AUTOMATED SEISMIC SURVEY DESIGN AND DISPERSED SOURCE ARRAY ACQUISITION

AUTOMATED SEISMIC SURVEY DESIGN AND DISPERSED SOURCE ARRAY ACQUISITION

Proefschrift

ter verkrijging van de graad van doctor
aan de Technische Universiteit Delft,
op gezag van de Rector Magnificus prof. ir. T.H.J.J. van der Hagen,
voorzitter van het College voor Promoties,
in het openbaar te verdedigen op woensdag 11 Maart 2020 om 12:30 uur

door

Matteo CAPORAL

Master of Science in Geophysics,
Università degli Studi di Pisa, Italië,
geboren te Pordenone, Italië.

Dit proefschrift is goedgekeurd door de promotoren

dr. ir. G. Blacquière en prof. dr. ir. C.P.A. Wapenaar

Samenstelling promotiecommissie:

Rector Magnificus,	voorzitter
Dr. ir. G. Blacquière,	promotor, Technische Universiteit Delft
Prof. dr. ir. C.P.A. Wapenaar,	promotor, Technische Universiteit Delft

Onafhankelijke leden:

Prof. dr. D.G. Simons,	Technische Universiteit Delft
Prof. dr. ir. E.C. Slob,	Technische Universiteit Delft
Prof. dr. M. Landrø,	Norwegian University of Science and Technology
Dr. I. Vasconcelos,	Universiteit Utrecht
Dr. ir. R. van Borselen,	Aramco Overseas Company

The research for this thesis was financially supported by the Delphi consortium.

Printed by: Ridderprint

Front & Back: Florian van Zandwijk

ISBN 978-94-6384-124-5

An electronic version of this dissertation is available at
http://repository.tudelft.nl/.

Ad Oriana, Nella,
Cinto & Isolina

CONTENTS

SUMMARY

Reflection seismology is nowadays the preferred technique in the oil and gas industry to estimate the properties of the Earth?s subsurface. The method typically includes a series of procedures that fit in three broad categories:

- seismic data acquisition;
- data processing and imaging;
- interpretation and reservoir characterization.

This thesis mainly focuses on the first category and aims at improving both the operational productivity of seismic surveys in terms of costs, and the quality of the data in terms of signal-to-noise ratio and frequency content. Hereafter, we present a novel approach to seismic data collection named Dispersed Source Array (DSA) acquisition. It is proposed to replace traditional broadband sources with a set of devices dedicated to different and complementary frequency bands. Modern multiple driver loudspeaker systems are based on the same key concept and their improved performance is demonstrated.
During field operations, it is often impossible to accurately implement nominal survey geometries in practice. Frequently, acquisition geophysicists are required to cope with unforeseen circumstances such as obstacles in the field and inaccessible or restricted areas. These complications may compromise the quality of the data or lead to delays, and thus extra expenses, during acquisition. In this thesis, we propose two automated approaches to survey design focused on avoiding spatial discontinuities in the recorded data and on guaranteeing adequate data quality. The two methods are based on the reorganization of regular (centralized) and irregular (decentralized) source acquisition grids, respectively, and provide a practical acquisition plan for seismic crews.
In this thesis, based on theoretical considerations and numerical data inversion and imaging examples, the feasibility of Dispersed Source Array acquisitions is demonstrated. Additionally, we show that it is possible to reliably recover subsurface information based on irregularly sampled datasets. We show how, despite the significant mismatch between baseline and monitor survey geometries, decentralized DSA surveys are also suitable for time-lapse studies.

SAMENVATTING

Reflectie-seismiek is de techniek die olie- en gasbedrijven veelal gebruiken om de eigenschappen van de ondergrond te schatten. De techniek bestaat grofweg uit de volgende onderdelen:

- seismische data-acquisitie;
- dataverwerking en beeldvorming;
- data-interpretatie en reservoir-karakterisering.

Dit proefschrift richt zich op de data-acquisitie en beoogt zowel de kosten ervan te verlagen door de productiviteit van seismische meetsessies te verhogen, als de datakwaliteit te verhogen in termen van signaal-ruisverhouding en frequentie-inhoud. We presenteren een nieuwe aanpak voor data- acquisitie met de naam DSA (eng: Dispersed Source Array). In deze aanpak worden de conventionele, breedbandige bronnen vervangen door een veelheid van brontypen, elk met hun eigen (beperkte) bandbreedte, die tezamen de volledige frequentieband afdekken. Moderne meerkanaals luidsprekersystemen zijn op ditzelfde concept gebaseerd en hun verbeterde prestaties zijn aangetoond.
Het is bij de uitvoering van de data-acquisitie vaak niet mogelijk om de van tevoren geplande acquisitie-geometrie exact te realiseren. Het komt geregeld voor dat geofysici moeten inspelen op onvoorziene omstandigheden zoals obstakels, ontoegankelijk terrein of verboden gebied. Dit soort problemen kunnen de kwaliteit van de meetgegevens negatief beïnvloeden, of leiden tot vertraging, wat kostenverhogend werkt. In dit proefschrift stellen we twee oplossingen voor het uitvoeren van een seismische survey voor die beide volledig automatisch werken. Beide trachten spatiële discontinuïteiten te vermijden en richten zich op het garanderen van een acceptabele datakwaliteit. De twee oplossingen zijn achtereenvolgens gebaseerd op een regelmatig (gecentraliseerd) en onregelmatig (gedecentraliseerd) bronraster, en voorzien in een praktisch acquisitieplan voor een seismische ploeg.
In dit proefschrift tonen we de haalbaarheid van het DSA-concept aan, op basis van theoretische overwegingen, resultaten van numerieke inversie en de hiermee verkregen afbeeldingen. Daarbij laten we zien dat het mogelijk is om op een betrouwbare manier informatie van de ondergrond te verkrijgen, uitgaande van spatieel onregelmatig bemonsterde meetgegevens. Tenslotte tonen we aan dat, ondanks een aanzienlijk verschil tussen de oorspronkelijke geometrie en de monitor geometrie, gedecentraliseerde DSA surveys ook geschikt zijn voor 4D studies.

1

INTRODUCTION

1

1.1. REFLECTION SEISMOLOGY

Reflection seismology is largely adopted for the exploration of the subsurface. This technique is utilized by geophysicists to reconstruct the stratigraphic and structural composition of the buried geological bodies of interest. Information about depositional geometries, stratification, faults, overthrusts and so on, can be retrieved without the need for invasive and expensive procedures such as drilling.
Clearly, this technology is of great interest to the oil and gas industry and it has been widely applied in hydrocarbon exploration, particularly since the 1950s. Additional fields of application include, among others, near-surface studies (for civil and environmental engineering), archeology, crustal studies and mineral exploration.
The general principle behind reflection seismology is relatively straightforward (Figure 1.1). Specially designed active sources generate seismic waves that propagate through the Earth's subsurface. The characteristics of their propagation are dictated by the strength and the frequency content of the emitted signal, in addition to the Earth's elastic properties. Specifically, the frequency band of seismic interest for hydrocarbon exploration goes roughly from 0 Hz to 100 Hz. Within the subsurface, a portion of the wavefront is reflected back upwards due to the variations in the acoustic impedance of the different geological structures. The reflected waves reaching the surface are recorded by the receivers, and the data are processed in order to produce a visual representation of the subsurface.
From a practical standpoint, the underlying physical foundations of this imaging method are not dissimilar to those of medical ultrasound. Also in that case, acoustic waves are sent into the medium to be inspected (human tissues) with the aid of an acoustic source (ultrasound transducer) in order to create an image of the internal body structures. However, the frequency band of interest for medical ultrasound is quite different from the frequency band of seismic interest and is generally in the range of 1 MHz to 18 MHz.

1.2. SEISMIC SOURCES

A fundamental component of every seismic survey is, of course, the energy source. The list of available seismic sources is extensive and specific care needs to be addressed to their selection. In fact, their influence on the recorded signal is substantial and may determine the success or failure of the whole survey. The main focus of the following paragraphs will be on the seismic sources that are, at present, routinely utilized by the oil and gas industry for hydrocarbon exploration. Hereafter, the sources are grouped in three broad categories based on the type of environment where they are predominantly deployed and their operating principles. These categories are *explosives*, *seismic vibrators* and *airguns*, respectively. Regarding the first category, a brief introduction about the deployment and characteristics of land and marine charges is provided. The main reasons for their decrease in popularity (particularly in marine environment) are specified. Subsequently the operating principles and advantages of the seismic vibrators will be treated. For the marine case, the operating principles of the airgun will instead be described. Note that, in transitional environments, a combination of land and marine sources may be preferred.

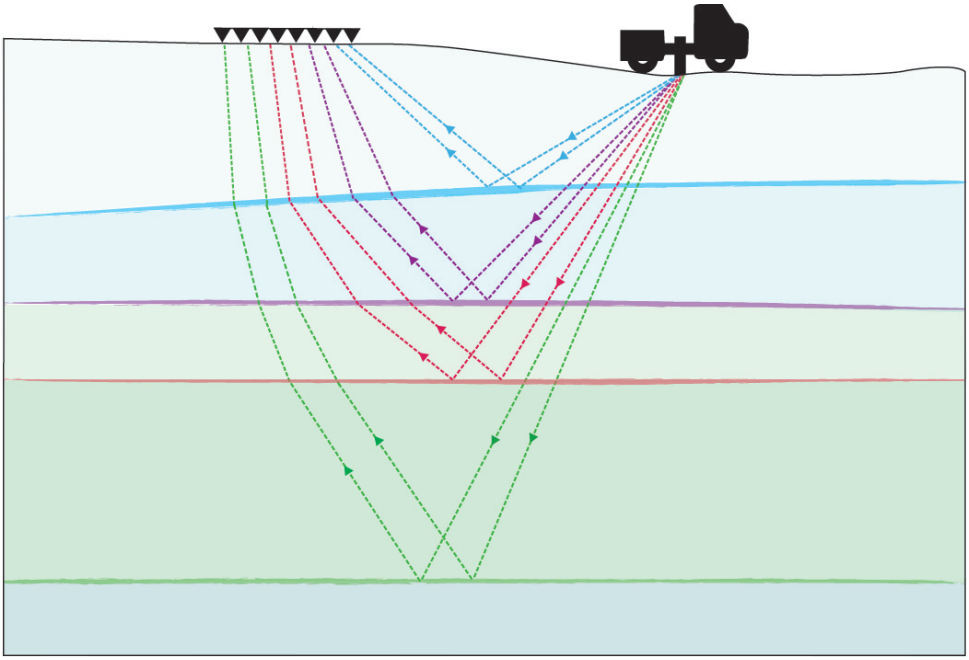

Figure 1.1: *Schematic representation of the general principle behind reflection seismology.*

1.2.1. EXPLOSIVES

Explosives and, in particular, dynamite (Figure 1.2) prevailed as the dominant seismic source in seismic exploration for a considerably long period of time before the debut of the first alternatives such as seismic vibrators in land operations and airguns in marine. From an economic perspective, dynamite surveys are relatively cheap with respect to surveys deploying different types of seismic sources. The expenses incurred in performing this kind of surveys are, for the large part, dictated by the costs of drilling the shot holes to place and detonate the explosives. Although comparatively very little energy is actually radiated in the frequency band of seismic interest, explosives have a remarkably high ratio of radiated (seismic) energy over mass [1]. Additional reasons for their popularity are, for instance, the ease of transport in difficult terrains and the lack of required regular maintenance, compared to other sources. Furthermore, upon detonation, explosives release large volumes of expanding gases that result in sudden high pressures traveling through the subsurface. As a consequence, their source signature resembles a band-limited, minimum-phase delta pulse, which is a highly desirable type of signal for geophysical prospecting [2, 3].

Despite the above-mentioned beneficial characteristics of explosive seismic sources, other acquisition techniques are now preferred, mainly due to environmental concerns. Explosive-based surveys are, in fact, rather invasive. Other than the immediate adverse effects that blasting activities may have on the surrounding flora, fauna and inhabited regions, explosions induce permanent deformation to the neighboring areas making these sur-

1

Figure 1.2: *Dynamite explosion during a seismic survey. Note that the picture was taken in the 1950s, currently the safety standards are much higher and dynamite explosions are hardly visible from the surface.*

veys inadequate for urban and ecologically delicate environments. Currently, dynamite surveys are almost entirely banned offshore, but are still common practice in land operations, when alternative sources would lead to unreasonably high costs or when the terrain is particularly inaccessible. However, in order to reduce their environmental impact, smaller charges are preferred also on land, leading to a potential lack of low frequency in the recorded signal [2]. Additionally, the frequency content of the recorded signal is highly dependent on the rock formation in which the charge is fired, making the source signature somewhat less predictable and repeatable [2]. Moreover, since the explosives must be placed at some depth below the surface, the recorded signal may be compromised by notches in the frequency band due to the *source ghost phenomenon*. The phenomenon is intrinsic of marine acquisitions but, although in a lesser degree, also affects land surveys with buried sources. For a more exhaustive explanation of the ghost problem (offshore), the reader is referred to [4].

1.2.2. SEISMIC VIBRATORS

Starting from the mid-1950s, seismic vibrators (Vibroseis™, Figure 1.3) were introduced and made commercially available in 1961 by Conoco Incorporated. This technology rapidly gained popularity in the industry and is today the preferred seismic source for land acquisition. The use of seismic vibrators is however still not as common in marine environment, despite the interest in the development of such technology is rapidly growing in recent years [5, 6].

From an operational perspective, seismic vibrators radiate seismic waves in the subsurface by exerting an oscillatory force on a baseplate, which is coupled to the ground as tightly as possible thanks to a so-called hold-down mass. The latter is vibrationally isolated from the system and is, in most cases, the weight of the vibrator truck itself. The driving force exercised on the baseplate is commonly supplied by a hydraulic system but may, less frequently, be provided by a purely mechanical, electromagnetic, piezoelectric or magnetostrictive actuator [7]. For hydraulic vibrators (Figure 1.4), the driving force is delivered by pumping fluid alternately into the lower and upper chambers of a piston, which is firmly anchored to the baseplate. The fluid flow between the two chambers, in turn, pushes against a reaction mass that is free to slide along the shaft connecting the piston with the baseplate. The resulting force on the baseplate (and consequently on the ground) is, in principle, equal and opposite to the force on the reaction mass. A servovalve is utilized to regulate the flow rate and, thus, the emitted signal. A more detailed theoretical and practical description of the operating principles of seismic vibrators is beyond the scope of this thesis, the interested reader is referred to [8–11].

Figure 1.3: *Vibroseis source truck. Picture taken by Dr. Rik Noorlandt.*

1

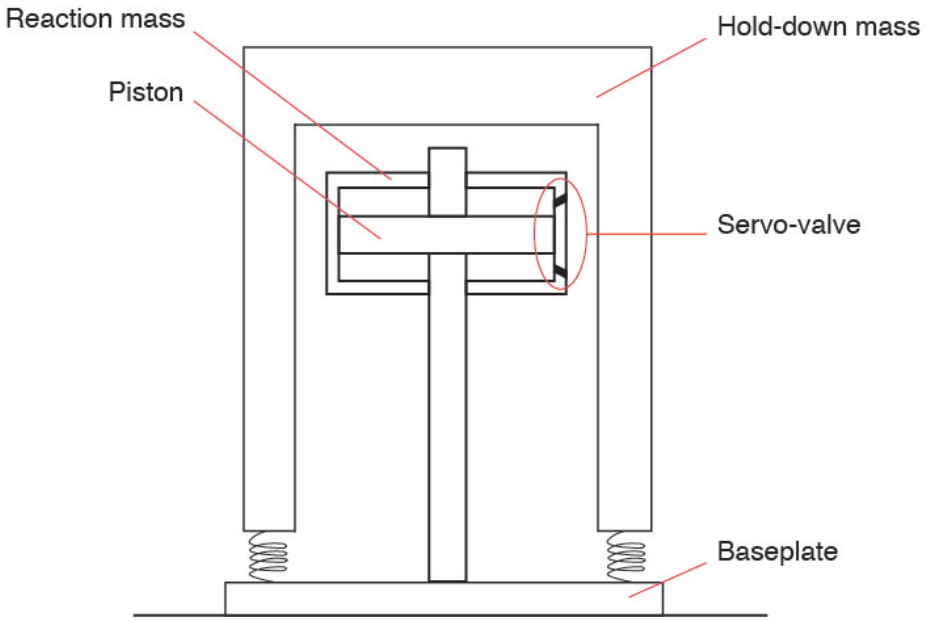

Figure 1.4: *Hydraulic vibrator mechanical model.*

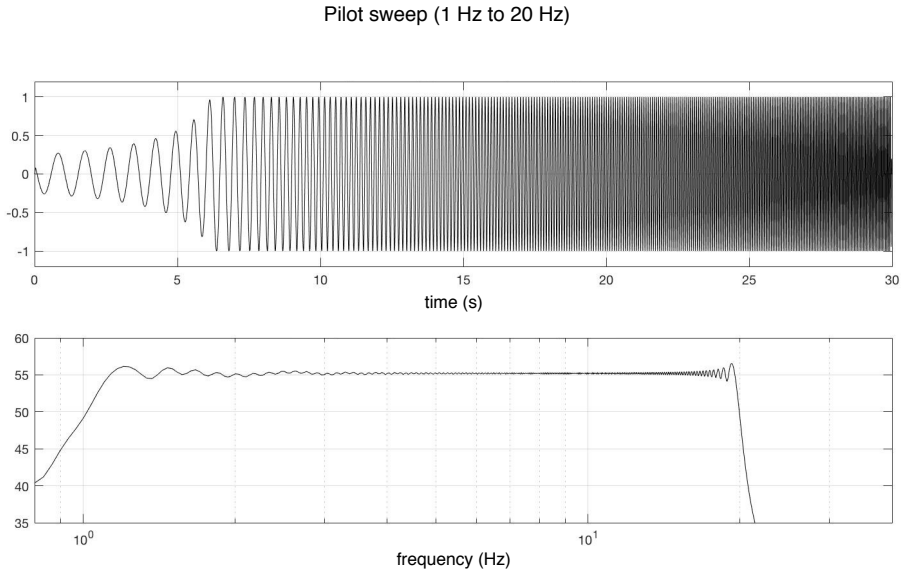

Figure 1.5: *Uncorrelated vibroseis pilot sweep (1 Hz to 20 Hz) in the time and temporal frequency domain.*

A very important characteristic of the vibroseis is that, despite being a relatively low power source, it is not a low energy system. This means that the same energy impulsively released in the frequency band of seismic interest by explosive sources can be radiated by seismic vibrators with a non-impulsive, and thus less invasive, user-defined signal of the duration of several seconds. This signal is essentially a sinusoid with continuously varying frequency and it is commonly referred to as *sweep* (Figure 1.5). However, as the ultimate goal of seismic surveys is obtaining the impulsive response of the earth, the effect of the increased source signature duration on the recorded data has to be eliminated. This can be achieved by cross-correlating the seismic record with the source sweep. Hence, the high degree of control on the phase and amplitude spectra of the outgoing signal guaranteed by the vibroseis method is essential. Furthermore, it allows to limit the generation of energy at frequency ranges that are of no benefit for seismic imaging (e.g. above $\sim 100\ Hz$) but may still have detrimental effects on the surrounding areas. With respect to dynamite surveys, the improved control on the seismic source wavelet also sensibly increases the land seismic experiment repeatability.

Being a surface source, the vibroseis has the additional advantage of not being affected by the source ghost phenomenon. Nevertheless, for the same reason, a much larger amount of surface waves than with buried explosives charges is generated. Although part of this energy may be used for imaging too, it is conventionally considered undesirable noise. Note that, according to [12], as little as the 6.8% of the energy radiated by seismic vibrators consists of P-waves. The remaining energy is distributed between SV-waves (25.8%) and Rayleigh waves (67.4%). Additionally, in vibroseis operations, poor coupling between earth and baseplate, as well as nonlinearities associated with the mechanical and hydraulic properties of the vibrator, can result in harmonic distortions [13]. The harmonic signal is generally treated as noise but, unlike other types of noise, is not uncorrelated with the fundamental sweep. As a consequence, the crosscorrelation process may produce undesired artifacts, namely an oscillatory tail on the correlogram for *downsweeps* (sweeps with frequency decreasing with time) or an oscillatory forerunner on the correlogram for *upsweeps* (sweeps with frequency increasing with time).

In spite of being the preferred seismic source for land applications, hydraulic vibrators produce a relatively limited amount of low frequency energy and the signal-to-noise ratio can still be quite poor for frequencies below ~ 5 Hz [12]. De facto, increasing the low frequency content of land vibrator signals is an issue that has been abundantly addressed during the last few decades [e.g. 14–17]. The key constraining factors at the lower end of the spectrum are the reaction mass stroke (reaction mass displacement limit), the high flow demand (pump and servo-valve ability to cope with strong flow oscillations) and the size of the baseplate. As we move to the higher frequencies, what become important limiting components are the mass and stiffness of the baseplate, the compressibility of the hydraulic fluid and the mechanical limitation of the driven structure [12]. The machine's limitations, however, seem to have a larger detrimental effect on the lower frequencies than on the higher frequencies of seismic interest, despite promising new advances in source design.

1

1.2.3. AIRGUNS

Starting from the early 1960s, dynamite surveys were almost entirely banned offshore due to their highly destructive effects on marine ecosystems. It is in this context that airguns, now the most popular marine seismic source, made their first appearance in offshore seismic surveys. In fact, such sources can be considered a reliable, repeatable and relatively safe seismic source in comparison to explosive alternatives, despite increasing environmental concerns do exist and are currently being addressed also by the oil industry.

As suggested by their name, airguns are rather simple mechanical devices that rely on the use of compressed air in order to generate acoustic waves. The air is first pumped under relatively high pressure into the firing chamber of the device, and then suddenly released into the surrounding water as an air bubble. Since the air pressure within the bubble is initially much greater than the hydrostatic pressure of the water, the bubble starts to rapidly expand. Eventually, the air reaches a pressure equal to that of the surrounding fluid, but inertia causes the bubble to continue to expand well beyond this threshold (to overshoot). Once the expansion has ceased, the air pressure is thus below the hydrostatic pressure and the bubble starts to collapse. In turn, the collapse overshoots the equilibrium position and the cycle starts again. These oscillations continue for several cycles, before being completely damped by frictional forces and heat dissipation in the water. This characteristic behaviour results in a source signature with a shape resembling a damped sine curve (Figure 1.6), quite far from a band-limited delta pulse,

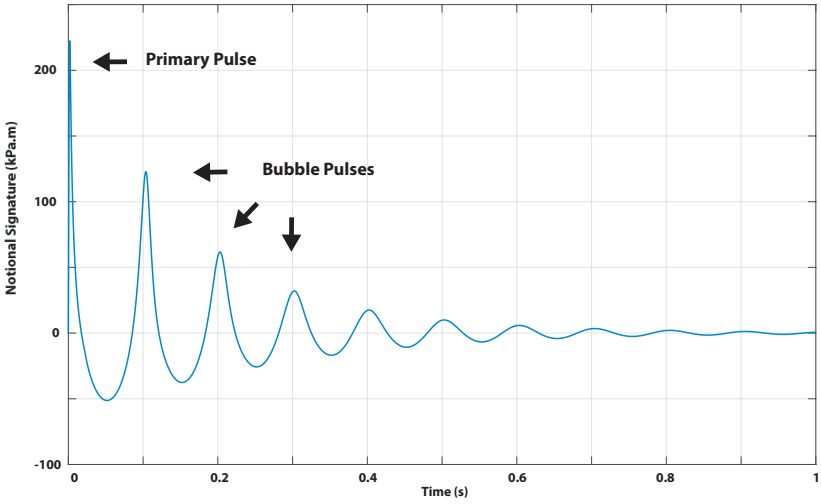

Figure 1.6: *Airgun signature in the time domain. The first pressure peak corresponds to the primary pulse generated when the airgun ports first open. The following pressure peaks are produced by the expansion-collapse cycle of the air bubble. The peaks gradually decrease in amplitude due to frictional forces and dissipation in the water. The signal is modeled with the airgun signature modeling software developed by [18].*

which is the most desirable type of signal for geophysical prospecting. On these grounds, airguns are generally utilized in arrays of multiple guns fired simultaneously, each with a different firing chamber volume. In fact, the period of oscillation of the bubble generated by an airgun (or the wavelength of the sinusoid, if we think of the airgun signature as a damped sine curve) depends on the volume of air released. Thus, the first peaks of the pressure pulses of each gun add up constructively, increasing the overall amplitude, while the subsequent pulses are out of phase and, therefore, their sum attenuates the relative influence on the signal. As a consequence, the resulting source signature is much closer to the ideal impulsive seismic wavelet than the signatures from individual guns. However, by utilizing arrays instead of single sources, we inevitably introduce directionality effects most commonly known as *directivity*. This means that the total shape of the signal is not constant in all directions, but depends on the direction in which the wave is traveling. The size of a typical airgun array is, in fact, around 20 m, which is comparable to the shortest wavelengths of seismic interest. Additionally, it can be observed that the interference between the signals of different guns of the same array is highly nonlinear in the near field. Despite this effect is highly mitigated in the far field, it may sensibly affect the signature of the airgun array. It is thus crucial to take these effects into account, when measuring the source signature. Furthermore, since airguns are placed at some depth below the water surface, the recorded signal is compromised by notches in the frequency band due to the *source ghost phenomenon*. For a more detailed description of the airgun source operating principles and of their signature determination, the interested reader is referred to [4, 19, 20].

1.3. IMPORTANCE OF A BROAD FREQUENCY BAND

In exploration seismology, the contribution of broadband data acquisition and processing to high-quality imaging, inversion and, ultimately, interpretation is critical [21].
A broad temporal frequency spectrum plays an important role in enhancing the resolution of seismic images and mitigating the interference between neighboring seismic events [22, 23]. On one hand, high frequencies reduce the width the main lobe of the seismic wavelet, resulting in a sharper, and thus more desirable, source signature. On the other hand, low frequencies decrease the amplitude of the side lobes of the wavelet, improving the interpreters' ability to differentiate between distinct reflections. These principles are illustrated in Figure 1.7. A total of three different bandpass filters are applied to the same band limited impulse response. More low frequencies (Figure 1.7a) translate in a better peak-to-sidelobe ratio, while more high frequencies (Figure 1.7c) result in a main lobe closer in shape to a band limited delta pulse.
Also, note that the behavior of seismic waves at low and high frequencies can display substantially different characteristics. For instance, high frequencies are essential for high-resolution near-surface studies. Low frequencies instead guarantee better signal penetration suffering less from scattering and absorption phenomena. In particular, the influence of small scale inhomogeneities on the low frequencies is limited. For long wavelengths, small scatterers are, in fact, negligible and the wavefield will propagate through the medium nearly unaffected.
Broadband data may also favor the solution of inverse problems. In geophysics, since

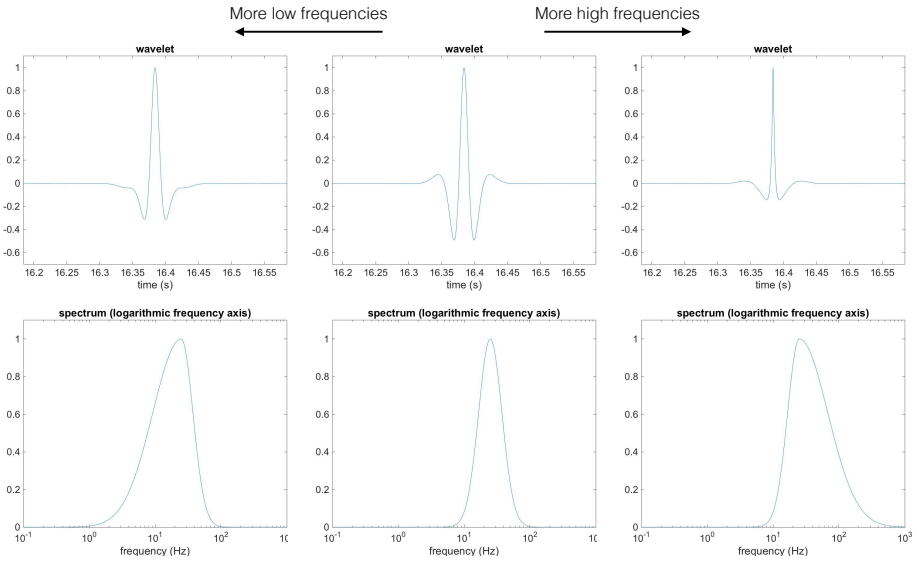

Figure 1.7: *Importance of a broad frequency band: more low frequencies (left column) translate in a better peak-to-sidelobe ratio; more high frequencies (right column) result in a main lobe closer in shape to a band limited delta pulse. The wavelets presented in the figure are generated in the frequency domain around a peak at 25 Hz, with varying low/high frequency slopes.*

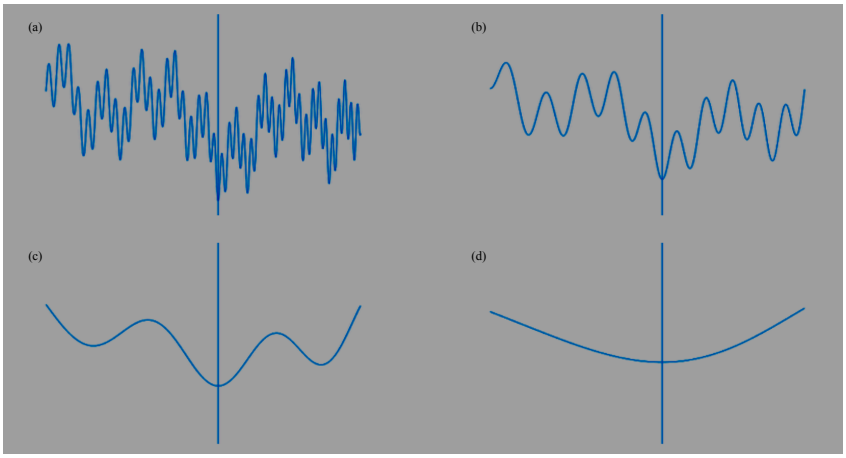

Figure 1.8: *Simple schematic representation of the advantages of multigrid (or multiscale) inversion approach. By decomposing the problem by scale, the performance of iterative inversions can be improved. At low frequencies (d), the inversion can get closer to the neighborhood of the global minimum. We can then gradually include higher frequencies, in order to improve the resolution, by moving on to the inversion of (c), (b) and, ultimately, (a).*

full waveform inversion (FWI) was first introduced by [24], seismic inversion techniques remarkably gained popularity. These iterative methods consist of nonlinear inversion algorithms aimed at determining earth parameters through the minimization of the misfit between the observed and the modeled data. In particular, they are most commonly used as velocity or impedance model building tools.
Considering that global optimization methods are not computationally affordable to address this kind of problems, one of the main challenges of FWI and similar techniques is the presence of local minima in the (least-squares) misfit functional. As a consequence, the inversion scheme is particularly sensitive to the initial model and prone to fail in predicting the correct earth parameters, if the starting model is too far from the global minimum.
In this context, low frequencies are crucial to attain a more reliable degree of convergence to the neighborhood of the global minimum. In fact, although there is still no theoretical guarantee of convergence, at low frequencies the presence of local minima can be largely mitigated. Consequently, inversion algorithms are often implemented with a frequency-based multigrid (or multiscale) approach, in order to facilitate a faster and more accurate convergence [25]. The approach consists in decomposing the problem by scale: after defining an arbitrary number of scales ranging from low to high frequencies, it is convenient to invert each scale sequentially, with the initial model of scale *i* being the final model of scale *i-1*. In Figure 1.8, a schematic representation of the concept is presented. A multimodal objective function and its respective decompositions onto four different scales are shown. By slowly increasing the maximum inversion frequency, it is possible to sensibly improve the chances of successful convergence. Although the method might not always work as smoothly as suggested in the example, it is fair to imply that the width of the valley around the global minimum of the misfit functional is generally proportional to the length of the scale. For the same reason, of great value for inversion are also the large offsets [26]. As suggested above, only the lower seismic frequencies can preserve sufficient energy at this range of distance from the source point.

1.4. DISPERSED SOURCE ARRAYS ACQUISITION

Currently, in order to acquire broadband seismic data, the industry relies on the use of especially designed broadband sources. However, from a practical point of view, a significant effort is required to profitably produce and operate such sources and often it is unavoidable to accept a trade-off between transmission efficiency, costs and operational flexibility. In particular, the most commonly utilized seismic sources, both on land (vibroseis) and in marine environment (airguns), produce relatively limited low-frequency energy. Conversely, conventional impulsive sources, such as dynamite on land and airguns offshore, produce extensive energy at frequency ranges that are of no use to seismic imaging, namely at the high side of the spectrum. Following the guidelines drawn by [27], we propose to make use of multiple types of sources during seismic surveys. The entire ensemble of sources represents as a whole a so-called dispersed source array (DSA, Figure 1.9). Each source type involved in a DSA acquisition is dedicated to a particular frequency band without the need to satisfy the seismic wideband requirement, thus avoiding the above-mentioned trade-off. Together, the devices are meant to cover the

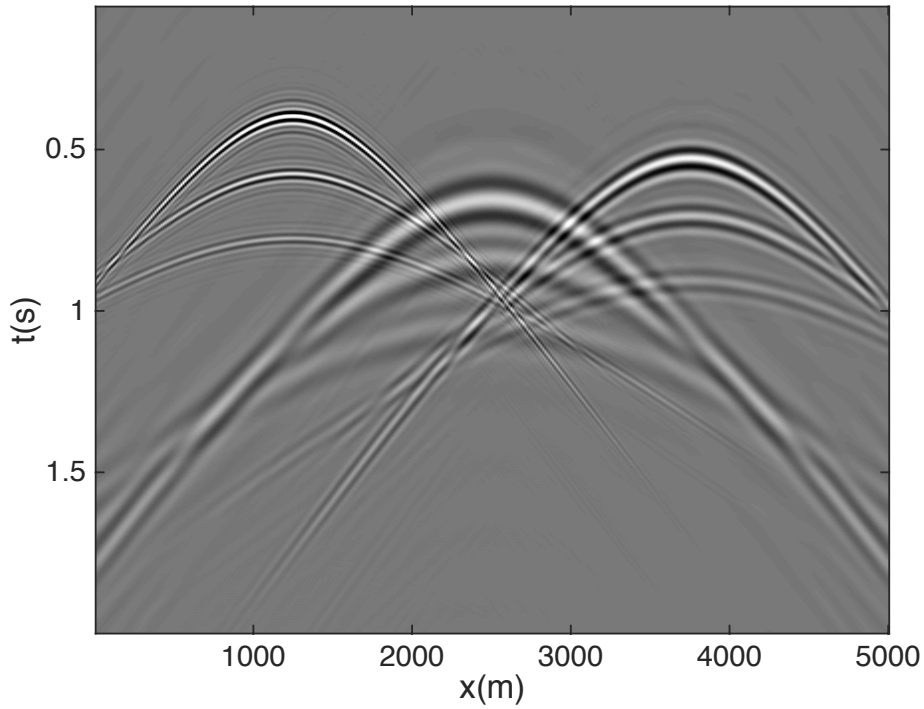

Figure 1.9: *Example of a DSA blended seismic record generated numerically. The simulation shows the reflection response of different DSA sources fired in rapid succession on a flat layered medium. The source wavelets utilized for this example are Ricker wavelets with different central frequencies (4 Hz, 10 Hz and 20 Hz, respectively).*

entire temporal and spatial bandwidth of interest. The concept is rapidly gaining momentum and dispersed source array prototypes specifically dedicated to the emission of the low frequencies have already been developed both for land [28] and for marine [29]. Successful field tests have been carried out in recent year as well [30]. Hereafter, we examine the impact of the use of low frequency land vibrators [28] in a seismic survey together with conventional broadband sources, through a realistic theoretical case study.

1.4.1. CASE STUDY. ULTRALOW FREQUENCY VIBRATOR: SWEEP DESIGN AND SURVEY PRODUCTIVITY

Thanks to recent progress in acquisition technology, many modern seismic vibrators can successfully emit frequencies as low as 1 Hz. Yet, for most field applications, they fail to generate enough energy to effectively cope with the significant ambient noise levels at the lower end of the spectrum. In practice, this limitation can be addressed utilizing heavier reaction masses, bigger pumps and/or extra hydraulic accumulators to compensate for the higher flow demand. Withal, such improvements remain a great challenge

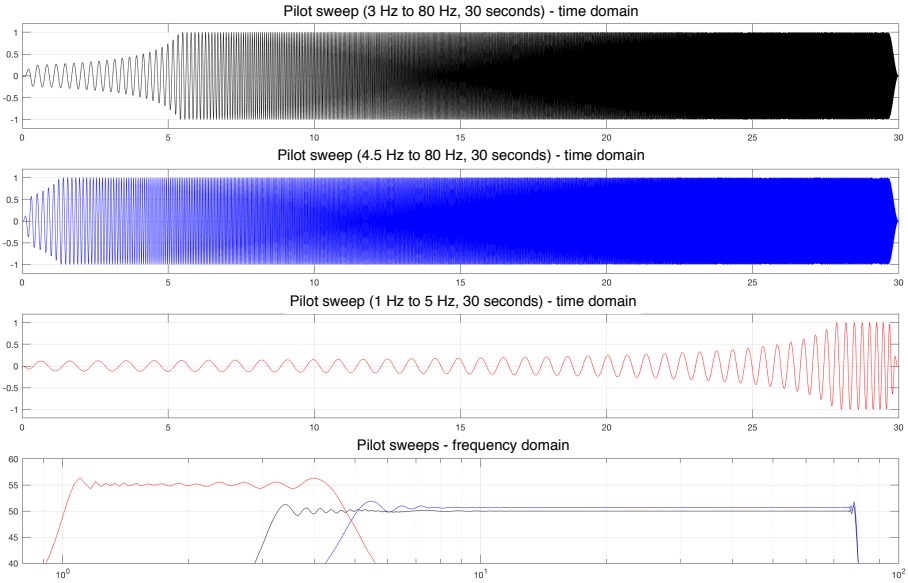

Figure 1.10: *Comparison of broadband and DSA vibroseis pilot sweep. All sweeps have the same duration.*

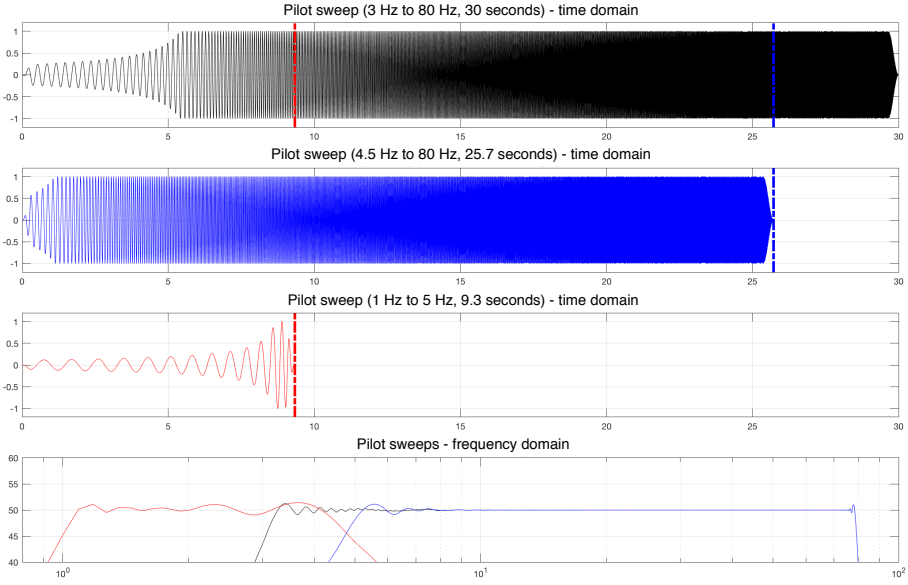

Figure 1.11: *Comparison of broadband and DSA vibroseis pilot sweep. All sweeps have the same amplitude.*

for developers and engineers and can considerably compromise the operational flexibility of the vibrator trucks. Customized non linear sweeps allow to maintain a flat spectrum on the full bandwidth of interest [11, 14], requiring however longer sweep times and overall significantly increasing the survey cost. Essentially, the time spent on the ultralow frequencies (≈ 1-5 Hz) represents the largest portion of the sweep duration with non trivial consequences on the productivity of the acquisition system. In the following paragraphs, we propose a quantitative sweep analysis inspired by the work of [31] on the impact of the use of broadband vibrators on crew productivity. In particular, we investigate the significance of the joint employment of conventional vibrators and seismic vibrators specifically dedicated to the lower frequencies of seismic interest.
As shown in Figure 1.10a, we first examine a 3-80 Hz, 30 s customized non-linear sweep generated with a conventional 61800 lbf vibrator (ION Geophysical AHV-IV, Model 362). Secondly, we look at two customized, non-linear, 30 s sweeps to be jointly employed in a (two source types) DSA survey (Figure 1.10b-c): on one hand a 4.5-80 Hz pilot sweep generated with the same above-mentioned vibrator, on the other hand a 1-5 Hz sweep generated with a 60000 lbf *very low frequency seismic vibrator* [28]. Considering that this is a comparative study and that the peak ground force of the two vibrators is very similar, its values were not taken into account during the simulations (we set $F_{peak} = 1$ lbf in both cases). Clearly, the total amount of energy emitted by the vibrators to be jointly employed in a DSA survey is appreciably higher, especially looking at the lower frequencies (Figure 1.10d). If instead we aim at a comparable energy spectrum, we can save up to 15 % of the total sweep duration (4.3 s of 30 s) for the higher part of the bandwidth and up to 70 % of the total sweep duration (20.7 s of 30 s) for the lower part of the bandwidth (Figure 1.11).
In addition, the simultaneous use of different sources with diversified spectral properties could appreciably help improving the signal-to-noise ratio of the data. In fact, ambient noise records from around the world clearly show that the noise levels can significantly vary not only from one survey area to another, but even between different frequency bands and over time [32]. In many circumstances emitting energy with a flat amplitude spectrum over the entire frequency band of interest might not be the most suitable choice. This is even more true if we consider that the response of the receivers (as well as the earth response) is hardly flat in the frequency domain. Consequently, the improved flexibility in the emission of seismic energy per frequency range introduced by the DSA concept represents a worthwhile added value. Obviously, these considerations also apply to marine surveys and their validity is not limited to low frequency sources.

1.5. BLENDING

Recent improvements in acquisition technology and research allow and encourage geophysicists and engineers to think outside the box. Every year, more flexible, other than more efficient, survey designs and field equipments are developed and tested. In fact, data acquisition has a major economic impact on the seismic industry, representing per se the largest part of the investments occurring ahead of drilling. Subsequently, in data acquisition more than in other aspects of the seismic method, there is a great need to gain in efficiency. In other words, it is reasonable to aim for alternative survey tech-

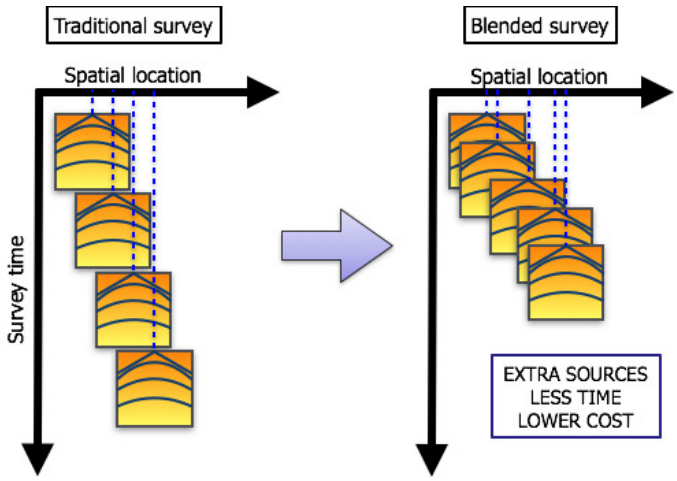

Figure 1.12: *Graphic representation of the concept of blending (simultaneous source acquisition).*

niques, which may require a new look at the acquired datasets, but reduce acquisition costs and time. That is to say, for a fixed, or even lower, seismic survey cost, higher quality data can be recorded with unconventional techniques. The quality of the data being measured in terms of signal-to-noise ratio, signal bandwidth and maximum angle of illumination and sensing.

On this basis, much attention has been paid to the so-called *blended* or *simultaneous* seismic acquisition technique. In traditional seismic surveys, the interference between different sources within a single record is avoided by choosing either the temporal interval or the lateral distance among consecutive shots sufficiently large. In order to keep the seismic survey economically feasible, these precautions often lead to a severe undersampling in the source domain or to a limited aperture. However, in blended acquisitions, the condition of non-overlapping shots is abandoned, allowing denser source sampling, or wider aperture, but leaving the rest of the acquisition parameters nearly unaltered. The simultaneous source data can either be separated with the aid of especially designed numerical techniques [*deblending*; e.g. 33, 34], or directly used for imaging and inversion [e.g. 35, 36].

The benefits of using simultaneous or blended sources during seismic surveys have been demonstrated and largely accepted [see, for example, 37–40]. Each subsurface grid point can concurrently be illuminated from a larger number of angles and, more importantly, from larger angles. This results in subsurface images with higher spatial resolution, leading to better reservoir characterization. Survey time and costs are reduced as well and the total signal-to-noise ratio is also improved [41]. A schematic comparison between conventional and blended acquisition systems is shown in Figure 1.12. Note that, in the context of DSA survey design, the concept of blending is exceptionally appealing. Considering that, in principle, more sources than for traditional surveys would be deployed in the field at the same time, simultaneous shooting would be an essential tool to reduce the acquisition costs.

1

1.6. OBSTACLES AND SYSTEM DECENTRALIZATION

From a practical standpoint, unforeseen logistical complications may arise once theoretical survey designs need to be implemented in the field. It is not uncommon to encounter surface obstacles, restricted areas or inaccessible terrains during operations. Some of this information may be available in advance, but it is often necessary to promptly modify the acquisition preplans. With this work, we suggest to look at seismic acquisition as a challenging coordination problem and propose two different automated approaches in order to solve it while, at the same time, minimizing the direct intervention of survey designers.
With the first approach, the so-called *centralized* method, we tackle the automated reorganization of a predefined source geometry around the obstacles in the field. With the second, the so-called *decentralized* method, we propose a fundamental change in the system architecture of seismic surveys. This approach is particularly suitable for simultaneous multi-source surveys (e.g. DSA acquisitions). The individually simple components of the acquisition system (source vessels in marine and source vehicles on land) are expected to make autonomous decisions to achieve a global task as a whole (acquiring a well-sampled dataset). In particular, every unit must be able to modify in real-time its own behavior (the moving speed and direction) in order to promptly adapt to environmental changes, such as the presence of an unexpected obstacle on its path. In the latter case, a detailed survey preplan is not required.

1.7. THESIS OUTLINE

Chapter 2 discusses in detail the benefits of Dispersed Source Array acquisitions under a technical, operational and theoretical perspective. Issues such as source sampling, ghost interference and environmental concerns surrounding seismic surveys are reviewed. The so-called Full Wavefield Migration algorithm is introduced and utilized in a numerical example for the inversion of a 3D Dispersed Source Array dataset in order to retrieve the correspondent reflectivity model. The chapter has been published as a journal paper in *Geophysical Prospecting* [42]. Note that minor changes have been introduced to make the text consistent with the rest of the chapters of this thesis.
Chapter 3 focuses on automated survey design in the presence of adverse field conditions, such as restricted areas or obstacles on the terrain. Two different methods to tackle the problem are presented. The two methods are based on the reorganization of regular (centralized) and irregular (decentralized) source acquisition grids, respectively. We tested the algorithms on a real terrain map featured by a substantial amount of inaccessible areas due to the presence of steep sand dunes. The chapter has been submitted to the journal *Geophysics*.
Chapter 4 combines the concepts of Dispersed Source Array acquisition and decentralization in a single study. The theory of Full Wavefield Migration is further extended to contemporaneously invert for reflectivity and velocity subsurface models (Joint Migration Inversion). This extension is relatively straightforward under the assumption that the velocity model only affects the kinematics of the modeled data without generating scattering, while the reflectivity model generates all orders of scattering without affecting

the kinematics of the data. The impact of Dispersed Source Array decentralized surveys on time lapse acquisition is also investigated. Numerical examples in support of this study are provided. The chapter has been submitted to the journal *Geophysical Journal International*.
Chapter 5 discusses the conclusions drawn from this research. A series of recommendations for future work on the topics of Dispersed Source Array acquisition and automated path planning for seismic survey design are proposed.

1

REFERENCES

[1] M. Lavergne, *Emission by underwater explosions,* Geophysics **35**, 419 (1970).

[2] J. A. Sharpe, *The production of elastic waves by explosion pressures; I, theory and empirical field observations,* Geophysics **7**, 144 (1942).

[3] W. E. Peet, *A shock wave theory for the generation of the seismic signal around a spherical shot hole,* Geophysical Prospecting **8**, 509 (1960).

[4] G. Parkes and L. Hatton, *The Marine Seismic Source* (Reidel, 1986).

[5] R. M. Laws, D. Halliday, J. F. Hopperstad, D. Gerez, M. Supawala, A. Özbek, T. Murray, and E. Kragh, *Marine vibrators: the new phase of seismic exploration,* Geophysical Prospecting **67**, 1443 (2019).

[6] A. Feltham, M. Girard, M. Jenkerson, V. Nechayuk, S. Griswold, N. Henderson, and G. Johnson, *The marine vibrators joint industry project: four years on,* Exploration Geophysics **49**, 675 (2017).

[7] J. Meunier, *Seismic Acquisition from yesterday to tomorrow* (Society of Exploration Geophysicists, 2011).

[8] W. E. Lerwill, *The amplitude and phase response of a seismic vibrator,* Geophysical Prospecting **29**, 503 (1981).

[9] J. J. Sallas and R. M. Weber, *Comments on "The amplitude and phase response of a seismic vibrator" by W. E. Lerwill,* Geophysical Prospecting **30**, 935 (1982).

[10] G. Baeten and A. M. Ziolkowski, *The vibroseis source* (Elsevier, 1984).

[11] N. A. Anstey, *Vibroseis* (Prentice Hall, 1991).

[12] J. J. Sallas, *How do hydraulic vibrators work? a look inside the black box,* Geophysical Prospecting **58**, 3 (2010).

[13] A. J. Seriff and W. H. Kim, *The effect of harmonic distortion in the use of vibratory surface sources,* Geophysics **35**, 234 (1970).

[14] C. Bagaini, *Low-frequency vibroseis data with maximum displacement sweeps,* The Leading Edge **27**, 582 (2008).

[15] G. J. M. Baeten, A. Egreteau, J. Gibson, F. Lin, P. Maxwell, and J. J. Sallas, *Low-frequency generation using seismic vibrators,* EAGE (Eur. Ass. of Geosc. and Eng., Expanded abstracts, 2010).

[16] Z. Wei and T. F. Phillips, *On the generation of low frequencies with modern seimic vibrators,* Geophysics **78**, WA91 (2013).

[17] N. Tellier and G. Ollivrin, *Low-frequency vibroseis: current achievements and the road ahead?* First Break **37**, 48 (2019).

[18] H. O. Sertlek, M. A. Ainslie, and R. M. Laws, *Agora Source Signatures for the International Airgun Modelling Workshop* (IEEE Dataport Online: http://dx.doi.org/10.21227/5081-yr65, 2019).

[19] A. M. Ziolkowski, G. E. Parkes, L. Hatton, and T. Haugland, *The signature of an air gun array: Computation from near-field measurements including interaction,* Geophysics **47**, 1413 (1982).

[20] W. H. Dragoset, *A comprehensive method for evaluating the design of air guns and air gun arrays,* The Leading Edge **3**, 52 (1984).

[21] F. ten Kroode, S. Bergler, C. Corsten, J. W. de Maag, F. Strijbos, and H. Tijhof, *Broadband seismic data - the importance of low frequencies,* Geophysics **78**, WA3 (2013).

[22] R. S. Kallweit and L. C. Wood, *The limits of resolution of zero-phase wavelets,* Geophysics **47**, 1035 (1982).

[23] A. J. Berkhout, *Seismic resolution* (Geophysical press, London, 1984).

[24] A. Tarantola, *A strategy for nonlinear elastic inversion of seismic reflection data,* Geophysics **51**, 1893 (1986).

[25] C. Bunks, F. M. Saleck, S. Zaleski, and G. Chavent, *Multiscale seismic waveform inversion,* Geophysics **60**, 1457 (1995).

[26] O. Gauthier, J. Virieux, and A. Tarantola, *Two-dimensional nonlinear inversion of seismic waveforms; numerical results,* Geophysics **51**, 1387 (1986).

[27] A. J. Berkhout, *Blended acquisition with dispersed source arrays,* Geophysics **77**, A19 (2012).

[28] D. K. Reust, O. A. Johnston, J. A. Giles, and S. Ballinger, *Very low frequency seismic source,* SEG (Soc. Expl. Geophys., Expanded abstracts, 2015).

[29] J. Dellinger, A. Ross, D. Meaux, A. Brenders, G. Gesoff, J. T. Etgen, J. Naranjo, G. Openshaw, and M. Harper, *Wolfspar, an fwi friendly ultra-low-frequency marine seismic source,* SEG (Soc. Expl. Geophys., Expanded abstracts, 2016).

[30] C. Tsingas, Y. S. Kim, and J. Yoo, *Broadband acquisition, deblending, and imaging employing dispersed source arrays,* The Leading Edge **35**, 354 (2016).

[31] N. Tellier and G. Ollivrin, *Impact of the use of low-frequency heavy vibrators on crew productivity,* SEG (Soc. Expl. Geophys., Expanded abstracts, 2014).

[32] W. P. Kimman and P. L. Vermeer, *Use of low and high noise models for land surface-seismic data,* EAGE (Eur. Ass. of Geosc. and Eng., Expanded abstracts, 2015).

[33] J. Stefani, G. Hampson, and E. F. Herkenhoff, *Acquisition using simultaneous sources,* EAGE (Eur. Ass. of Geosc. and Eng., Expanded abstracts, 2007).

[34] L. T. Ikelle, *Coding and decoding: seismic data modeling, acquisition and processing,* SEG (Soc. Expl. Geophys., Expanded abstracts, 2007).

[35] Y. Tang and B. Biondi, *Least-squares migration/inversion of blended data,* SEG (Soc. Expl. Geophys., Expanded abstracts, Houston, 2009) pp. 2859–2863.

[36] W. Dai, X. Wang, and G. T. Schuster, *Least-squares migration of multisource data with a deblurring filter,* Geophysics **76**, R135 (2011).

[37] S. T. Vaage, *Method and system for acquiring marine seismic data using multiple seismic sources,* U.S. Patent 6 906 981 (2002).

[38] C. J. Beasley, *A new look at marine simultaneous sources,* The Leading Edge **27**, 914 (2008).

[39] A. J. Berkhout, *Changing the mindset in seismic acquisition,* The Leading Edge **27**, 924 (2008).

[40] C. Bagaini, *Acquisition and processing of simultaneous vibroseis data,* Geophyshysical Prospecting **58**, 81 (2010).

[41] G. Berkhout and G. Blacquière, *Effect of noise in blending and deblending,* Geophysics **78**, A35 (2013).

[42] M. Caporal, G. Blacquière, and M. Davydenko, *Broadband imaging via direct inversion of blended dispersed source array data,* Geophysical Prospecting **66**, 942 (2018).

2

BROADBAND IMAGING VIA DIRECT INVERSION OF BLENDED DISPERSED SOURCE ARRAY DATA

Although seismic sources typically consist of identical broadband units alone, no physical constraint dictates the use of only one kind of device. We propose an acquisition method that involves the simultaneous exploitation of multiple types of sources during seismic surveys. It is suggested to replace (or support) traditional broadband sources with several devices individually transmitting diverse and reduced frequency bands and covering together the entire temporal and spatial bandwidth of interest. Together these devices represent a so-called Dispersed Source Array.

As a consequence, the use of simpler sources becomes a practical proposition for seismic acquisition. In fact, the devices dedicated to the generation of the higher frequencies may be smaller and less powerful than the conventional sources, providing the acquisition system with an increased operational flexibility and decreasing its environmental impact. Offshore we can think of more manageable boats carrying airguns of different volumes or marine vibrators generating sweeps with different frequency ranges. On land vibrator trucks of different sizes, specifically designed for the emission of particular frequency bands, are preferred. From a manufacturing point of view, such source units guarantee a more efficient acoustic energy transmission than today's complex broadband alternatives, relaxing the low versus high frequencies compromise. Furthermore, specific attention can be addressed to choose shot densities that are optimum for the different devices according to their emitted bandwidth. In fact, since the sampling requirements depend on the maximum transmitted frequencies, the appropriate number of sources dedicated to the lower frequencies is relatively small, provided the signal-to-noise ratio requirements are met. Additionally, the method allows to rethink the way to address the ghost problem in marine seismic acquisition, permitting to tow different sources at different depths based on the devices individual central frequencies. As a consequence, the destructive interference of the ghost notches, including the one at 0 Hz, is largely mitigated. Furthermore, blended acquisition (also known as simultaneous source acquisition) is part of the Dispersed Source Array concept, improving the operational flexibility, the cost efficiency and the signal to noise ratio.

Based on theoretical considerations and numerical data examples, the advantages of this approach and its feasibility are demonstrated.

This chapter has been published in Geophysical Prospecting [1]. Note that minor changes have been introduced to make the text consistent with the other chapters of this thesis. Coauthors: G. Blacquière and M. Davydenko.

2.1. INTRODUCTION

In exploration seismology, it is widely accepted that the contribution of both high and low frequencies is of fundamental importance for high-quality seismic imaging. High frequencies provide sharper wavelets resulting in an improved vertical resolution. Low frequencies can drastically reduce the wavelet sidelobes amplitude and therefore the potential interference among neighboring seismic events. They also translate in better signal penetration, suffering less from scattering and attenuation. Furthermore, they play a crucial role in seismic inversion for velocity and impedance models. An interesting and detailed overview on the importance of broadband data acquisition and processing, with specific focus on the low frequencies, is presented by [2].

In particular, the most commonly used seismic sources, both on land (vibroseis, dynamite) and offshore (airguns), produce relatively little low frequency energy. The conventional methodology to acquire satisfactory data in the whole bandwidth of interest consists of producing more energy at all frequencies utilizing broadband sources. From a practical point of view, a significant effort is required to profitably manufacture and operate such sources and it is often unavoidable to accept a trade-off between desired bandwidth and system engineering efficiency.

Following the guidelines drawn by [3], we propose to employ more than one type of source during the same seismic survey, together representing a Dispersed Source Array (DSA). Each DSA source unit involved in the acquisition is dedicated to a certain particular frequency bandwidth without the need to satisfy the seismic wideband requirement, thus avoiding the abovementioned trade off. As a whole, the ensemble of sources incorporated in the array is designed to cover the entire temporal and spatial bandwidth of seismic interest.

The employment of low-frequency sources in seismic acquisition has also been proposed by [4] and by [5], mainly as a supplement to conventional broadband acquisition. On the other hand, an interesting first experiment of DSA land data acquisition and inversion (FWI-based) has been carried out and presented by [6], utilizing standard vibrators.

The DSA concept could enhance the operational flexibility of the system, since for the higher frequencies we could think of utilizing much smaller devices. Such devices are allowed to be less powerful emitting only the required amount of energy, provided that the signal-to-noise requirements are met. This characteristic would also make them more suitable to comply with the strict regulations that apply in marine environment. Additionally, dedicated source intervals and source depths can be adopted for each type of device with beneficial implications. In the following sections these benefits are studied in detail. A brief theoretical illustration of the DSA concept and a numerical example of 3D blended DSA data migration are also provided.

2.2. BENEFITS OF DISPERSED SOURCE ARRAY ACQUISITIONS

To illustrate the concept, four different source unit types are utilized: *ultralow*- (from 2 Hz to 6 Hz), *low*- (from 5 Hz to 15 Hz), *mid*- (from 10 Hz to 30 Hz) and *high*-frequency sources (from 20 Hz to 60 Hz). Note that each source type spans a frequency bandwidth corresponding to the same number of octaves. In such situation, given bandwidths are partially overlapping for a relatively small range of frequencies. This characteristic will simplify the treatment of the data both for deblending (i.e. source separation) and ultimately direct processing. In Figures 2.1 and 2.2, the amplitude spectra of aforementioned sources are shown (top). Correspondent examples of acoustic energy propagation in a homogeneous medium together with the relative source wavelets, are presented (bottom). It is worth observing that the spectral characteristics of the proposed sources are designed to guarantee flat amplitude conditions in the whole frequency band of interest. Nevertheless, as long as the signal-to-noise ratio is acceptable, this is not essential.
In the following paragraphs, a description of the main benefits of DSA acquisition systems is provided. For simplicity they have been divided in four different categories and discussed separately.

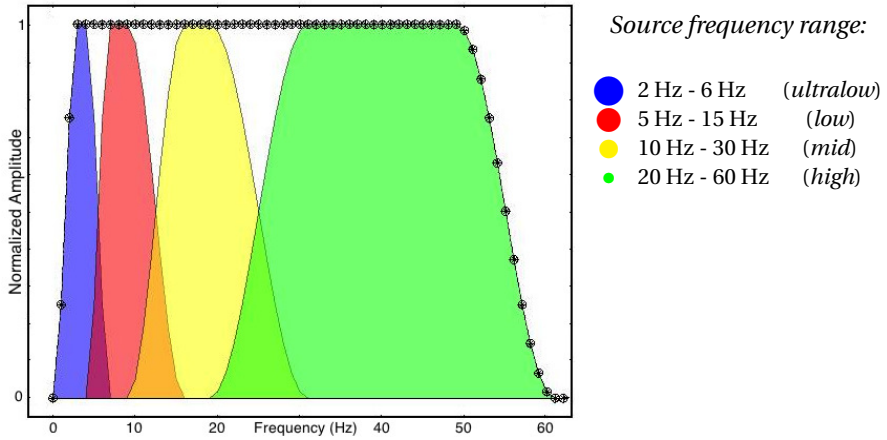

Figure 2.1: *Amplitude spectra corresponding to the chosen source units.*

2.2.1. SAMPLING ISSUES

It is well known that the ideal alias-free spatial sampling (both on the source and on the receiver side) is achieved when the maximum wave numbers of interest are properly sampled [7]. This means that the spatial sampling Δx is required to satisfy the following inequality:

$$\Delta x < \frac{c_{\min}}{2 f_{\max} \sin\theta_{\max}}, \tag{2.1}$$

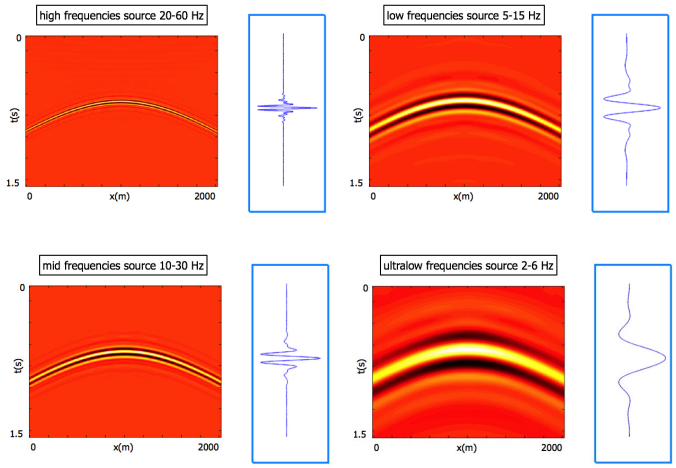

Figure 2.2: *Examples of DSA acoustic energy propagation in a homogeneous medium and corresponding source wavelets.*

where $c_{\min}$ is the minimum propagation velocity, while $f_{\max}$ and $\theta_{\max}$ are the maximum frequency and the maximum angle of the signal we aim to record, respectively. In other words, the sampling interval should be smaller than a half-period of the minimum horizontal wave length, in order to allow an accurate reconstruction of the wavefields.
Within DSA acquisition systems, each different source type has therefore specific sampling requirements. In particular, DSA acquisition systems could give us the chance to avoid oversampling on the lower frequencies side and undersampling on the higher frequencies side. In fact, the required number of source units (and shots) producing the lower significant frequencies is relatively small, provided that the signal-to-noise ratio is acceptable. Note that, regarding the low and ultralow frequencies, current acquisition geometries are excellent or even too dense, as far as spatial sampling is concerned.

2.2.2. TECHNICAL ADVANTAGES

From a technical point of view, we believe that DSA acquisitions have the potential to relax the low versus high frequency compromise. Addressing specific attention to the manufacture of different source units might, in fact, drastically improve their signal emission properties and simplify their design and production. Modern multiple-driver loudspeaker systems are based on the same key concept and their improved performances are demonstrated and widely accepted [see, for example, 8]. Furthermore, except for the very low frequencies of seismic interest, the conventional sources are significantly bigger and louder than required [9, 10]. The same applies to modern loudspeaker systems: the drivers dedicated to the reproduction of the high audible frequencies (tweeters) are considerably smaller than the drivers dedicated to the reproduction of the low frequencies (woofers).
Besides, the recent advances in unmanned systems technology and the improved operational flexibility enabled by the smaller dimensions of most DSA devices may be beneficial to the data acquisition efficiency. With DSAs, the use of relatively simple au-

tonomous devices becomes a practical proposition for seismic surveys. In a marine environment, we might consider utilizing several autonomous source boats at the same time. On land, a combination of autonomous Vibroseis trucks of varied dimensions and designs is suggested. An introductory overview on this proposition is presented by [11].

2.2.3. GHOST MATCHING

In the marine environment, seismic sources such as airgun arrays are towed at some depth z_s below the water surface. Consequently, the source wavefield not only travels downwards, but also upwards towards the air-water interface. Such interface can be considered a virtually perfect reflector with a reflection coefficient very close to -1. Thus, a secondary source is scattered back and travels downwards, delayed in time and reversed in polarity with respect to the primary. By optical analogy, aforementioned secondary source is referred to as *source ghost* and can be considered as a particular form of natural blending. For a more exhaustive explanation of the ghost problem, the reader is referred to [12]. Hereafter we will refer to the total transmitted signal as a *composite wavefield* (sum of the primary and the source ghost). The time delay between the two different acoustic wavefields is equal to $\frac{2z_s cos\Phi}{c_w}$, where Φ is the angle of incidence at the water surface and c_w is the velocity of sound in the water layer. Clearly, if $2z_s cos\Phi = (n+\frac{1}{2})\lambda_c$ (with $n \in \mathbf{N}$), the primary and source ghost wavefields will add constructively. On the other hand, if $2z_s cos\Phi = n\lambda_c$, the primary and source ghost wavefields will add destructively, requiring the use of dedicated techniques to recover lost information. Note that, in case of rough weather conditions, additional precautions need to be taken during the processing or inversion steps in order to properly address the ghost problem. In fact, the assumption of a virtually perfect reflection from the sea surface would not hold anymore. Considerable research has been and is currently conducted on this topic [e.g. 13–15].
For what concerns DSAs, extra benefits arise if we look at the ghost issue. To reduce the effect of the source ghost, each source type can be placed at the optimum depth below the water surface, i.e. at $z_s = \frac{(2n+1)\lambda_c}{4}$, one quarter of its central frequency wavelength λ_c (or at any half wavelength starting from that value). We will call this procedure *ghost matching*. This effect is illustrated in Figures 2.3 and 2.4. A 2D comparison between the composite wavefields generated by devices towed at *shallow*, optimum and *deep* levels below the water surface is shown (in the $f-k_x$ domain) for each source type including an ideal full-band unit (Figure 2.3). Here with full-band we refer to the entire bandwidth under consideration. The wavefield given by the sum of the contributions of all DSA sources is also presented (Figure 2.4). Clearly, in case of shallow tow depths the signal is greatly attenuated. When sources are towed too deep, undesired ghost notches appear in the spectrum. The DSA concept allows to reduce both complications: ghost destructive interference and notches are largely avoided and low frequency attenuation due to a too shallow tow depth can be prevented. As a result, the ghost wavefield will enhance the signal instead of compromising it, requiring simpler or no deghosting algorithms to be deployed. The overall result is definitely improved also with respect to the composite wavefield generated by the full-band device towed at its optimum depth. We could see this proposal as an optimized extension of the multilevel source arrays concept already widely developed and tested in the oil industry [see, for an overview, 16].

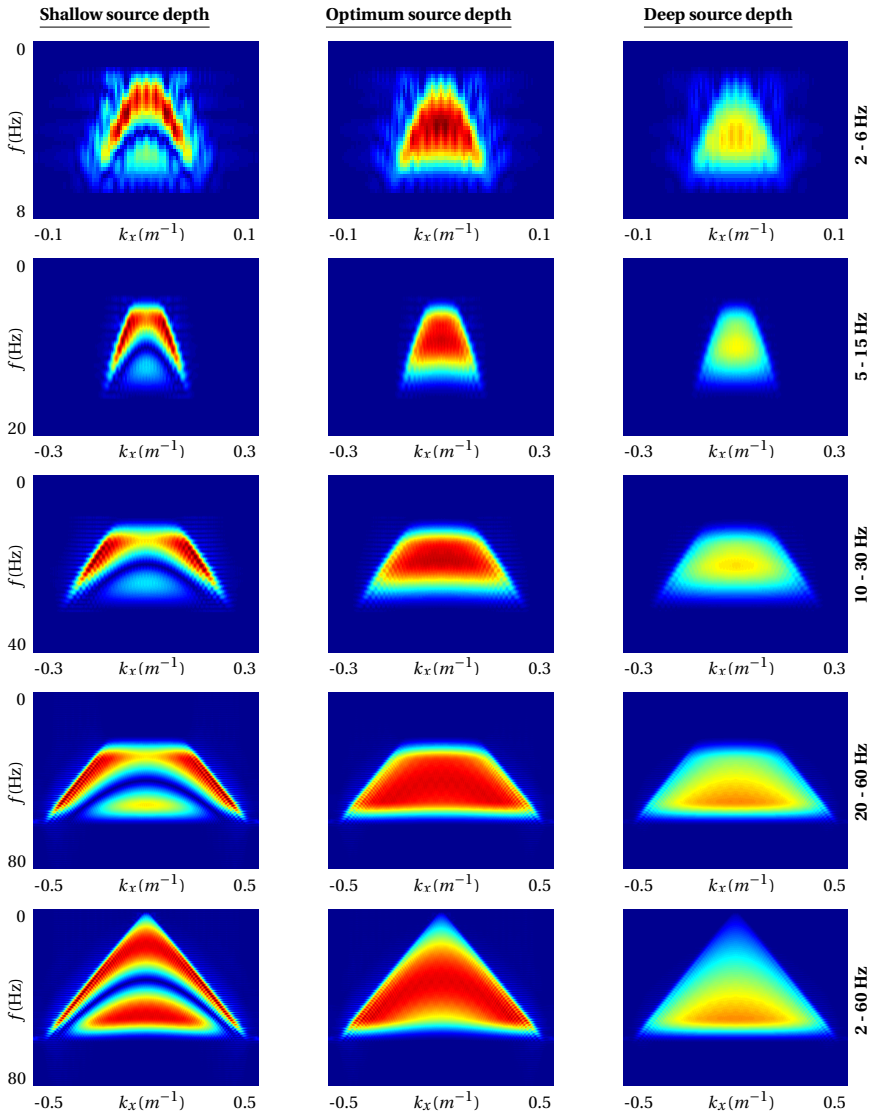

Figure 2.3: *Comparison, in the $f - k_x$ domain, between the composite wavefields generated by devices towed at shallow, optimum, and deep depth levels below the water surface for each source type, including an ideal full-band unit.*

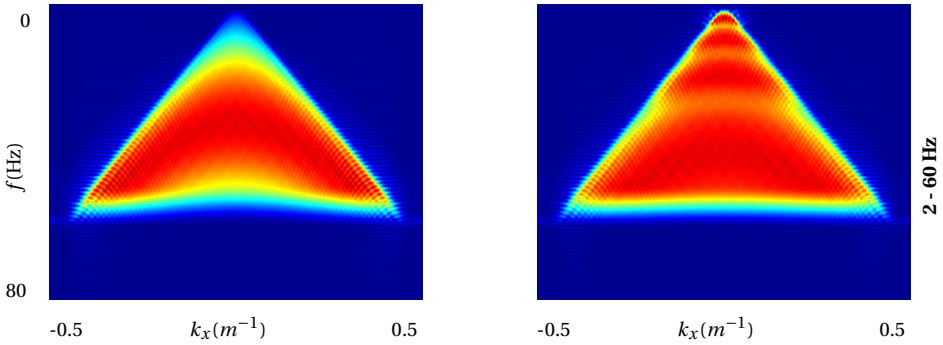

Figure 2.4: *Comparison, in the $f - k_x$ domain, between the composite wavefields generated by an ideal full-band unit towed at its optimum depth level below the water surface and the wavefield given by the sum of the contributions of all DSA sources at their respective optimum depths.*

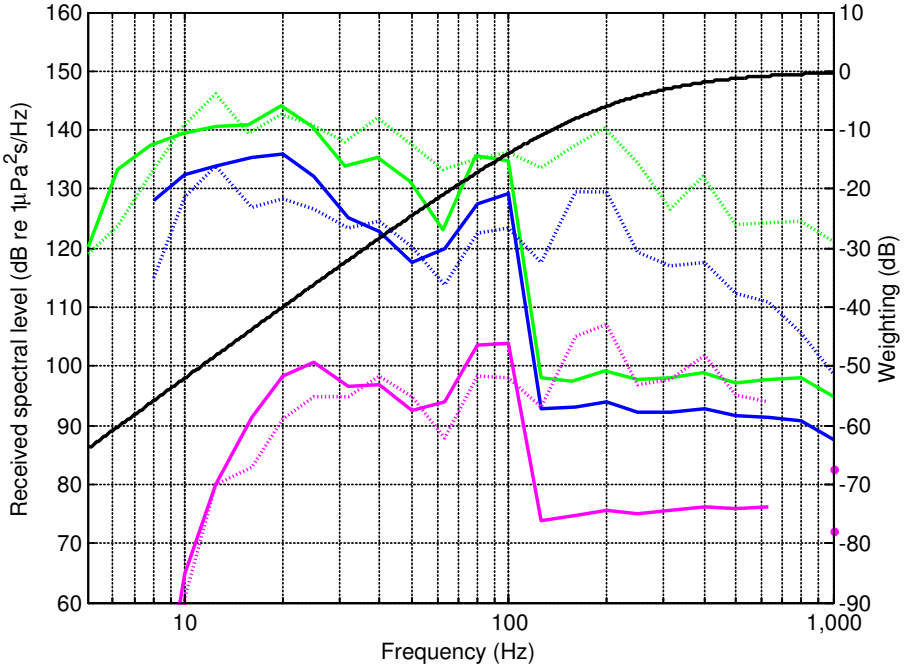

Figure 2.5: *Modelled received spectra at ranges of 1 km (green), 10 km (blue), and 100 km (red) for the marine vibrator array (solid lines) and the airgun array (dotted lines). The black curve is the high-frequency cetacean M-weighting curve from [28] (right hand axis) to give a sense of how the hearing sensitivity of these cetaceans drops off in the lower frequencies (picture and caption taken from [30] with permission from the authors).*

2.2.4. MARINE ENVIRONMENTAL ISSUES

In the last few decades, the increasing awareness and concern towards anthropologically driven environmental changes have significantly affected the way marine seismic surveys are designed. Despite important aspects of underwater bioacoustics remain unresolved, a growing number of studies have been conducted on the impact of anthropogenic noise on marine fauna [see, an overview, 17–21]. Here with anthropogenic noise we refer to all sound produced by human activities, including seismic surveys. In particular, most common undesired and potentially negative responses to the acoustic emissions due to seismic sources include acoustic masking [22] and seemingly temporary changes in behavior of marine species. Considered the complexity of ecosystem processes, the understanding of how immediate individual responses translate in large scale and long term ecological effects is currently limited. Nevertheless, the research carried on thus far has led to a considerable tightening of the regulations on aquatic life protection [23–25].

De facto, the critical parameter to take into consideration while planning a seismic survey is the signal-to-noise ratio. Here with noise we refer to the recorded signal which is unrelated to the reflection response of the controlled emitted sound. It is therefore crucial to acknowledge that there is not a generally suitable set of rules to improve the final result or to decrease the environmental impact. For instance, it is recommended to perform seismic source testing during the preliminary phases of the survey in order to assess the minimal signal strength for the area under consideration. Geological and ecological prior information may also be beneficial in this regard. It has indeed been demonstrated that in several cases, within the bandwidth of interest, the seismic source is unnecessarily too loud [9, 26]. Additionally, conventional impulsive sources, such as airguns, produce a significant amount of energy at frequency ranges that are of no benefit to seismic imaging but could potentially be harmful to aquatic life [17, 27]. Specifically, the frequency band of seismic interest (< 150 Hz) constitutes a threat to a relatively small subset of the marine fauna [28]. Note that higher frequencies considerably contribute to the total emitted energy, which is often the main parameter taken into consideration by regulators. New types of airguns have been recently designed in order to decrease the acoustic output at non-relevant frequencies without compromising the pulse shape within the seismic frequency range [29]. A greater benefit would result by the deployment of marine seismic vibrators in place of impulsive sources. See Figure 2.5 [from 30], for a realistic modeling comparison between received sound levels produced by a marine vibrator array and those from an airgun array under some typical survey scenarios. In light of these considerations we are further motivated to carry our research on DSA forward given their flexibility in terms of signal frequency emission.

Notation	Description
z_m	denotes the m^{th} depth level. Index increases with depth.
$\vec{S}(z_m)$	is the physical source wavefield at depth level z_m. Key amplitude and phase information about the spectral properties of the different DSA sources is therefore enclosed here. Each column represents one source (or source array). Each row corresponds to a different spatial coordinate.
$\vec{P}(z_m)$	is the incoming wavefield at depth z_m. In other words, it is the pressure wavefield recorded at the given depth level.
$\vec{Q}(z_m)$	is the outgoing wavefield at depth z_m. In other words, it is the pressure wavefield leaving the given depth level.
$\mathbf{R}(z_m)$	is the reflectivity operator describing the scattering occurring at depth z_m. Namely, it specifies how the incident wavefield is converted into the reflected wavefield.
$\mathbf{T}(z_m)$	is the full transmission operator at depth z_m. It can be represented as the sum of a unity matrix I and an additional term $\delta\mathbf{T}$.
$\delta\mathbf{T}(z_m)$	is the differential transmission operator at depth z_m.
$\mathbf{W}(z_l, z_r)$	is the one-way propagation operator. Each column contains a discretized Rayleigh II operator, being the vertical derivative of the Green's function describing the wave propagation between depth levels z_r and z_l.
$*^{+,-}$	denote the wavefields traveling direction (downgoing +, upgoing -).
$*^{\cap,\cup}$	denote the direction towards which the wavefields are reflected (downwards $\cap$, upwards $\cup$).
$*^{H}$	denotes the conjugate transpose of a matrix.

Table 2.1: *Overview of used notation.*

2.3. THEORETICAL FRAMEWORK

In the following, wavefield extrapolation-based modeling and inversion will be briefly discussed by means of the so called **WRW** model, introduced by [31]. Instructions on how to extend this scheme to the description of blended and DSA acquisition systems are given. Note that a dataset is considered to be blended when different sources individual responses are overlapping in space, time and both spatial and temporal frequency [32]. The domain of reference for the following theoretical consideration is the space-frequency domain. Expressions are valid for stationary receiver geometries. In Table 2.1, a description of the notation is provided. Each matrix and operator introduced below refers to a single monochromatic component of the fields.

2.3.1. THEORETICAL FRAMEWORK - MODELING

At each depth level, the total outgoing wavefield can be represented as the sum of the transmitted incoming wavefield in the same propagation direction and the wavefield reflected from the opposite direction (see Figure 2.6):

$$\mathbf{Q}^{+}(z_m) = \mathbf{T}^{+}(z_m)\,\mathbf{P}^{+}(z_m) + \mathbf{R}^{\cap}(z_m)\,\mathbf{P}^{-}(z_m), \tag{2.2}$$

$$\mathbf{Q}^{-}(z_m) = \mathbf{T}^{-}(z_m)\,\mathbf{P}^{-}(z_m) + \mathbf{R}^{\cup}(z_m)\,\mathbf{P}^{+}(z_m), \tag{2.3}$$

where

$$\mathbf{T}^{\pm}(z_m) = \mathbf{I} + \delta\mathbf{T}^{\pm}(z_m). \tag{2.4}$$

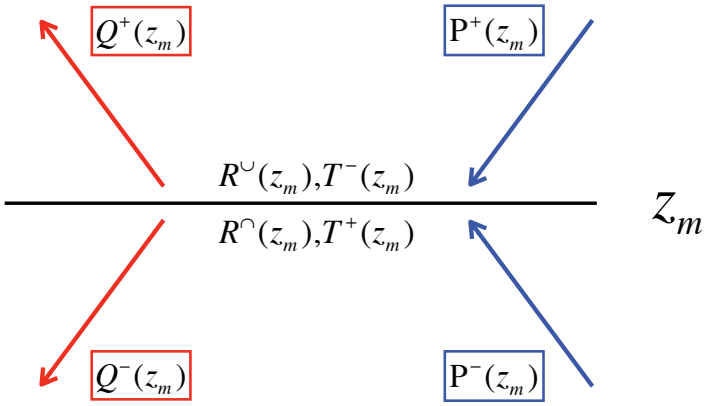

Figure 2.6: *Incoming (P) and outgoing (Q) fields at depth level z_m.*

From the above, it follows that

$$\mathbf{Q}^+(z_m) = \mathbf{P}^+(z_m) + \delta\mathbf{T}^+(z_m)\mathbf{P}^+(z_m) + \mathbf{R}^\cap(z_m)\mathbf{P}^-(z_m), \tag{2.5}$$

$$\mathbf{Q}^-(z_m) = \mathbf{P}^-(z_m) + \delta\mathbf{T}^-(z_m)\mathbf{P}^-(z_m) + \mathbf{R}^\cup(z_m)\mathbf{P}^+(z_m). \tag{2.6}$$

Note that the two last additional terms on the right of both equations account for the scattering effects and can be considered as secondary sources $\delta\mathbf{S}^\pm(z_m)$ [33]:

$$\delta\mathbf{S}^+(z_m) = \delta\mathbf{T}^+(z_m)\mathbf{P}^+(z_m) + \mathbf{R}^\cap(z_m)\mathbf{P}^-(z_m), \tag{2.7}$$

$$\delta\mathbf{S}^-(z_m) = \delta\mathbf{T}^-(z_m)\mathbf{P}^-(z_m) + \mathbf{R}^\cup(z_m)\mathbf{P}^+(z_m). \tag{2.8}$$

If we now assume small shear contrast at the interface (i.e. we neglect wave conversion), we have:

$$\mathbf{R}^\cup(z_m) = -\mathbf{R}^\cap(z_m); \qquad \mathbf{R}^\cup(z_m) = \delta\mathbf{T}^+(z_m); \qquad \mathbf{R}^\cap(z_m) = \delta\mathbf{T}^-(z_m). \tag{2.9}$$

Thus:

$$\delta\mathbf{S}^-(z_m) = \delta\mathbf{S}^+(z_m) = \delta\mathbf{S}(z_m). \tag{2.10}$$

We can, therefore, rewrite Equations 2.5 and 2.6 as follows:

$$\mathbf{Q}^{+}(z_m) = \mathbf{P}^{+}(z_m) + \delta\mathbf{S}(z_m), \tag{2.11}$$

$$\mathbf{Q}^{-}(z_m) = \mathbf{P}^{-}(z_m) + \delta\mathbf{S}(z_m). \tag{2.12}$$

After propagation, the total outgoing wavefields become incoming wavefields at the neighboring depth levels:

$$\mathbf{P}^{+}(z_m) = \mathbf{W}^{+}(z_m, z_{m-1})\,\mathbf{Q}^{+}(z_{m-1}), \tag{2.13}$$

$$\mathbf{P}^{-}(z_m) = \mathbf{W}^{-}(z_m, z_{m+1})\,\mathbf{Q}^{-}(z_{m+1}). \tag{2.14}$$

Assuming that all sources and receivers are positioned at depth level z_0, this leads us to:

$$\mathbf{P}^{+}(z_m) = \mathbf{W}^{+}(z_m, z_0)\,\mathbf{S}^{+}(z_0) + \sum_{n>0} \mathbf{W}^{+}(z_m, z_n)\delta\mathbf{S}(z_n), \tag{2.15}$$

$$\mathbf{P}^{-}(z_0) = \sum_{n>0} \mathbf{W}^{-}(z_0, z_n)\delta\mathbf{S}(z_n). \tag{2.16}$$

Utilizing this scheme, the wavefield resulting from several round trips (from the surface to an arbitrary depth level z_M and back), includes primary reflections, internal multiples and also the transmission effects. Physically also the surface multiples can be included, if the total upgoing wavefield at the surface is reinjected, after multiplication with the free surface reflectivity, as an additional downgoing wavefield. Thus, each further round trip can be described as an increment of the scattering order of the wavefield. Using this modeling approach, the so-called Full Wavefield Modeling [FWMod, see 33], we can therefore effectively add to the modeled data as many orders of multiples as necessary. Such recursive wavefield modeling approach shows strong similarities to the generalized Bremmer series [34–37].

2.3.2. THEORETICAL FRAMEWORK - INVERSION

The so-called Full Wavefield Migration algorithm [FWM, see 38, 39] aims at minimizing, by iteratively updating the reflectivities, the difference between the observed data and the data modeled with the aforementioned FWMod method. A schematic representation of the inversion loop is presented in Figure 2.7. The objective function can be described as follows:

$$J = J_\Delta + f(\mathbf{R}), \tag{2.17}$$

where the term $f(\mathbf{R})$ is a penalty function chosen based on an arbitrary constraining functional. The term J_Δ is a misfit norm function of the form:

$$J_\Delta = \sum_{\omega} \|\Delta\mathbf{P}(z_0)\|_2^2 = \sum_{\omega} Tr\left(\Delta\mathbf{P}(z_0)\,\Delta\mathbf{P}^{H}(z_0)\right), \tag{2.18}$$

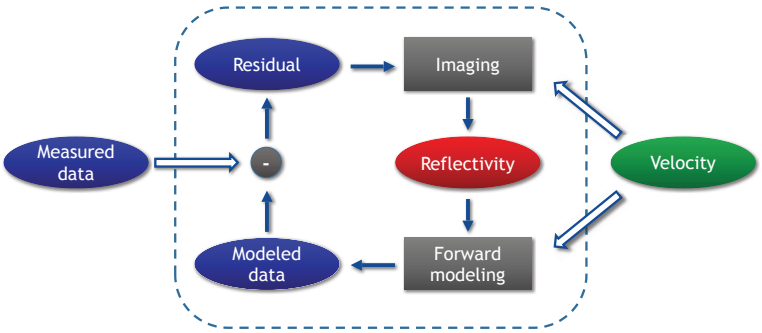

Figure 2.7: *Closed-loop for Full Wavefield Migration.*

where $\Delta\mathbf{P}(z_0)$ is the residual, i.e. the difference between the observed data $\mathbf{P}_{obs}(z_0)$ and the modeled data $\mathbf{P}^{-}_{mod}(z_0)$:

$$\Delta\mathbf{P}(z_0) \quad = \quad \mathbf{P}_{obs}(z_0) - \mathbf{P}^{-}_{mod}(z_0). \tag{2.19}$$

According to [40], the following derivative property holds while dealing with the derivative of matrix traces:

$$\frac{\partial}{\partial \mathbf{X}} Tr\left[(\mathbf{AXB}+\mathbf{C})(\mathbf{AXB}+\mathbf{C})^H\right] = 2\mathbf{A}^H(\mathbf{AXB}+\mathbf{C})\mathbf{B}^H. \tag{2.20}$$

In our case:

$$\mathbf{AXB}+\mathbf{C} = \Delta\mathbf{P}(z_0);$$

$$\mathbf{A} = -\sum_{n>0}\mathbf{W}^{-}(z_0,z_n);$$

$$\mathbf{X} = \mathbf{R}^{\cup}(z_n);$$

$$\mathbf{B} = \mathbf{P}^{+}_{mod}(z_n);$$

$$\mathbf{C} = \mathbf{P}_{obs}(z_0) - \sum_{n>0}\mathbf{W}^{-}(z_0,z_n)\delta\mathbf{T}^{-}(z_n)\mathbf{P}^{-}_{mod}(z_n). \tag{2.21}$$

This leads to:

$$\frac{\partial J_\Delta}{\partial \mathbf{R}^{\cup}(z_n)} = -2[\mathbf{W}^{-}(z_0,z_n)]^H[\Delta\mathbf{P}(z_0)]\left[\mathbf{P}^{+}_{mod}(z_n)\right]^H. \tag{2.22}$$

Thus, the total gradient driving the update of the reflectivities at each iteration of the algorithm is:

$$\frac{\partial J}{\partial \mathbf{R}^{\cup}(z_n)} \approx [\mathbf{W}^{-}(z_0,z_n)]^H [\Delta \mathbf{P}(z_0)] \left[\mathbf{P}^{+}_{mod}(z_n)\right]^H + \frac{\partial f\left(\mathbf{R}^{\cup}(z_n)\right)}{\partial \mathbf{R}^{\cup}(z_n)}. \tag{2.23}$$

Within this framework it is possible to introduce the concept of blending by defining the so-called *blending matrix* Γ_{bl} [32]. The observed and modeled data will be updated as follows:

$$\mathbf{P}_{obs}(z_0) \quad \longrightarrow \quad \mathbf{P}_{obs,bl}(z_0); \tag{2.24}$$

$$\mathbf{P}^{-}_{mod}(z_0) \quad \longrightarrow \quad \mathbf{P}^{-}_{mod}(z_0)\Gamma_{bl} \quad = \quad \mathbf{P}^{-}_{mod,bl}(z_0). \tag{2.25}$$

All information about the combination of the different sources of the array to be employed during the DSA blended experiments is encoded in Γ_{bl}. Each row of Γ_{bl} corresponds to a different source. Each column refers to a different blended shot record. In case of simple time delays between different shots, the elements of Γ_{bl} are given by $\gamma_{ik} = e^{-j\omega\tau_{ik}}$, where τ_{ik} determines the time delay relative to the i-th source for the k-th blended experiment and ω refers to the angular frequency.
The aforementioned adjustments will lead to a new misfit norm function of the form:

$$J_{\Delta,bl} \quad = \quad \sum_{\omega} \|\Delta \mathbf{P}_{bl}(z_0)\|_2^2 \quad = \quad \sum_{\omega} Tr\left(\Delta \mathbf{P}_{bl}(z_0)\, \Delta \mathbf{P}^H_{bl}(z_0)\right), \tag{2.26}$$

where $\Delta \mathbf{P}_{bl}(z_0)$ is the residual, i.e. the difference between the observed blended data $\mathbf{P}_{obs,bl}(z_0)$ and the modeled blended data $\mathbf{P}^{-}_{mod,bl}(z_0)$:

$$\Delta \mathbf{P}_{bl}(z_0) \quad = \quad \mathbf{P}_{obs,bl}(z_0) - \mathbf{P}^{-}_{mod,bl}(z_0). \tag{2.27}$$

Note that no deblending (source separation) is involved in this scheme. It follows that:

$$\mathbf{AXB} + \mathbf{C} = \Delta \mathbf{P}_{bl}(z_0);$$

$$\mathbf{A} = -\sum_{n>0} \mathbf{W}^{-}(z_0,z_n);$$

$$\mathbf{X} = \mathbf{R}^{\cup}(z_n);$$

$$\mathbf{B} = \mathbf{P}^{+}_{mod}(z_n)\Gamma_{bl};$$

$$\mathbf{C} = \mathbf{P}_{obs,bl}(z_0) - \sum_{n>0} \mathbf{W}^{-}(z_0,z_n)\delta \mathbf{T}^{-}(z_n)\, \mathbf{P}^{-}_{mod}(z_n)\Gamma_{bl}. \tag{2.28}$$

This leads to:

$$\frac{\partial J_{\Delta,bl}}{\partial \mathbf{R}^{\cup}(z_n)} = -2[\mathbf{W}^{-}(z_0,z_n)]^H[\Delta\mathbf{P}_{bl}(z_0)][\Gamma_{bl}]^H\left[\mathbf{P}^{+}_{mod}(z_n)\right]^H. \tag{2.29}$$

From a physical point of view, we can see the gradient as featured by three consecutive steps (see Figure 2.8):

$$\frac{\partial J_{\Delta,bl}}{\partial \mathbf{R}^{\cup}(z_n)} \approx \left[\mathbf{W}^{-}(z_0,z_n)\right]^H[\Delta\mathbf{P}_{bl}(z_0)][\mathbf{\Gamma}_{bl}]^H\left[\mathbf{P}^{+}_{mod}(z_n)\right]^H$$

1

2

3

Figure 2.8: *Steps for the gradient computation.*

1. Decoding [i.e. *Pseudo-deblending*, see 32] of the residual wavefield;
2. Back-propagation of the pseudo-deblended residual;
3. Cross-correlation of the back-propagated pseudo-deblended residual wavefield with the forward modeled downgoing wavefield.

2.4. NUMERICAL EXAMPLE

In this section we will demonstrate the feasibility of the DSA acquisition method with a 3D numerical example of marine seismic data migration.
The numerical example is based on the 3D SEG EAGE salt model [41]. The velocity model used as reference is shown in Figure 2.9a, while the density model is considered to be homogeneous. Note that the three visible sections of the velocity model shown in Figure 2.9a portray three orthogonal slices from inside the model. The horizontal slice (top-left) is located at $z = 750$ meters. The slice on the bottom-right is located at $x = 1000$ meters and the slice on the bottom-left corner is located at $y = 1000$ meters. The model is 2000 meters wide along both horizontal directions and 1000 meters deep.
The types of DSA sources involved in the acquisition are the ones introduced in the previous sections (see Figure 2.2). The source boats sail following straight lines parallel to both horizontal axes. The crossline spacing between neighboring lines is constant and equal to 100 meters for the ultralow-frequency sources, 50 meters for all other sources. Along the inline direction the shot interval is irregular in order to distribute the blending noise more uniformly (between 10 meters and 20 meters for the high-frequency units, between 20 meters and 30 meters for the mid-frequency units, between 30 meters and 70 meters for the low-frequency units and between 50 meters and 100 meters for the ultralow-frequency units). The sources were fired simultaneously, with a maximum blending fold

of 4. A number of 8 boats were deployed simultaneously for every source type except for the ultralow frequency sources, where 4 boats were instead deployed. Each source type has been placed at its optimum depth below the water surface, i.e. at $z_s = \lambda_c/4$.
On the receiver side, a total of 6 floating nodes is chosen. One is placed at the center of the area of interest while the others are evenly spaced around it along a circumference of 250 meters radius. Each node is positioned at a depth of 250 meters below the water surface, 50 meters above the ocean bottom. In Figure 2.9b an illustrative representation of the acquisition geometry is shown.
The receivers are recording continuously, and the result of this blended experiment is one single *supertrace* per node. The data inversion is performed without preliminary deblending. All internal multiples were utilized and not removed in the inversion process. Figure 2.10 depicts an example of the continuous signals recorded by the nodes (*supertraces*).
The results of 3D FWM after 1 and 20 iterations of the algorithm are presented in Figure 2.11. The same slices as for the velocity model are portrayed. With these acquisition settings, we do not expect to properly image the whole model, especially in the larger offsets but we can see that at the final iteration the crosstalk and the blending noise are well suppressed.

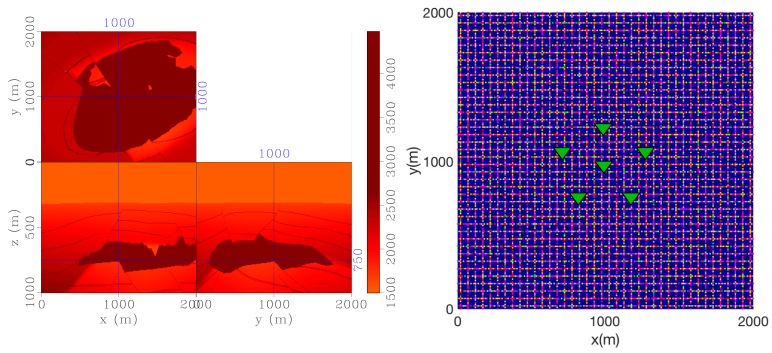

Figure 2.9: *Reference velocity model (a) and schematic illustration of the acquisition geometry (b). Note that the green triangles depict a total of 6 floating nodes. One is placed at the center of the area of interest while the others are evenly spaced around it along a circumference of 250 meters radius. Each node is positioned at a depth of 250 meters below the water surface. The colored dots represent shot locations along straight lines parallel to both horizontal axis. Different colors represent different DSA source types.*

2.5. CONCLUDING REMARKS

Particularly in the last few decades, broadband seismic acquisition has become an increasingly important topic due to its critical importance for high-resolution seismic imaging. Nevertheless acoustic sources deployed during field surveys are historically chosen to be equal and, as a consequence, often it is inevitable to accept a compromise between wave transmission properties and system engineering complexity. Usually it is necessary to settle for source sampling intervals and source depths (in marine) that are optimal

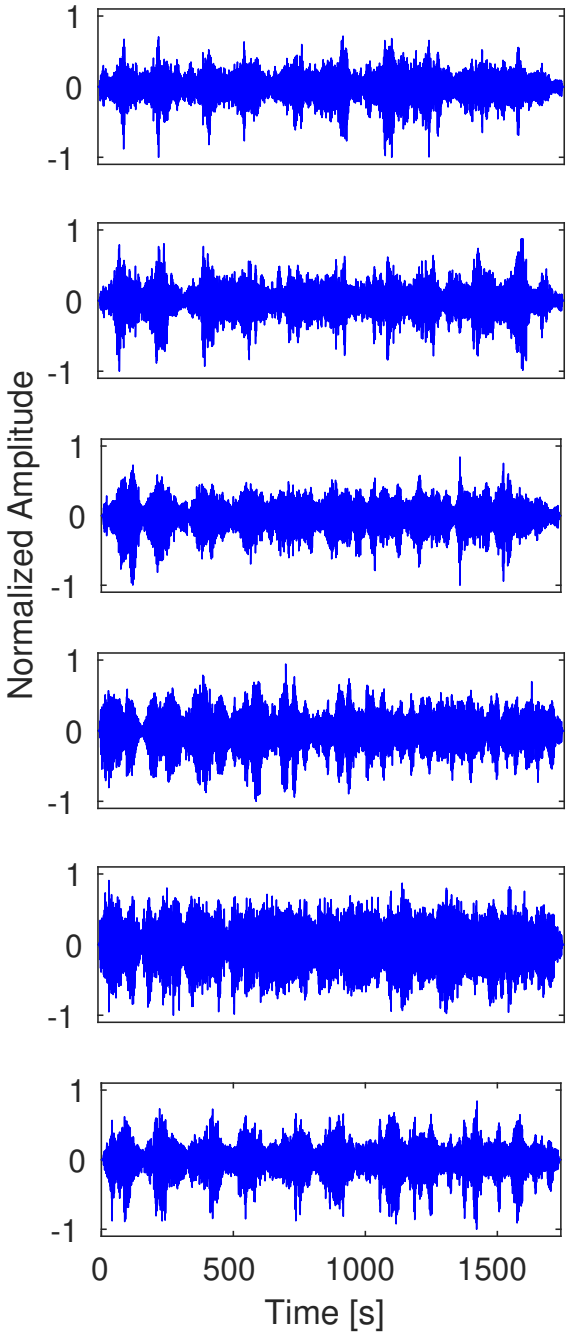

Figure 2.10: *Continuous signals recorded by the nodes (*supertraces*).*

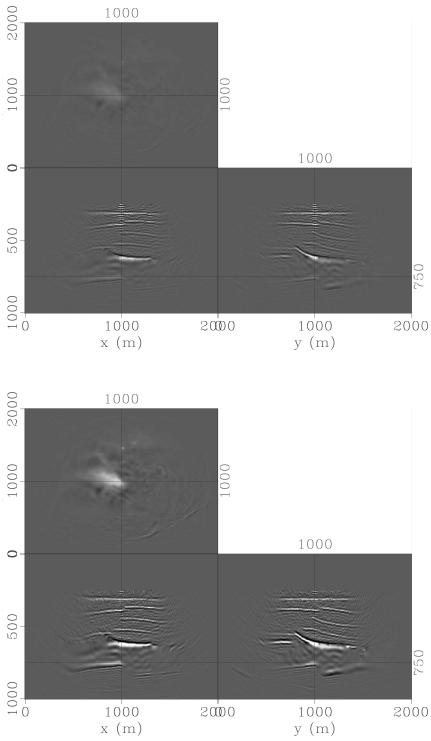

Figure 2.11: *3D images after 1 Full Wavefield Migration iteration (a) and after 20 Full Wavefield Migration iterations (b).*

only for a limited frequency range of the emitted signal.
Replacing the traditional broadband source with multiple devices transmitting a reduced and diversified frequency band offers a wide range of practical advantages, while no physical constraint prevents us from employing diverse sources with different spectral properties during seismic surveys. The whole ensemble of sources will be referred to as Dispersed Source Array (DSA).
These sources can be technically simpler to produce and more effective from an energy transmission point of view. Their utilization will allow shot densities to be chosen in a frequency dependent manner. Lower-frequency source units can be distributed more sparsely, provided that the signal-to-noise ratio is adequate. Smaller and less powerful source units may be adopted densely for the production of the higher frequencies, reducing the complexity and increasing the operational flexibility of the system as well as mitigating its environmental impact. Furthermore, in marine surveys the concept offers the possibility to tow the devices at depths that are optimum for their specific frequency range, giving extra benefits if we look at the source ghost issue. The destructive interference due to the ghost notches and the low frequency attenuation due to shallow tow depths are largely avoided.
Interesting and encouraging migration results from 3D blended DSA data have been produced with no deblending (source separation) involved in the inversion scheme.

REFERENCES

[1] M. Caporal, G. Blacquière, and M. Davydenko, *Broadband imaging via direct inversion of blended dispersed source array data,* Geophysical Prospecting **66**, 942 (2018).

[2] F. ten Kroode, S. Bergler, C. Corsten, J. W. de Maag, F. Strijbos, and H. Tijhof, *Broadband seismic data - the importance of low frequencies,* Geophysics **78**, WA3 (2013).

[3] A. J. Berkhout, *Blended acquisition with dispersed source arrays,* Geophysics **77**, A19 (2012).

[4] D. K. Reust, O. A. Johnston, J. A. Giles, and S. Ballinger, *Very low frequency seismic source,* SEG (Soc. Expl. Geophys., Expanded abstracts, 2015).

[5] J. Dellinger, A. Ross, D. Meaux, A. Brenders, G. Gesoff, J. T. Etgen, J. Naranjo, G. Openshaw, and M. Harper, *Wolfspar, an fwi friendly ultra-low-frequency marine seismic source,* SEG (Soc. Expl. Geophys., Expanded abstracts, 2016).

[6] C. Tsingas, Y. S. Kim, and J. Yoo, *Broadband acquisition, deblending, and imaging employing dispersed source arrays,* The Leading Edge **35**, 354 (2016).

[7] R. A. Niland, *Optimum oversampling,* J. Acoust. Soc. Amer. **86**, 1805 (1989).

[8] D. Davis and E. Patronis, *Sound system engineering* (Focal Press, 2006).

[9] R. M. Laws, E. Kragh, and G. Morgan, *Are seismic sources too loud?* EAGE (Eur. Ass. of Geosc. and Eng., Expanded abstracts, Rome, 2008).

[10] E. Kragh, R. Laws, J. F. Hopperstad, and A. Kireev, *Reducing the size of the seismic source with a 4C towed-marine streamer,* EAGE (Eur. Ass. of Geosc. and Eng., Expanded abstracts, Copenhagen, 2012).

[11] M. Caporal, G. Blacquière, and M. Davydenko, *3d seismic acquisition with decentralized dispersed source arrays,* SEG (Soc. Expl. Geophys., Expanded abstracts, 2016).

[12] G. Parkes and L. Hatton, *The Marine Seismic Source* (Reidel, 1986).

[13] R. Laws and E. Kragh, *Rough seas and time-lapse seismic,* Geophysical Prospecting **50**, 195 (2002).

[14] L. Amundsen, T. Røsten, J. O. A. Robertsson, and E. Kragh, *Rough-sea deghosting of streamer seismic data using pressure gradient approximations,* Geophysics **70**, V1 (2005).

[15] O. C. Orji, W. Söllner, and L. J. Gelius, *Effects of time-varying sea surface in marine seismic data,* Geophysics **77**, P33 (2012).

[16] H. Shen, T. Elboth, G. Tian, J. Warszawski, and D. Lilja, *Theoretical study on multilevel source design,* Geophysical Prospecting **62**, 1337 (2014).

[17] D. P. Nowacek, L. H. Thorne, D. W. Johnston, and P. L. Tyack, *Responses of cetaceans to anthropogenic noise,* Mammal Review **37**, 81 (2007).

[18] P. Laiolo, *The emerging significance of bioacoustics in animal species conservation,* Biological Conservation **143**, 1635 (2010).

[19] C. Erbe, J. Sisneros, F. Thomsen, A. Hawkins, and A. Popper, *Overview of the 4th international conference on the effects of noise on aquatic life,* Proc. Mtgs. Acoust. **27**, 040006 (2016).

[20] H. P. Kunc, K. E. McLaughlin, and R. Schmidt, *Aquatic noise pollution: implications for individuals, populations, and ecosystems,* Proc. Royal Soc. B **283**, 20160839 (2016).

[21] G. Shannon, M. F. McKenna, L. M. Angeloni, K. R. Crooks, K. M. Fristrup, E. Brown, K. A. Warner, M. D. Nelson, C. White, J. Briggs, S. McFarland, and G. Wittemyer, *A synthesis of two decades of research documenting the effects of noise on wildlife,* Biological Reviews **91**, 982 (2016).

[22] W. P. Tanner, *What is masking?* Journal Acoustical Society of America **30**, 919 (1958).

[23] European Union, *Directive 2008/56/ec of the european parliament and of the council of 17 june 2008 establishing a framework for community action in the field of marine environmental policy (marine strategy framework directive),* Official Journal of the European Union **L 164**, 19 (2008).

[24] MSFD, *Monitoring guidance for underwater noise in european seas,* Marine Strategy Framework Directive (MSFD) - Technical Subgroup on Underwater Noise **JRC Scientific and policy reports** (2014).

[25] NOAA, *Technical guidance for assessing the effects of anthropogenic sound on marine mammal hearing: Underwater acoustic thresholds for onset of permanent and temporary threshold shifts,* U.S. Department of Commerce and National Oceanic and Atmospheric Administration (NOAA) and National Marine Fisheries Service (NMFS) **NOAA Technical Memorandum NMFS-OPR-55** (2016).

[26] P. M. Fontana and P. Zickerman, *Mitigating the environmental footprint of towed streamer seismic surveys,* First Break **28**, 57 (2010).

[27] P. T. Madsen, M. Johnson, P. J. O. Miller, N. A. Soto, J. Lynch, and P. Tyack, *Quantitative measures of air-gun pulses recorded on sperm whales (physeter macrocephalus) using acoustic tags during controlled exposure experiments,* Journal Acoustical Society of America **120**, 2366 (2006).

[28] B. L. Southall, A. E. Bowles, W. T. Ellison, J. J. Finneran, R. L. Gentry, C. R. G. Jr, D. Kastak, D. R. Ketten, J. H. Miller, P. E. Nachtigall, W. J. Richardson, J. A. Thomas, and P. L. Tyack, *Marine mammal noise exposure criteria: Initial scientific recommendations,* Aquatic Mammals **33**, 411 (2007).

[29] E. Coste, D. Gerez, H. Groenaas, J. F. Hopperstad, O. Pramm Larsen, R. Laws, J. Norton, M. Padula, and M. Wolfstirn, *Attenuated high-frequency emission from a new design of air-gun,* SEG (Soc. Expl. Geophys., Expanded abstracts, Denver, 2014).

[30] A. J. Duncan, L. Weilgart, R. Leaper, M. Jasny, and S. Livermore, *A modeling comparison between received sound levels produced by a marine vibroseis array and those from an airgun array for some typical survey scenarios,* Marine Pollution Bulletin **119**, 277 (2017).

[31] A. J. Berkhout, *Seismic migration, imaging of acoustic energy by wave field extrapolation, A: theoretical aspects* (Elsevier, 1982).

[32] A. J. Berkhout, *Changing the mindset in seismic acquisition,* The Leading Edge **27**, 924 (2008).

[33] A. J. Berkhout, *Review paper: An outlook on the future seismic imaging, part I: forward and reverse modelling,* Geophysical Prospecting **62**, 911 (2014).

[34] H. Bremmer, *The W.K.B approximation as the first term of a geometric-optical series,* Commun. Pure Appl. Math. **4**, 105 (1951).

[35] J. Corones, *Bremmer series that correct parabolic approximations,* Journal of Mathematical analysis and applications **50**, 361 (1975).

[36] M. V. de Hoop, *Generalization of the Bremmer coupling series,* Journal of Mathematical Physics **37**, 3246 (1996).

[37] C. P. A. Wapenaar, *One-way representations of seismic data,* Geophys. J. Int **127**, 178 (1996).

[38] A. J. Berkhout, *Review paper: An outlook on the future seismic imaging, part II: Full-wavefield migration,* Geophysical Prospecting **62**, 931 (2014).

[39] M. Davydenko and D. J. Verschuur, *Full-wavefield migration: using surface and internal multiples in imaging,* Geophysical Prospecting **65**, 7 (2017).

[40] K. B. Petersen and M. S. Pedersen, *Matrix cookbook* (University of Denmark, 2012).

[41] F. Aminzadeh, J. M. Burkhard, L. Nicoletis, F. Rocca, and K. Wyatt, *Seg/eage 3-D modeling project: 2^{nd} update,* The Leading Edge **13**, 949 (1994).

3

AUTOMATED REAL-TIME PATH PLANNING FOR SEISMIC SURVEY DESIGN

Ideal seismic survey designs provide evenly sampled data complying with predefined survey specifications in terms of offset and azimuth distributions, as well as fold and trace density. Orthogonal geometries are conventionally preferred but frequently difficult to implement in the field. Specific geographical, topological and environmental factors may limit the practical implementation of traditional designs and ad-hoc adjustments may be necessary during operations. Restricted or inaccessible areas as well as obstacles in the field are, in fact, not uncommon and potentially result in poor coverage and substantial acquisition imprint.
We present two distinct automated approaches to survey design that guarantee adequate survey attributes and avoid spatial discontinuities in the recorded data, even where adverse field conditions are significant. The two methods are based on the reorganization of regular (centralized) and irregular (decentralized) source acquisition grids, respectively. Both methods provide a practical acquisition preplan for the seismic crew. We tested these techniques on a real terrain map featured by a substantial amount of inaccessible areas due to the presence of steep sand dunes. The main focus is on the source geometry. On the receiver side, the survey geometry is assumed not to be affected by the presence of the obstacles. This is the case in most practical applications.

This chapter has been submitted to to the journal *Geophysics*. Note that minor changes have been introduced to make the text consistent with the other chapters of this thesis. Coauthors: G. Blacquière, C. Tsingas and A. AlShuhail

3.1. INTRODUCTION

During field operations, it is highly unlikely to deal with perfectly smooth and fully accessible terrains. In practice, seismic acquisitions may require particular care in the preplanning phase. Obstacles and restricted areas in the field contribute to the loss of receiver and (more frequently) source positions. The resulting uneven fold distribution causes loss or duplication of offset and azimuth ranges that could critically affect the imaging and characterization of the seismic data and introduce acquisition related artifacts [1].

Typical obstacles encountered during land seismic surveys are, for instance, forests, cultivated areas, buildings, roads, wells, pipelines or particularly steep hills and sand dunes. Certain areas may be restricted due to ecological concerns (fragile ecosystems, wildlife sanctuaries, national parks) or protected for political or military reasons (conflicts, country borders, military bases). In most cases, information on the distribution of unaccessible and restricted zones in the field is available from the preliminary scouting reports. These reports may include aerial photos, satellite and topological maps, inspections and geological or geophysical observations. In this chapter, we illustrate how this information can be utilized to automatically generate a pre-plan for seismic acquisition operations. Two different methods are presented. With the first, we aim at reorganizing the predefined (centralized) source geometry around the obstacles in the field. With the second, we rely upon a decentralized approach for the coordination of seismic sources. The sources do not follow a predesigned pattern, but move in the field autonomously avoiding each other and the obstacles. The final goal is not to carry out a regular grid survey, but to meet user-defined criteria in terms, for instance, of desired fold, azimuth and offset distributions.

Both techniques can be extended to handle time variant and dynamic obstacles. In fact, despite all preliminary efforts, undetected obstacles and unexpected field conditions may emerge when the crew takes the field.

3.2. CENTRALIZATION

In centralized acquisitions, the nominal survey geometry is defined and chosen beforehand. If its choice is not governed by explicit geological objectives, 3D survey design can be viewed as a reasonably straightforward extension of 2D survey design. The source lines are generally arranged at a specific angle α with respect to the receiver lines, with the most common survey geometry being the orthogonal geometry ($\alpha = 90°$).

A number of discontinuities due to the presence of obstacles is expected and some of the shot/receiver points will need to be repositioned to minimize potential artifacts in the data. In doing so, it is often preferred to avoid sharply bending the seismic lines around the obstacle and to opt for smoothly curved lines. This procedure allows to acquire data more suitable for regularization and pre-stack migration [2]. Moreover, this approach can be beneficial also under an environmental and logistical point of view. For instance, instead of resorting to deforestation, seismic lines may wind around large trees.

The repositioning procedure is conventionally performed manually [see, for instance, 3, 4] and can be very time consuming, especially when the survey area is particularly

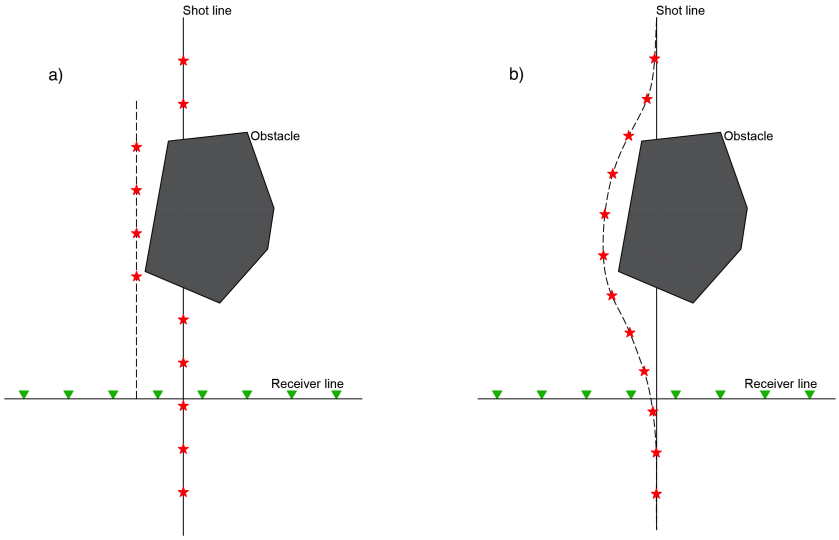

Figure 3.1: *Dealing with obstacles: to preserve spatial continuity it is preferable to reposition the missing shot positions, and few neighboring ones, along smoothly curved lines (b), rather than simply shifting them (a).*

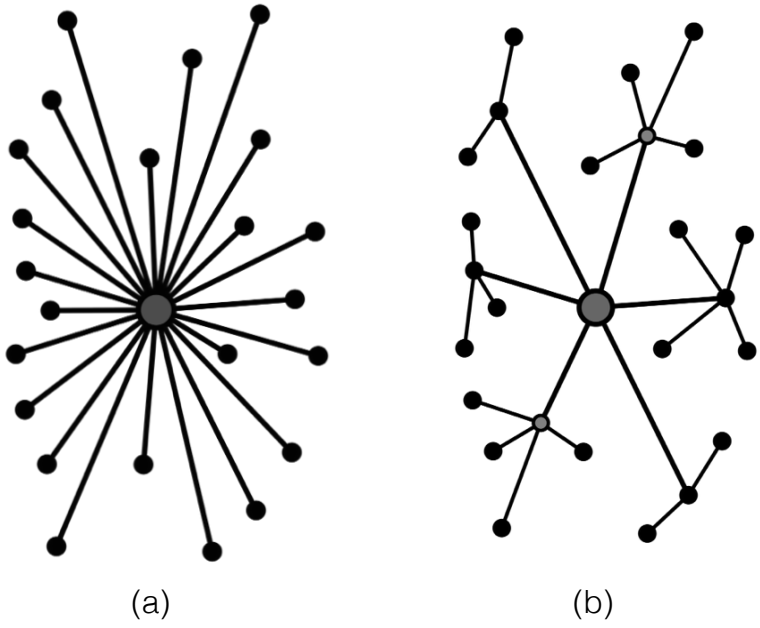

Figure 3.2: *Schematic comparison between a centralized (a) and a decentralized (b) system.*

large. The algorithm that we developed is able to handle this task automatically. Rather than shifting individual shot positions, the algorithm relocates entire portions of the shot lines in order to maintain their smoothness (Figure 3.1). In fact, especially for high resolution surveys, it is preferred to preserve the spatial continuity of the signal rather than the nominal shot positions [5].

3.3. DECENTRALIZATION

To explain the concept of decentralization, let us consider a set of interacting or interdependent components forming a more complicated and intricate system as a whole. Such a system is considered to be decentralized if complete reliance upon a single one of its elements is not required or contemplated. Functions, powers and tasks are redistributed from a central location or authority and the complex behavior of the system originates in independent decisions made by simple components operating on local information. Concepts of decentralization have been applied to a wide range of disciplines including social and political studies, economics and, of course, technology. A schematic comparison between a centralized and a decentralized system is presented in Figure 3.2.
Often, these organizational principles are inspired by nature and particularly by mutual interactions among social animals. For instance, much research has been conducted on red harvester ant colonies (*Pogonomyrmex barbatus*) which guide their global behavior using a set of patterned interactions that rely on antennal contact and olfactory sensing [6]. Observing the rate at which foragers return with food supplies and sensing olfactory cues left behind by incoming individuals, outgoing ants can determine the direction towards which they must leave the nest on foraging trips and the amount of supplies to be found at the destination. While these contacts consist of both interactions with the environment and each other, ants do not directly influence the behavior of other ants and thus never rely upon the instructions of a central controller to achieve their global goals.
In the last few decades, decentralized system architecture inspired great advances in automation technology and a new approach to the coordination and the path planning of large numbers of relatively simple robots. This branch of robotics is referred to as *swarm robotics*, emphasizing the analogy with natural sciences [7]. From an operational point of view, the reliability of a swarm coordination method can be measured on the basis of three key desired characteristics: robustness, flexibility and scalability. Robustness can be defined as the capacity of a system to tolerate failures of single system components. Flexibility can be defined as the capacity of a system to adapt to unexpected complications and dynamic environments. Scalability can be defined as the ability of a system to support a smaller or larger number of individuals without appreciably impacting its performance.
Under this perspective, an efficient and reasonably reliable real-time path planning method, which is particularly suitable for the coordination of seismic sources during operations, is the so-called *artificial potential field method* [8]. According to this approach, each source device moves in a virtual field of forces influencing the target acquisition area. The local fluctuations of the field reflect the conditions and characteristics of the area of interest. The position to be reached, in case there is any, is an attractive pole while

every obstacle in the field, including other source devices and the target area boundaries, acts as a repulsive surface (Figure 3.3). In practice, the method essentially acts as a gradient descent optimization procedure forcing the source units to avoid collisions and to remain within the boundaries of the region of interest. Outside the obstacles region of influence, the source is forced to move towards the attractive poles, for instance the recovery point or a poorly sampled area, or to move forward along its path in the absence of attractive poles. All source units are provided with a prior model describing the position of the known fixed obstacles and the target area boundaries coordinates. They are expected, however, to operate autonomously in order to promptly adapt to environmental changes (i.e. unexpected obstacles and other source units), without necessarily relying upon detailed circumstantial information beyond some limited neighborhood around their location.

From a practical perspective, a configuration $\vec{q}$ of an arbitrary object on the field (e.g. a seismic source unit) is a set of m independent parameters describing the position and the orientation of the body within an operational space of reference A. At each moment in time, the artificial force ($\vec{F}(\vec{q}) = -\vec{\nabla}\mathbf{U}(\vec{q})$) induced by the potential field at the current configuration determines the most suitable direction of motion and moving speed. The total artificial potential field $\mathbf{U}$ usually consists of the sum of an attractive potential $\mathbf{U}_{\text{att}}(\vec{q})$ pulling the seismic source units towards the target configuration $\vec{q}_{\text{att}}$, and a repulsive potential $\mathbf{U}_{\text{rep}}(\vec{q})$ pushing the devices afar from the obstacles on the fields:

$$\mathbf{U}(\vec{q}) = \mathbf{U}_{\text{att}}(\vec{q}) + \mathbf{U}_{\text{rep}}(\vec{q}). \tag{3.1}$$

The attractive potential field $\mathbf{U}_{\text{att}}(\vec{q})$ is defined as a parabolic well:

$$\mathbf{U}_{\text{att}}(\vec{q}) = \frac{1}{2}\xi\rho^2_{\text{att}}(\vec{q}), \tag{3.2}$$

where ξ is a positive scaling factor and $\rho_{\text{att}}(\vec{q}) = \| \vec{q} - \vec{q}_{\text{att}} \|$ denotes the Euclidean distance between $\vec{q}$ and the target configuration $\vec{q}_{\text{att}}$ (e.g. the source recovery point or a poorly sampled area). In particular circumstances, it may be convenient to assign a different target configuration to each seismic source unit.

The total repulsive potential field $\mathbf{U}_{\text{rep}}(\vec{q})$ can be described as a potential barrier around the obstacles that cannot be crossed by the seismic source units. Analytically, it is the sum of the repulsive potential fields generated by each individual obstacle:

$$\mathbf{U}_{\text{rep}}(\vec{q}) = \sum_{i=1}^{N_{rep}} \mathbf{U}_{\text{rep},i}(\vec{q}), \tag{3.3}$$

where $\mathbf{U}_{\text{rep},i}(\vec{q})$ is the repulsive potential field generated by the i^{th} obstacle and N_{rep} is the total number of obstacles in the survey area, including other source devices and the survey area boundaries. Each individual repulsive potential function is defined as follows:

$$\mathbf{U}_{\text{rep},i}(\vec{q}) = \begin{cases} \frac{1}{2}\eta\left(\frac{1}{\rho_{\text{rep},i}(\vec{q})} - \frac{1}{\rho_o}\right)^2 & \text{if } \rho_{\text{rep},i}(\vec{q}) \le \rho_o \\ 0 & \text{if } \rho_{\text{rep},i}(\vec{q}) > \rho_o \end{cases}, \tag{3.4}$$

where η is a positive scaling factor, $\rho_{\text{rep},i}(\vec{q}) = \| \vec{q} - \vec{q}_{\text{rep},i} \|$ denotes the Euclidean distance between $\vec{q}$ and the i^{th} obstacle configuration $\vec{q}_{\text{rep},i}$ and ρ_o represents an user-defined

limit distance beyond which the potential field has no influence on the moving sources. During seismic surveys, the source units may update their artificial potential field functions in an iterative fashion with the aid of real-time data, for instance AIS (Automatic Identification System) and sensors onboard. When available, the aid of more sophisticated tools aimed at improving the *situational awareness* [9] of the highly dynamic acquisition systems may also be beneficial. An example of a software solution that provides a spatial and temporal overview of all simultaneous operations taking place during seismic acquisitions offshore, has been presented in [10]. Geological and ecological prior information about the region of interest, as well as instructions regarding ideal illumination goals, may also be easily integrated.

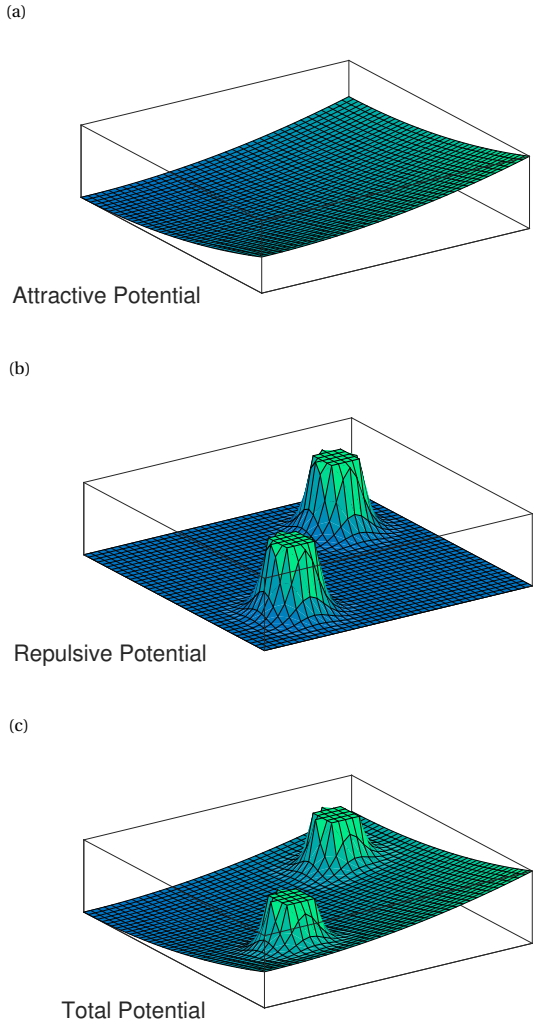

Figure 3.3: *Artificial potential field function (c) in the presence of one attractive pole (a) and two obstacles (b).*

3.4. NUMERICAL EXAMPLES

In this section, we present the application of the above-mentioned path planning method to a real terrain map featured by a substantial amount of inaccessible areas due to the presence of steep sand dunes. The elevation map of area of interest (3 km by 3 km) is shown in Figure 3.4a. Steep dune slopes may prevent seismic vibrators to operate properly, or may cause them to roll over compromising operations and safety. In order to avoid these adverse situations, the terrain elevation gradient was computed from the map. The slopes were subsequently classified in 3 different categories (Figure 3.4b): safe areas (slope below 11 degrees, in green), no vibe areas (slope between 11 and 13 degrees, in yellow), and no go areas (slope above 13 degrees, in red).
The no go areas were considered restricted areas, and thus obstacles. A potential field map was computed based on the *artificial potential field method* introduced above (Figure 3.5a). In Figure 3.5b and 3.5c, the VPs distribution for both the centralized and decentralized scenarios are respectively presented. The source line interval in the centralized case is 75 m, while the source interval is 25 m for both geometries. The simulated survey is a blended survey with 6 active vibrators in the field. As shown in Figure 3.5b and 3.5c, a specific subsection of the survey area was assigned to each different vibrator. On the receiver side, the survey geometry is assumed not to be affected by the presence of the obstacles. The receiver lines are orthogonal with respect to the nominal source lines of the centralized survey. A total of three distinct receiver geometries were taken into consideration (Figure 3.5d-f). A comparison between them in terms of acquisition attributes (fold, offsets, azimuths) is presented hereafter. For the first scenario, the receiver line interval is 75 m (Figure 3.5d). For the second scenario, the receiver line interval is 125 m (Figure 3.5e). For the third scenario, the receiver lines of the second scenario were redistributed on the field. Each line was moved to a random new location within an interval of ±62.5 m around its original position (Figure 3.5f). The receiver interval is 25 m for each of the three scenarios. Note that, the latter receiver geometry setup is based on the assumption that regular undersampling at the surface is not a sufficient, nor nec-

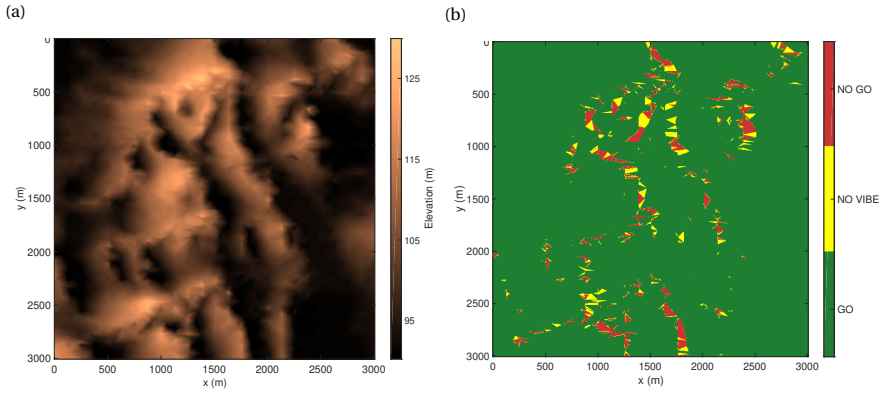

Figure 3.4: *Sand dunes terrain: elevation (a) and slope classification (b) maps.*

essary, condition both for reconstruction [11] and PSDM [12]. Hereafter, we show how our results are in line with these considerations.
In Figures 3.6-3.9, the offset, azimuth and fold distributions corresponding to each receiver geometry are compared, both for the centralized and decentralized survey geometries. For what concerns the denser receiver geometry (Figure 3.5d), both source acquisitions provide a wide range of azimuths and offsets, but only in the decentralized case, their distribution is smooth along the entire range (Figures 3.6b and 3.7b). For the centralized case, their distribution exhibits a step-like trend (Figures 3.6a and 3.7a). This is especially evident by looking at the fold distribution over a thin grid (binsize: 6.25 m, Figure 3.9a), where a square-like acquisition imprint is visible and may cause high frequency numerical artifacts, particularly for near surface studies or in case data reconstruction needs to be applied to the dataset. Nonetheless, by looking at the attribute over a thicker grid (binsize: 12.5 m, Figures 3.8a-b), we can observe that the fold distributions are fairly comparable.
If we opt for sparser receiver geometries (Figures 3.5c-d), the difference in azimuth and offset distribution between centralized and decentralized source geometries decreases sensibly (Figures 3.6c-f and 3.7c-f). However, in terms of fold distribution, the centralized source geometry is appreciably affected by the decimation with a stronger acquisition imprint (Figures 3.8c-f and 3.9c-f). Thus, among the two source acquisition designs, the decentralized approach is clearly more robust to receiver lines decimation. In addition, when a limited number of receiver lines is available, it is worth considering to distribute them in a semi-random fashion.

3.5. CONCLUSIONS

Obstacles and inaccessible areas may limit the implementation of desired seismic survey geometries in the field. To contain the acquisition related artifacts in the data, some of the shot points will need to be repositioned. While this procedure is conventionally performed manually, we propose two algorithm solutions which are able to handle this task autonomously, by reorganizing the source geometry based on regular (centralized) and irregular (decentralized) acquisition grids, respectively. These methods effectively provide acquisition geometry plans, minimizing spatial discontinuities in an automated and relatively simple fashion.
Considering the beneficial fold, azimuth and offset distributions guaranteed by decentralized source organization, it is worth considering such acquisition approach even for obstacle-free terrains. Furthermore, this technique allows to deal with dynamic field conditions more efficiently than conventional centralized design, and it can support smaller or larger groups of sources in the field without appreciable impact on its performance.

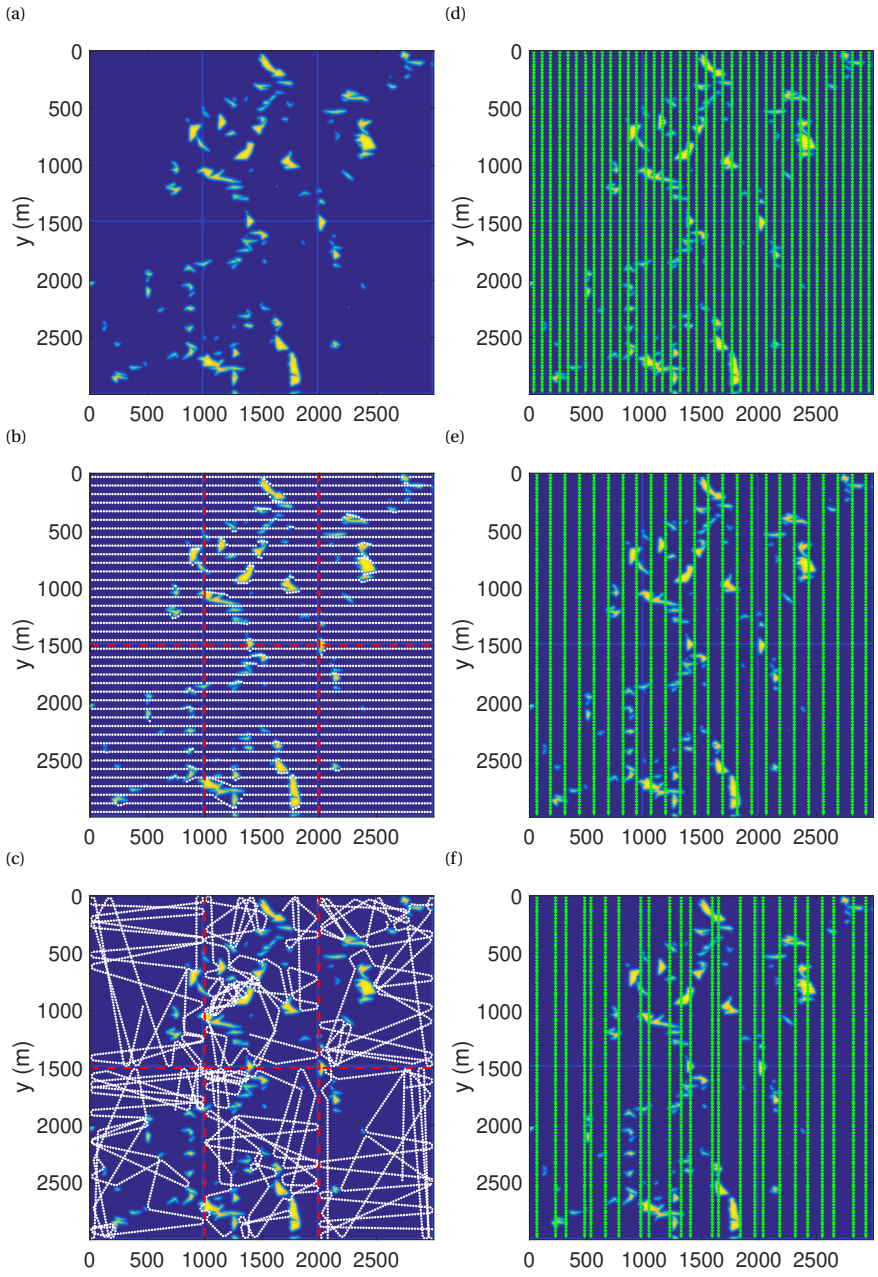

Figure 3.5: *Left column: artificial potential field map (a) and VP distribution for both centralized (b) and decentralized (c) surveys. Right column: regular* dense *(d), regular* sparse *(e) and irregular* sparse *(f) receiver lines distributions.*

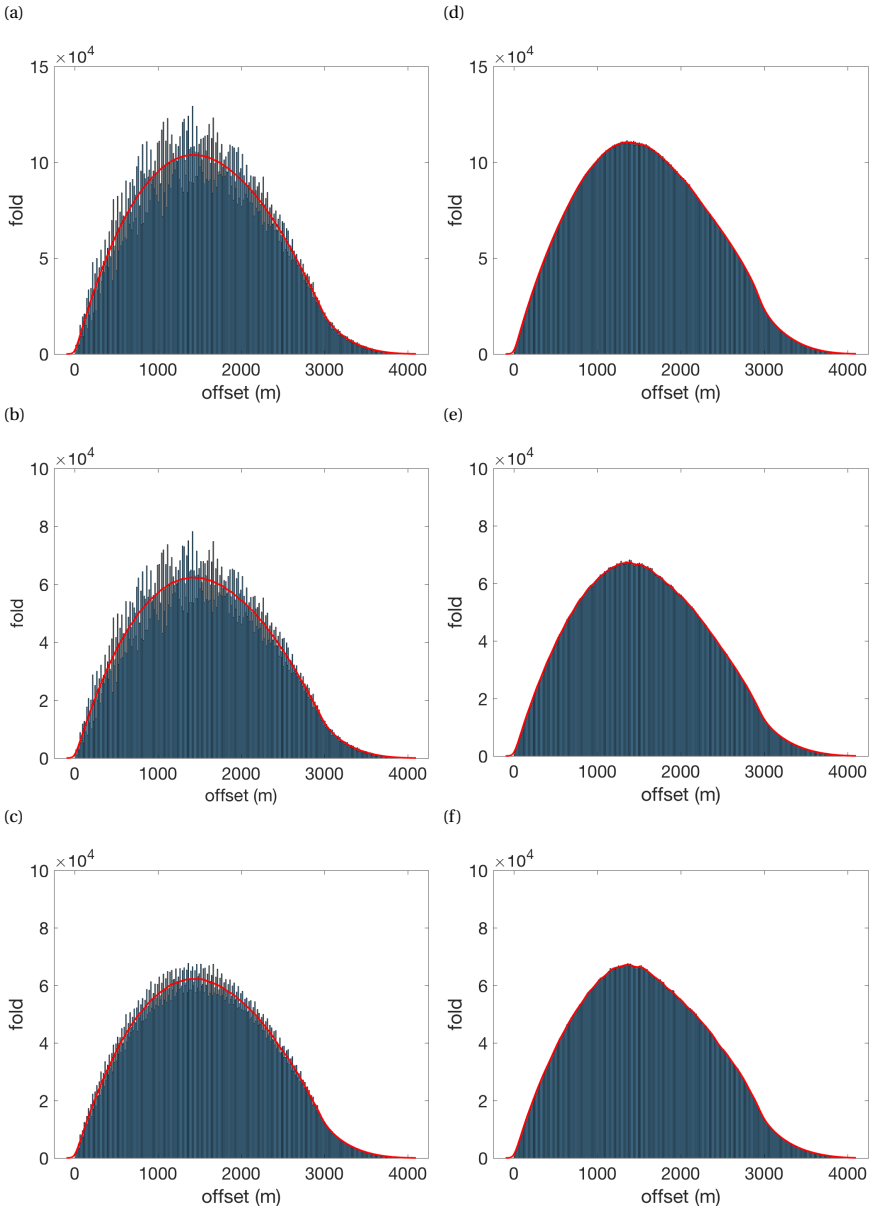

Figure 3.6: *Offset distributions for centralized (left column) and decentralized (right column) surveys. Each row is relative to a different receiver line distribution:* dense *and regular (top, line interval = 75 m);* sparse *and regular (centre, line interval = 125 m);* sparse *and semi-random (bottom). In red, the kernel density estimation of the probability density function of the samples [13].*

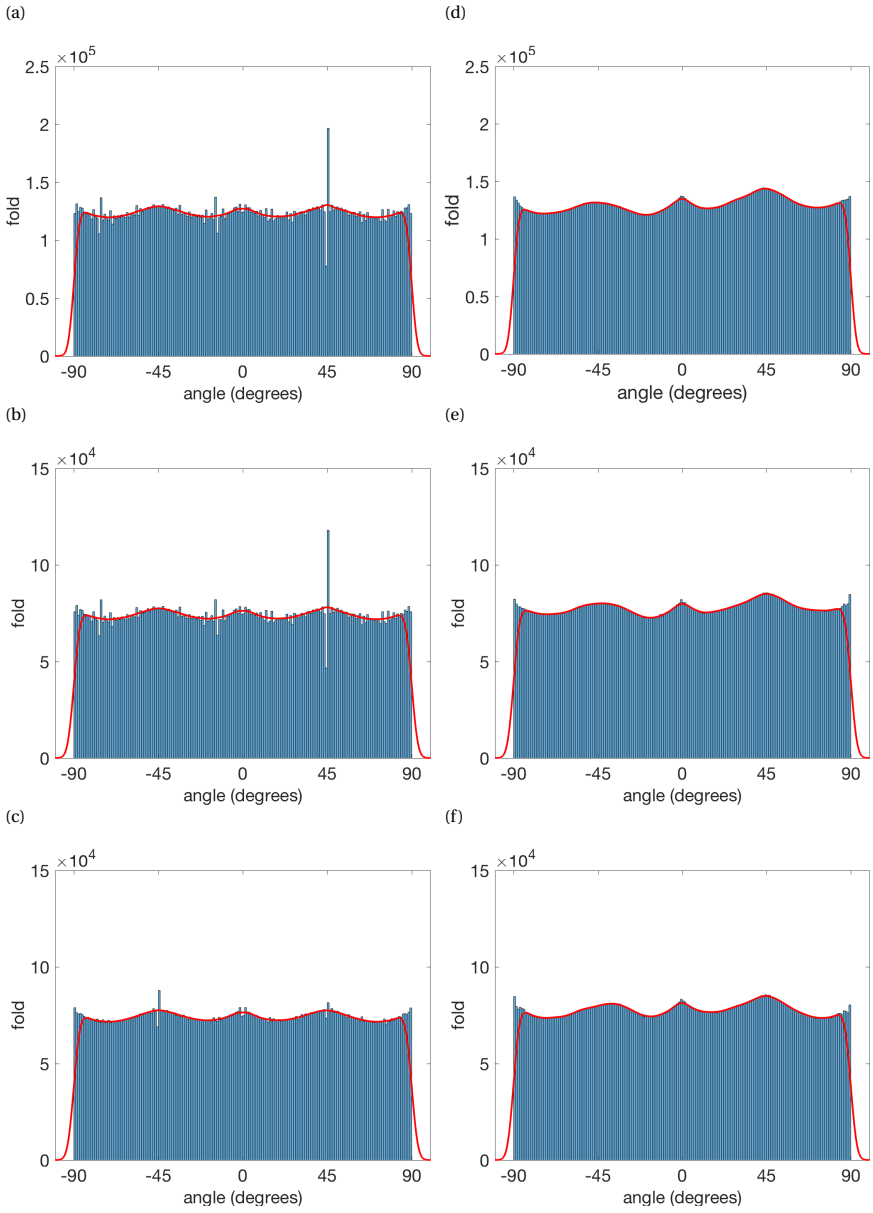

Figure 3.7: *Azimuth distributions for centralized (left column) and decentralized (right column) surveys. Each row is relative to a different receiver line distribution:* dense *and regular (top, line interval = 75 m);* sparse *and regular (centre, line interval = 125 m);* sparse *and semi-random (bottom). In red, the kernel density estimation of the probability density function of the samples [13].*

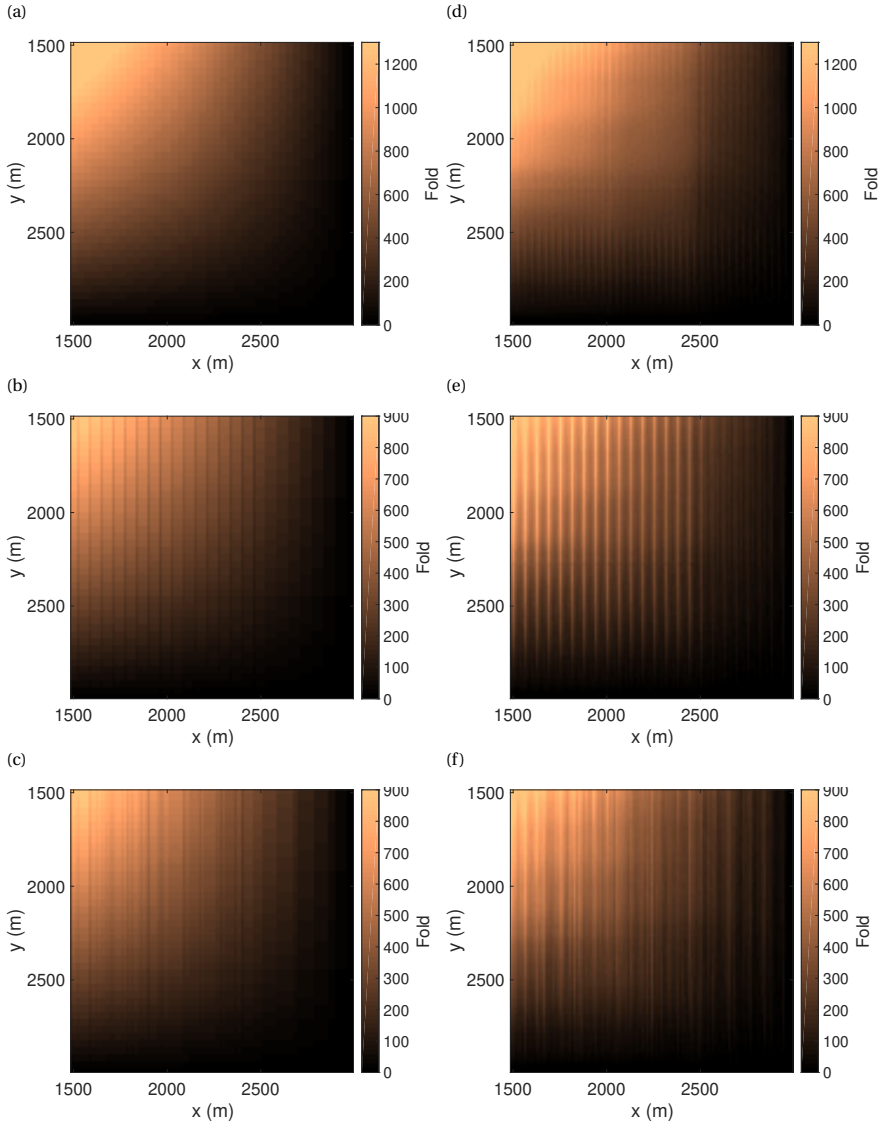

Figure 3.8: *Fold distributions (binsize = 12.5 m) for centralized (left column) and decentralized (right column) surveys. Each column is relative to a different receiver line distribution:* dense *and regular (top row, line interval = 75 m);* sparse *and regular (central row, line interval = 125 m);* sparse *and semi-random (bottom row). Note that, for better visualization and without loss of generality, a zoom of the bottom-right corner of the survey area is presented.*

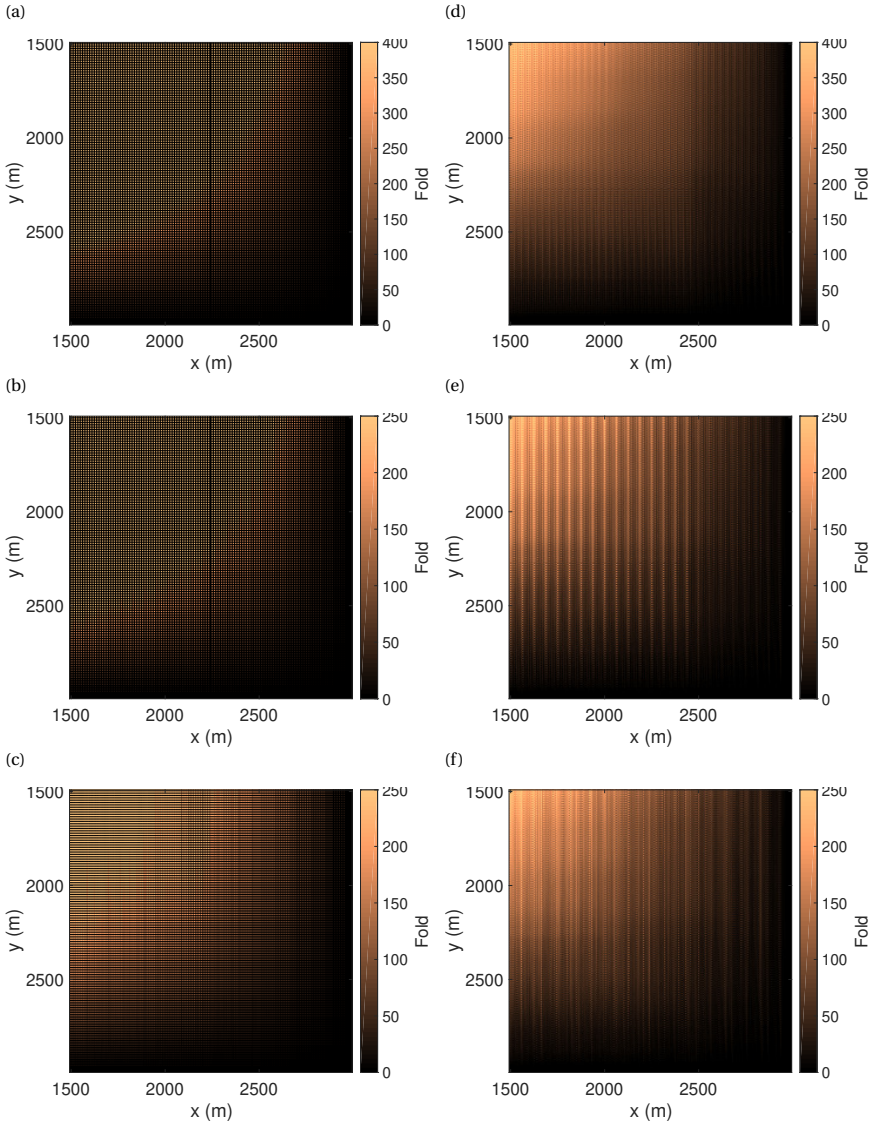

Figure 3.9: *Fold distributions (binsize = 6.25 m) for centralized (left column) and decentralized (right column) surveys. Each column is relative to a different receiver line distribution:* dense *and regular (top row, line interval = 75 m);* sparse *and regular (central row, line interval = 125 m);* sparse *and semi-random (bottom row). Note that, for better visualization and without loss of generality, a zoom of the bottom-right corner of the survey area is presented.*

REFERENCES

[1] K. J. Marfurt, R. M. Scheet, J. A. Sharp, and M. G. Harper, *Suppression of the acquisition footprint for seismic sequence attribute mapping,* Geophysics **63**, 830 (1998).

[2] J. P. Lindsey, *Crooked lines and taboo places: What are the rules that govern good line layout?* The Leading Edge **10**, 74 (1991).

[3] P. S. Wood, S. Pettersson, D. Gibson, and W. Rowe, *Seria high resolution 3d survey revives the fortunes of a mature oilfield,* SEG (Soc. Expl. Geophys., Expanded abstracts, 1999).

[4] C. B. Harrison, P. Sokol, and P. Thacker, *Geographic information systems for seismic pathway optimization,* SEG (Soc. Expl. Geophys., Expanded abstracts, 2018).

[5] G. J. O. Vermeer, *3d seismic survey design optimization,* The Leading Edge **22**, 934 (2003).

[6] D. M. Gordon, *Ants At Work: How An Insect Society Is Organized* (Free Press, 1999).

[7] L. Bayındır and E. Şahin, *A review of studies in swarm robotics,* Turkish Journal of Electrical Engineering and Computer Sciences **15**, 115 (2007).

[8] O. Khatib, *Real-time obstacle avoidance for manipulators and mobile robots,* International Journal of Robotics Research **5**, 90 (1986).

[9] M. R. Endsley, *Toward a theory of situation awareness in dynamic systems,* Human Factors **37**, 32 (1995).

[10] G. Pemberton, S. Darling, C. Koehler, and E. McDonald, *Managing simultaneous operations during seismic acquisition,* First Break **33**, 75 (2015).

[11] G. Hennenfent and F. J. Herrmann, *Simply denoise: Wavefield reconstruction via jittered undersampling,* Geophysics **73**, V19 (2008).

[12] S. Gesbert, *From acquisition footprints to true amplitude,* Geophysics **67**, 684 (2002).

[13] M. Rosenblatt, *Remarks on some nonparametric estimates of a density function,* The Annals of Mathematical Statistics **27**, 832 (1956).

4

DECENTRALIZED DISPERSED SOURCE ARRAY ACQUISITION, IMAGING AND TIME-LAPSE APPLICATIONS

In Dispersed Source Array (DSA) acquisition, traditional broadband seismic sources are replaced (or supplemented) by dedicated narrower-band devices with different central frequencies, blended together to cover the entire temporal and spatial bandwidth of interest. Taking into account the ever-increasing productivity of acquisition crews, this concept, combined with recent advances in unmanned systems technology, may be remarkably beneficial to the data acquisition efficiency. In fact, with DSA the use of relatively simple autonomous devices becomes a practical proposition for seismic surveys. For instance, the devices dedicated to the generation of the higher frequencies may be smaller and less powerful than the conventional broadband sources, providing the acquisition system with an increased operational flexibility, other than mitigating its environmental impact. In a marine environment we might consider employing several autonomous DSA source vessels at the same time, while on land a combination of autonomous DSA source vehicles of varied dimensions and designs is suggested. This chapter presents a real-time decentralized and automated approach to path planning and seismic acquisition design called artificial potential field method. *The method proves to be particularly suitable for managing and organizing several sources simultaneously operational in the field. Based on theoretical considerations and numerical data inversion and imaging examples, the feasibility and effectiveness of this approach to acquisition design are demonstrated. Additionally, we show that it is also possible to reliably recover time-lapse information despite the significant mismatch between baseline and monitor survey geometries introduced by the decentralized acquisition method.*

This chapter has been submitted to to the journal *Geophysical Journal International*. Note that minor changes have been introduced to make the text consistent with the other chapters of this thesis. Coauthors: G. Blacquière, S. Qu and M. Davydenko.

4.1. INTRODUCTION

The past decade has seen some substantial growth in the interest towards the Dispersed Source Array (DSA) acquisition method [1–3]. With this novel technology, geophysicists aim at acquiring more effectively broadband seismic data in order to improve the image quality and facilitate reservoir characterization. It is, in fact, widely accepted that the contribution of both high and low frequencies is of fundamental importance for high-quality seismic data analysis. On one hand, high frequencies reduce the width of the main lobe of the seismic wavelet, enhancing the resolution of seismic images and mitigating the interference between neighboring seismic events. On the other hand, low frequencies decrease the amplitude of its side lobes and guarantee better signal penetration, suffering less from scattering and absorption phenomena. In addition, thanks to the recent advances in inversion algorithms and to the ever-increasing computational power available, the need and suitability of low frequencies for Full Waveform Inversion (FWI) have considerably grown. An interesting and detailed overview on the importance of broadband data acquisition and processing is presented by [4].

Currently, the conventional methodology to acquire broader-bandwidth data consists of utilizing broadband sources. From a practical point of view, a significant effort is required to profitably produce and operate such sources and often it is unavoidable to accept a trade-off between transmission efficiency, costs and operational flexibility. With DSAs, traditional broadband sources are replaced (or supplemented) by a variety of devices individually transmitting diverse and reduced frequency bands and covering together the entire bandwidth of seismic interest. Addressing specific attention to the manufacture of different narrowband source units can drastically improve their signal emission properties and simplify their production. Multiple-driver loudspeaker systems are based on the same key concept and their improved performances are demonstrated [see, for example, 5]. Furthermore, the devices dedicated to the transmission of the higher frequencies may be smaller and less powerful than conventional sources [e.g. 6, 7], providing the acquisition system with increased operational flexibility. In fact, higher frequency sources would then constitute the major part of the acquisition system, considering that the minimum alias-free spatial sampling is inversely proportional to the maximum emitted frequency. Provided that the signal-to-noise ratio is acceptable, the required number of source units (and/or shots) generating the lower significant frequencies is instead relatively small. The concept received growing attention in the last years and new FWI-friendly ultralow-frequency (~ 1-10 Hz) seismic sources have already been developed both for land and offshore environments [8, 9].

However, with an eventually larger number of devices simultaneously deployed in the field, it is convenient to rethink the organizational principles on which survey design is traditionally based. We propose to look at seismic acquisition as a challenging coordination problem to be addressed in an automated and decentralized manner. The individually simple components of the acquisition system (DSA source vessels in marine and DSA vehicles on land) are expected to make autonomous decisions to achieve a global task as a whole (acquiring a well-sampled dataset), without detailed circumstantial information beyond some limited neighborhood around their position. In particular, every unit must be able to modify in real-time its own behavior (the moving speed and

direction) in order to promptly adapt to environmental changes, such as the presence of an unexpected obstacle on its path. To do so, we chose a specific decentralized approach called *artificial potential field method* [10] which proves to be particularly flexible in such situations. Each obstacle on the field (including the other sources) is considered as a repulsive potential pole, and the position to be reached (e.g. the recovery point, a poorly covered area) is treated as an attractive potential pole. The sum of these forces generates a virtual potential field and each seismic source unit is essentially a body under its influence (see Chapter 2, this thesis). In practice, this potential automatically forces the source units to avoid collisions and to remain within the boundaries of the region of interest.
In the following sections, after a theoretical introduction, we will first present a numerical example of inversion of 3D decentralized DSA data, using the *Full Waveform Migration* method [FWM, 11]. Further, we show that, by choosing the *Simultaneous Joint Migration Inversion* method [SJMI, 12], it is possible to efficiently deal with the significant changes in the survey geometry introduced by the non-repeatable nature of the suggested acquisition approach.

4.2. THEORETICAL FRAMEWORK

Notation	Description
z_n	denotes the n^{th} depth level. Index increases with depth.
$\vec{S}(z_n)$	is the physical source wavefield at depth level z_n. Key amplitude and phase information about the spectral properties of the different DSA sources is enclosed here. No propagation and scattering effects are included.
$\vec{P}(z_n)$	is the incoming wavefield at depth z_n. In other words, it is the pressure wavefield approaching the given depth level.
$\vec{Q}(z_n)$	is the outgoing wavefield at depth z_n. In other words, it is the pressure wavefield leaving the given depth level.
$\mathbf{R}(z_n)$	is the reflectivity operator describing the scattering occurring at depth z_n. Namely, it specifies how the incident wavefield is converted into the reflected wavefield.
$\mathbf{T}(z_n)$	is the transmission operator at depth z_n.
$\mathbf{W}(z_l, z_r)$	is the one-way propagation operator. Each column contains a discretized Rayleigh II operator, being the vertical derivative of the Green's function describing the wave propagation between depth levels z_r and z_l.
$*^{+,-}$	denote the wavefields traveling direction (downgoing +, upgoing -).
$*^{\cap,\cup}$	denote the direction towards which the wavefields are reflected (downwards $\cap$, upwards $\cup$).
$*^{H}$	denotes the conjugate transpose of a matrix/vector.

Table 4.1: Overview of used notation.

In the following, we will describe the theoretical framework behind the modeling and inversion engines chosen to validate the efficacy of the proposed acquisition methodology. The derivations follow the so-called *WRW* operator notation in the temporal frequency domain [13–15]. Utilizing this formulation to forward model seismic data, we are able to fully explain the kinematic effects of wave propagation based on the background velocity model alone, while the scattering effects are entirely described by the reflectivity model of the subsurface. Based on this approach, acoustic wave propagation in a source-free, inhomogeneous, isotropic half-space is described by wavefield extrapolation, which is in

practice represented by the Rayleigh integral. Instructions on how to extend this scheme to the description of *blended* [16] and DSA acquisition systems are provided. Hereafter a dataset is considered to be blended when the individual responses of different sources are overlapping in space, time and both spatial and temporal frequency. Each vector, matrix and operator introduced below refers to a single monochromatic component of the fields. Due to the orthogonality of the Fourier basis, every frequency component can be modeled or inverted for separately. Expressions are valid for stationary receiver geometries. In Table 4.1, a description of the notation is provided.

4.2.1. THEORETICAL FRAMEWORK - MODELING

Hereafter, the so-called *Full Waveform Modeling* algorithm is introduced [FWMod, see 17]. In general, at each depth level, the total outgoing wavefield can be represented as the sum of three different elements (Figure 4.1):

- a physical source [$\vec{S}^{\pm}(z_m)$];
- the energy transmitted by the wavefield incoming from the same propagation direction [$\mathbf{T}^{\pm}(z_m)\vec{P}^{\pm}(z_m)$];
- the energy reflected by the wavefield incoming from the opposite propagation direction [$\mathbf{R}^{\cap}(z_m)\vec{P}^{-}(z_m)$ *or* $\mathbf{R}^{\cup}(z_m)\vec{P}^{+}(z_m)$].

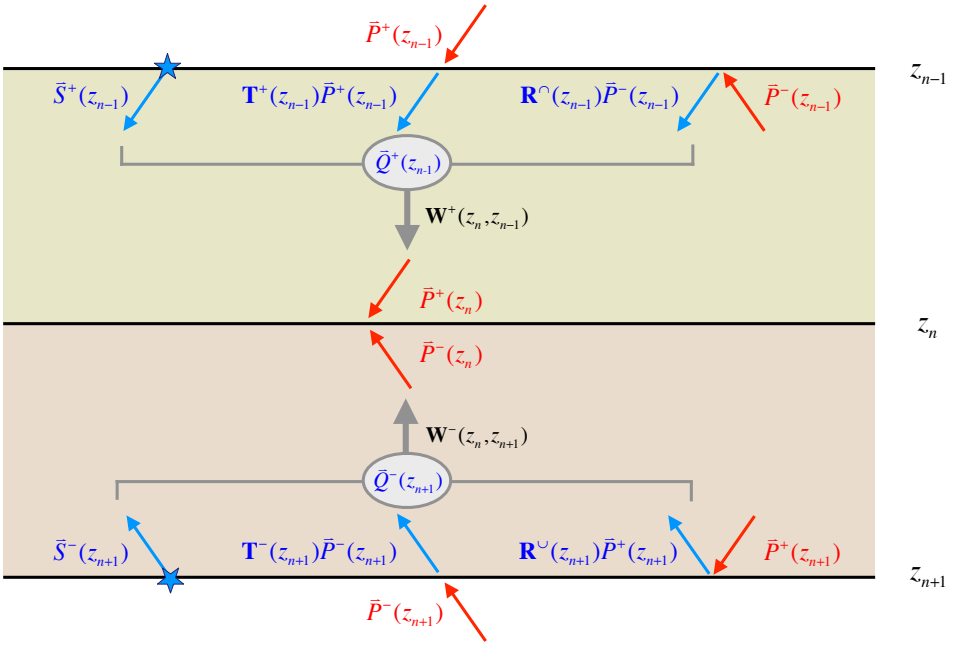

Figure 4.1: *Graphic representation of the modeling scheme. In blue, the wavefields leaving the given depth levels. In red, the wavefields approaching the given depth levels.*

In practice, we can write:

$$\vec{Q}^{+}(z_n) = \vec{S}^{+}(z_n) + \mathbf{T}^{+}(z_n)\,\vec{P}^{+}(z_n) + \mathbf{R}^{\cap}(z_n)\,\vec{P}^{-}(z_n), \tag{4.1}$$

$$\vec{Q}^{-}(z_n) = \vec{S}^{-}(z_n) + \mathbf{T}^{-}(z_n)\,\vec{P}^{-}(z_n) + \mathbf{R}^{\cup}(z_n)\,\vec{P}^{+}(z_n). \tag{4.2}$$

For this study we will actually assume that:

$$\vec{S}^{+}(z_n) = \delta_{ns}\,\vec{S}^{+}_{w}, \tag{4.3}$$

$$\vec{S}^{-}(z_n) = \delta_{ns}\,\vec{S}^{-}_{w}, \tag{4.4}$$

with δ_{ns} being a Kronecker delta function defined as follows:

$$\delta_{ns} = \begin{cases} 1 & \text{if } z_n = z_s \\ 0 & \text{if } z_n \neq z_s \end{cases}, \tag{4.5}$$

where z_s is the depth level of the physical source and $\vec{S}^{\pm}_{w}$ is the seismic source signal. After propagation, as described in Figure 4.1, the outgoing wavefields become incoming wavefields at the neighboring depth levels. This can be expressed in terms of matrix-vector products:

$$\vec{P}^{+}(z_n) = \mathbf{W}^{+}(z_n, z_{n-1})\,\vec{Q}^{+}(z_{n-1}), \tag{4.6}$$

$$\vec{P}^{-}(z_n) = \mathbf{W}^{-}(z_n, z_{n+1})\,\vec{Q}^{-}(z_{n+1}). \tag{4.7}$$

As suggested by Equations 4.6 and 4.7, the modeling method is implemented as a recursive process in depth. The wavefields are first extrapolated downwards, from the surface level z_0 to a user-defined maximum depth level z_N, and subsequently upwards, from the maximum depth level z_N to the surface level z_0. After the first iteration (round trip), the resulting upgoing wavefield at the surface includes the full primary reflection response while each additional round trip incorporates one extra order of multiples. In such a way, during each iteration the wavefields computed at every depth level in the previous round trip are utilized and updated. Such recursive wavefield modeling approach shows strong similarities to the generalized Bremmer series [18–21]. The values of $\vec{P}^{-}(z_n)$ are set to zero at all depth levels during the downwards extrapolation for the first round trip. For the extrapolation procedure, we assume that the wavefields incoming from outside the area of interest ($\vec{P}^{-}(z_N)$ and $\vec{P}^{+}(z_0)$) are known and, in most cases, they are considered to be equal to zero. We also assume that the reflectivity, transmission and propagation operators are known.
The operations described above can be rewritten as follows (see APPENDIX A for detailed derivations):

$$\vec{P}^{+}(z_n) = \sum_{k=0}^{n-1} \mathbf{V}^{+}(z_n, z_k)\left[\vec{S}^{+}(z_k) + \mathbf{R}^{\cap}(z_k)\,\vec{P}^{-}(z_k)\right], \tag{4.8}$$

$$\vec{P}^{-}(z_n) = \sum_{k=n+1}^{M} \mathbf{V}^{-}(z_n, z_k)\left[\vec{S}^{-}(z_k) + \mathbf{R}^{\cup}(z_k)\,\vec{P}^{+}(z_k)\right], \tag{4.9}$$

with:

$$\mathbf{V}^{+}(z_n, z_k) = \left[\coprod_{m=k+1}^{n-1} \mathbf{W}^{+}(z_{m+1}, z_m)\,\mathbf{T}^{+}(z_m)\right]\mathbf{W}^{+}(z_{k+1}, z_k), \tag{4.10}$$

$$\mathbf{V}^{-}(z_n, z_k) = \left[\prod_{m=n+1}^{k-1} \mathbf{W}^{-}(z_{m-1}, z_m)\,\mathbf{T}^{-}(z_m)\right]\mathbf{W}^{-}(z_{k-1}, z_k). \tag{4.11}$$

The symbol $\coprod$ is here defined as the reverse of the π-product:

$$\coprod_{i=0}^{M} \alpha_i = \alpha_M \cdot \alpha_{M-1} \cdot \cdots \cdot \alpha_1 \cdot \alpha_0 = \prod_{i=0}^{M} \alpha_{M-i}. \tag{4.12}$$

We will see in the next subsection how this formulation of $\vec{P}^{+}(z_n)$ and $\vec{P}^{-}(z_n)$ proves to be more convenient for the calculation of the inversion gradients than the formulation according to Equations 4.6 and 4.7.
In the acoustic case, the total wavefield must be continuous on both sides of each depth level z_n. This leads to the following expression for the transmission operators:

$$\mathbf{T}^{+}(z_n) = \mathbf{I} + \mathbf{R}^{\cup}(z_n). \tag{4.13}$$

$$\mathbf{T}^{-}(z_n) = \mathbf{I} + \mathbf{R}^{\cap}(z_n). \tag{4.14}$$

Furthermore, we know that, when neglecting wave conversion, all reflections can be fully described by a single operator $\mathbf{R} = \mathbf{R}^{\cup} = -\mathbf{R}^{\cap}$.

4.2.2. THEORETICAL FRAMEWORK - INVERSION

With the so-called *Joint Migration Inversion* [JMI, see 22] we aim at minimizing, by iteratively updating the reflectivity and velocity models, the difference between the observed data and the data modeled with the aforementioned FWMod method. A schematic representation of the inversion loop is presented in Figure 4.2. The objective function J can be described as follows:

$$J = J_\Delta + J_f, \tag{4.15}$$

where the term J_f is a constraining functional chosen based on user-defined constraints on the reflectivity and velocity models. The term J_Δ is a misfit norm function that can be formulated as:

$$J_\Delta = \frac{1}{2}\sum_{shots}\sum_{\omega} |f_\omega|^2 \|\Delta\vec{P}(z_0)\|_2^2, \tag{4.16}$$

where f_ω is some frequency-dependent weighting functional and $\Delta\vec{P}(z_0)$ is the data residual, i.e.:

$$\Delta\vec{P}(z_0) = \vec{P}_{obs}(z_0) - \vec{P}^{-}_{mod}(z_0). \tag{4.17}$$

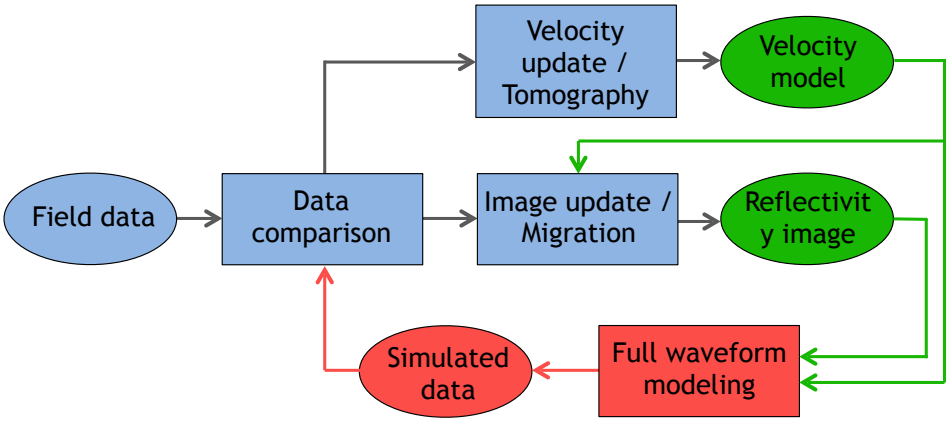

Figure 4.2: *Schematic representation of Joint Migration Inversion algorithm.*

Here, with $\vec{P}_{obs}(z_0)$ we refer to the recorded shot record after preprocessing (receiver response and statics corrections, regularizations, preliminary denoising and so on) and with $\vec{P}^{-}_{mod}(z_0)$ we refer to the modeled data. Considering that the modeled data are typically generated on a regular dense grid, it might be necessary to appropriately subsample them to match the actual receivers acquisition geometry. All receivers are assumed to be at depth level z_0.
To estimate the reflectivity updates we need to compute the gradients for the reflectivity operators $\mathbf{R}^{\cap}$ and $\mathbf{R}^{\cup}$. Namely, we have (see APPENDIX B for detailed derivations):

$$\frac{\partial J}{\partial \mathbf{R}^{\cup}(z_n)} = -\sum_{shots}\sum_{\omega} |f_\omega|^2 [\mathbf{V}^{-}(z_0,z_n)]^H \left[\Delta\vec{P}(z_0)\right]\left[\vec{P}^{+}_{mod}(z_n)\right]^H + \frac{\partial J_f}{\partial \mathbf{R}^{\cup}(z_n)}, \tag{4.18}$$

$$\frac{\partial J}{\partial \mathbf{R}^{\cap}(z_n)} = -\sum_{shots}\sum_{\omega} |f_\omega|^2 \left[\mathbf{V}^{\cup}(z_0,z_n)\right]^H \left[\Delta\vec{P}(z_0)\right]\left[\vec{P}^{-}_{mod}(z_n)\right]^H + \frac{\partial J_f}{\partial \mathbf{R}^{\cap}(z_n)}, \tag{4.19}$$

with:

$$\mathbf{V}^{\cup}(z_0,z_n) = \sum_{k=n+1}^{M} \mathbf{V}^{-}(z_0,z_k)\,\mathbf{R}^{\cup}(z_k)\,\mathbf{V}^{+}(z_k,z_n)\,. \tag{4.20}$$

Mathematically, the gradients obtained from Equations 4.18 and 4.19 represent the update directions of the gradient descent scheme but, in general, do not match the correct amplitudes. It is thus necessary to retrieve the optimal scaling parameter, α, to update

the reflectivity models more effectively. Namely, the scalar is computed by minimizing the following objective function:

$$J_\alpha = \sum_{shots} \sum_{\omega} \| \Delta \vec{P}(z_0) - \alpha \, \vec{\Psi}^-_{mod,\mathbf{R}}(z_0) \|_2^2, \tag{4.21}$$

where $\vec{\Psi}^-_{mod,\mathbf{R}}(z_0)$ is the modeled wavefield perturbation associated with the reflectivity gradient. Consequently, the scalar factor α is given by:

$$\alpha = \frac{\sum_{shots} \sum_{\omega} \Delta \vec{P}^H(z_0) \, \vec{\Psi}^-_{mod,\mathbf{R}}(z_0)}{\sum_{shots} \sum_{\omega} \| \vec{\Psi}^-_{mod,\mathbf{R}}(z_0) \|_2^2}. \tag{4.22}$$

4

Within this framework it is possible to introduce the concept of blending by defining the so-called blending operator $\vec{\Gamma}_{bl}$ [16]. In that case, the observed and modeled data will be updated as follows:

$$\vec{P}_{obs}(z_0) \quad \longrightarrow \quad \vec{P}_{obs,bl}(z_0), \tag{4.23}$$

$$\vec{P}^-_{mod}(z_n) \quad \longrightarrow \quad \mathbf{P}^-_{mod}(z_n)\vec{\Gamma}_{bl} \quad = \quad \vec{P}^-_{mod,bl}(z_n). \tag{4.24}$$

$$\vec{P}^+_{mod}(z_n) \quad \longrightarrow \quad \mathbf{P}^+_{mod}(z_n)\vec{\Gamma}_{bl} \quad = \quad \vec{P}^+_{mod,bl}(z_n). \tag{4.25}$$

Here with $\mathbf{P}^-_{mod}(z_n)$ and $\mathbf{P}^+_{mod}(z_n)$ we refer to the full unblended data matrices. In this convention, every column of $\mathbf{P}^-_{mod}(z_0)$ represents the unblended wavefield generated by a single source and recorded by all receivers, while every row represents the unblended wavefields generated by all sources and recorded at a single receiver location. All information about the combination of the different sources employed during the DSA blended experiments is encoded in $\vec{\Gamma}_{bl}$. Each element of $\vec{\Gamma}_{bl}$ corresponds to a different source. In case of simple time delays between different shots, the elements of $\vec{\Gamma}_{bl}$ are given by $\gamma_i = e^{-j\omega\tau_i}$, where τ_i determines the time delay applied to the i^{th} source and ω refers to the angular frequency under consideration.
The aforementioned adjustments will lead to a new misfit norm function of the form:

$$J_{\Delta,bl} = \frac{1}{2} \sum_{\substack{blend. \\ records}} \sum_{\omega} |f_\omega|^2 \| \Delta \vec{P}_{bl}(z_0) \|_2^2, \tag{4.26}$$

where $\Delta \vec{P}_{bl}(z_0)$ is the residual defined as follows:

$$\Delta \vec{P}_{bl}(z_0) = \vec{P}_{obs,bl}(z_0) - \vec{P}^-_{mod,bl}(z_0). \tag{4.27}$$

This leads to the following updates to the gradients:

$$\frac{\partial J}{\partial \mathbf{R}^{\cup}(z_n)} = -\sum_{\substack{blend.\\records}} \sum_{\omega} |f_\omega|^2 [\mathbf{V}^{-}(z_0, z_n)]^H [\Delta \vec{P}(z_0)] [\vec{\Gamma}_{bl}]^H [\mathbf{P}^{+}_{mod}(z_n)]^H + \frac{\partial J_f}{\partial \mathbf{R}^{\cup}(z_n)}, \quad (4.28)$$

$$\frac{\partial J}{\partial \mathbf{R}^{\cap}(z_n)} = -\sum_{\substack{blend.\\records}} \sum_{\omega} |f_\omega|^2 [\mathbf{V}^{\cup}(z_0, z_n)]^H [\Delta \vec{P}(z_0)] [\vec{\Gamma}_{bl}]^H [\mathbf{P}^{-}_{mod}(z_n)]^H + \frac{\partial J_f}{\partial \mathbf{R}^{\cap}(z_n)}, \quad (4.29)$$

No deblending (source separation) is explicitely involved in this scheme. The crosstalk from the blended acquisition will be largely resolved due to the inversion-based approach [23, 24]. From a physical point of view, ignoring the constraining functional we can see the gradient for $\mathbf{R}^{\cup}(z_n)$ as featured by three consecutive steps (see Figure 4.3):

$$\frac{\partial J_{\Delta,bl}}{\partial \mathbf{R}^{\cup}(z_n)} \approx \left[\mathbf{W}^{-}(z_0, z_n)\right]^H [\Delta \mathbf{P}_{bl}(z_0)] [\mathbf{\Gamma}_{bl}]^H \left[\mathbf{P}^{+}_{mod}(z_n)\right]^H$$

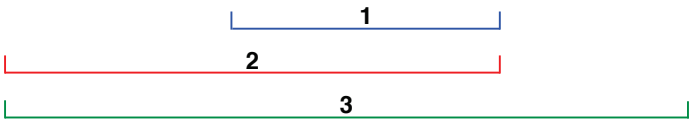

Figure 4.3: *Steps for the gradient computation.*

1. Decoding [i.e. *Pseudo-deblending*, see 16] of the residual wavefield;
2. Back-propagation of the pseudo-deblended residual wavefield;
3. Cross-correlation of the back-propagated, pseudo-deblended residual wavefield with the forward modeled downgoing wavefield.

A similar procedure applies to the gradient for $\mathbf{R}^{\cap}(z_n)$, with a slightly more complicated passage at step 2.
At this point, if a sufficiently reliable velocity model is available, we may limit the inversion to the reflectivity model. This approach is called *Full Waveform Migration* [FWM, see 11, 25]. With JMI, at each iteration the inaccurate propagation velocity model is instead corrected by updating the propagation operator, **W**. Here we are working under the assumption that the velocity model purely affects the kinematics and not the scattering effects of wave propagation. It is thus essential to relate analytically the propagation operators to the velocity model. For simplicity, we will actually deal with the slowness $s_c = \frac{1}{c}$, rather than directly with the velocity c.
In our formulation, for the 2D case the i^{th} column of the propagation operator, **W**, is defined as the inverse spatial Fourier transform of the following phase-shift operator in the wavenumber domain [13]:

$$\tilde{w}(z_n, z_m; x_i, s_c) = e^{-jk_z \Delta z} e^{jk_x x_i}, \quad (4.30)$$

where $\Delta z = z_m - z_n$, x_i is the source position of the Green's function and $k_z = \sqrt{k^2 - k_x^2}$. The wavenumber $k = \omega s_c$ is computed using the local propagation velocity $c(x_i)$ at depth $z_m + \frac{\Delta z}{2}$. Each column of $\mathbf{W}$ contains the response of a (dipolar) impulsive source positioned at depth level z_m and measured at all grid points at depth level z_n. We can now linearize the relationship between $\tilde{w}$ and s_c with the following truncated expansion:

$$\tilde{w}\left(z_n, z_m; x_i, s_{c_0} + \Delta s_c\right) \approx \tilde{w}_0 + \left[\frac{\partial \tilde{w}}{\partial s_c}\right]_{s_{c_0}} \Delta s_c = \tilde{w}_0 - j\omega\Delta z \left[\frac{k}{k_z}\right]_{s_{c_0}} \tilde{w}_0 \Delta s_c, \tag{4.31}$$

where Δs_c is the slowness update, s_{c_0} and $s_{c_0} + \Delta s_c$ represent respectively the current and updated slowness, and $\tilde{w}_0$ and $\tilde{w}\left(z_n, z_m; x_i, s_{c_0} + \Delta s_c\right)$ represent the spatial Fourier transforms of the current and updated i^{th} column of the propagation operator. Let us now define the matrix Υ with the following elements as rows:

$$v\left(z_n, z_m; x_i, s_{c_0} + \Delta s_c\right) = -j\omega\Delta z \left[\frac{k}{k_z}\right]_{s_{c_0}} \tilde{w}_0. \tag{4.32}$$

It follows:

$$\mathbf{W}^+_{l+1}(z_{n+1}, z_n) \approx \mathbf{W}^+_l(z_{n+1}, z_n) + \Upsilon^+(z_{n+1}, z_n)\,\Delta\mathbf{S}_c(z_n), \tag{4.33}$$

$$\mathbf{W}^-_{l+1}(z_n, z_{n+1}) \approx \mathbf{W}^-_l(z_m, z_{n+1}) + \Upsilon^-(z_n, z_{n+1})\,\Delta\mathbf{S}_c(z_n), \tag{4.34}$$

where $\Delta\mathbf{S}_c(z_n)$ is a diagonal matrix with the slowness updates as diagonal elements, while $\mathbf{W}^\pm_l$ and $\mathbf{W}^\pm_{l+1}$ represent the current and updated propagation operators. More explicitly, we can write:

$$\Delta\mathbf{S}_c(z_n) \approx \left[\Upsilon^+(z_{n+1}, z_n)\right]^H \Delta\mathbf{W}^+(z_{n+1}, z_n), \tag{4.35}$$

$$\Delta\mathbf{S}_c(z_n) \approx \left[\Upsilon^-(z_n, z_{n+1})\right]^H \Delta\mathbf{W}^-(z_n, z_{n+1}), \tag{4.36}$$

with $\Delta\mathbf{W}^\pm = \mathbf{W}^\pm_{l+1} - \mathbf{W}^\pm_l$.
With this in mind, let us compute the gradients for the propagation operators $\mathbf{W}^+$ and $\mathbf{W}^-$. Namely, we have (see APPENDIX B for detailed derivations):

$$\frac{\partial J}{\partial \mathbf{W}^+(z_{n+1}, z_n)} = -\sum_{shots}\sum_{\omega} |f_\omega|^2 \left[\mathbf{V}^\triangle(z_0, z_{n+1})\right]^H \left[\Delta\vec{P}(z_0)\right]\left[\vec{Q}^+_{mod}(z_n)\right]^H + \frac{\partial J_f}{\partial \mathbf{W}^+(z_{n+1}, z_n)}, \tag{4.37}$$

$$\frac{\partial J}{\partial \mathbf{W}^-(z_n, z_{n+1})} = -\sum_{shots}\sum_{\omega} |f_\omega|^2 [\mathbf{V}^\nabla(z_0, z_n)]^H \left[\Delta\vec{P}(z_0)\right]\left[\vec{Q}^-_{mod}(z_{n+1})\right]^H + \frac{\partial J_f}{\partial \mathbf{W}^-(z_n, z_{n+1})}, \tag{4.38}$$

with:

$$\mathbf{V}^{\triangle}(z_0, z_n) = \mathbf{V}^{-}(z_0, z_n)\,\mathbf{R}^{\cup}(z_n) + \mathbf{V}^{\cup}(z_0, z_n)\,\mathbf{T}^{+}(z_n), \tag{4.39}$$

and:

$$\mathbf{V}^{\triangledown}(z_0, z_n) = \mathbf{V}^{-}(z_0, z_n)\,\mathbf{T}^{-}(z_n). \tag{4.40}$$

As for the reflectivities, the gradients obtained from Equations 4.37 and 4.38 represent the inversion update directions of the gradient descent scheme but not with the correct amplitudes. It is thus necessary to retrieve the optimal scaling parameter, β, to update the slowness model more effectively. Namely, the scalar is computed by minimizing the following objective function:

$$J_\beta = \sum_{shots}\sum_{\omega} \| \Delta\vec{P}(z_0) - \beta\,\vec{\Psi}^{-}_{mod,\sigma}(z_0) \|_2^2, \tag{4.41}$$

where $\vec{\Psi}^{-}_{mod,\sigma}(z_0)$ is the modeled wavefield perturbation associated to the slowness update. Consequently, the scalar factor β is given as:

$$\beta = \frac{\sum_{shots}\sum_{\omega} \Delta\vec{P}^{H}(z_0)\,\vec{\Psi}^{-}_{mod,\sigma}(z_0)}{\sum_{shots}\sum_{\omega} \| \vec{\Psi}^{-}_{mod,\sigma}(z_0) \|_2^2}. \tag{4.42}$$

4.2.3. THEORETICAL FRAMEWORK - TIME-LAPSE SIMULTANEOUS JMI

It is well known that fluid flow and fluid substitution can significantly alter the reservoir parameters (e.g. fluid saturation, pressure and temperature) inducing changes in the elastic properties of the reservoir (e.g. bulk modulus, density) and consequently in the wave propagation velocities and the reflectivities. Time-lapse seismic, also referred to as 4D seismic, has proven to be an effective tool for monitoring this kind of dynamic variations. To do so, multiple seismic surveys are conducted in the same area at different stages of the hydrocarbon production and the differences in the seismic responses are analyzed. In conventional 4D seismic, a high degree of repeatability of the acquisition geometry is crucial to the success of the experiment [26]. However, as mentioned above, decentralized DSA surveys are non-repeatable by nature. It is thus crucial to find a robust and reliable strategy to properly handle the time-lapse datasets.
Per se, being an inversion-based method, JMI does not require baseline and monitor acquisition geometries to exactly overlap in order to accurately estimate time-lapse perturbations, provided that the subsurface illumination is adequate. In fact, by including the multiples in the imaging process we may drastically reduce the acquisition imprint on the final results [27, 28]. Furthermore, in what concerns the portion of the subsurface

that is not affected by the perturbations, time-lapse acquisition geometry changes can provide additional information and fill acquisition gaps [29, 30].
In light of these considerations, we propose to invert decentralized DSA time-lapse data with the so-called *Simultaneous Joint Migration Inversion* [SJMI, 12, 30], which combines JMI with simultaneous time-lapse data processing by inverting baseline and monitor datasets contemporaneously.
Considering a total of N_{tl} time-lapse surveys, the revised SJMI objective function can be formulated as follows:

$$J = \sum_{j=1}^{N_{tl}} \left[J_{\Delta_j} + J_{f_j} \right], \tag{4.43}$$

where the term J_{Δ_j} is the misfit norm function relative to the j^{th} time-lapse survey, computed as formulated in Equation 4.16. The term J_{f_j} is the constraining functional computed for the j^{th} time-lapse survey. Namely, the following four constraints are included in the inversion scheme [31]:

$$\begin{aligned} J_{f_j} \quad = \quad & \lambda_{1,j} \left[||\Lambda_R \left(\mathbf{R}_j^{\cup} - \mathbf{R}_b^{\cup} \right)||_2^2 + ||\Lambda_R \left(\mathbf{R}_j^{\cap} - \mathbf{R}_b^{\cap} \right)||_2^2 \right] \quad + \\ + \quad & \lambda_{2,j} ||\Lambda_{S_c} \left(\mathbf{S}_{c,j} - \mathbf{S}_{c,b} \right)||_2^2 \quad + \\ + \quad & \lambda_{3,j} \left[||\mathbf{C}^{-1} \mathbf{R}_j^{\cup}||_1 + ||\mathbf{C}^{-1} \mathbf{R}_j^{\cap}||_1 \right] \quad + \\ + \quad & \lambda_{4,j} \left[||\nabla_{\parallel} \mathbf{S}_{c,j}^{-1}||_1 + ||\nabla_{\perp} \mathbf{S}_{c,j}^{-1}||_1 \right]. \end{aligned} \tag{4.44}$$

The first two terms represent L2-norm constraints on the difference between the inverted reflectivity and slowness models resulting from the j^{th} time-lapse survey dataset ($\mathbf{R}_j^{\cup}, \mathbf{R}_j^{\cap}, \mathbf{S}_{c,j}$) and the ones resulting from the time-lapse survey dataset with the best subsurface illumination ($\mathbf{R}_b^{\cup}, \mathbf{R}_b^{\cap}, \mathbf{S}_{c,b}$; note that the dataset with the best subsurface illumination may not be the baseline dataset). Here, with $\mathbf{R}$ we refer to the full reflectivity model, being the collection of all $\mathbf{R}(z_n)$. Via the operators Λ_R and Λ_{S_c} we impose spatial weightings on the inversion to prioritize updates on the areas expected to be affected by production. We assume that, outside these regions, reflectivity and slowness models remain largely unaltered. The values $\lambda_{1,j}$ and $\lambda_{2,j}$ are suitably chosen scaling factors.
The third term describes a L1-norm sparsity constraint on the reflectivity model, where $\mathbf{C}^{-1}$ is some user-defined sparsity-promoting transform and $\lambda_{3,j}$ is a suitably chosen scaling factor.
The fourth and last constraint refers to an L1-norm-based directional total variation regularization on the velocity model. Recently, similar non-quadratic L1-norm-based regularizations proved to be beneficial for improving the accuracy of velocity inversion by recovering smooth velocity profiles while preserving sharp layer edges and discontinu-

ities [12, 32]. However, these techniques generally rely on the horizontal and vertical gradient operators (∇_h and ∇_v), regardless of the local dip direction of the geological units. This method may thus become inadequate for complex and tilted geological profiles. It is proposed to redesign the regularization operators based on the local dip field obtained from the seismic images. For this purpose, we utilize the operators $\nabla_\parallel$ and $\nabla_\perp$, being the appropriately rotated and scaled version of ∇_h and ∇_v. The first, $\nabla_\parallel$, will be oriented along the local dip direction, the latter, $\nabla_\perp$, perpendicularly to it [33]. The value $\lambda_{4,j}$ is a suitably chosen scaling factor.

4.3. NUMERICAL EXAMPLES

4.3.1. FULL WAVEFORM MIGRATION OF DECENTRALIZED DISPERSED SOURCE ARRAYS DATA

In this section we demonstrate the feasibility of the decentralized DSA acquisition method with a 3D numerical example of marine seismic data migration. By using the aforementioned Full Wavefield Modeling algorithm, the data is simulated with a real-time path coordination approach based on the artificial potential field concept introduced above. We will compare this result with the one obtained from a centralized DSA dataset acquired on the same model, but on a regular shot grid. The inversion is performed utilizing the Full Wavefield Migration algorithm [11, 25], also introduced above.
The numerical example is based on the 3D SEG EAGE salt model [34]. The velocity profile used as reference is shown in Figure 4.5a. Note that the three sections of the velocity model shown in Figure 4.5a portray three orthogonal slices from inside the model. The horizontal slice (top-left) is located at $z = 750$ m. The slice on the bottom-right is located at $x = 1000$ m and the slice on the bottom-left corner is located at $y = 1000$ m. The model is 2000 m wide along both horizontal directions and 1000 m deep. The grid size of the model is 10 m in both horizontal directions and 5 m in the vertical direction.

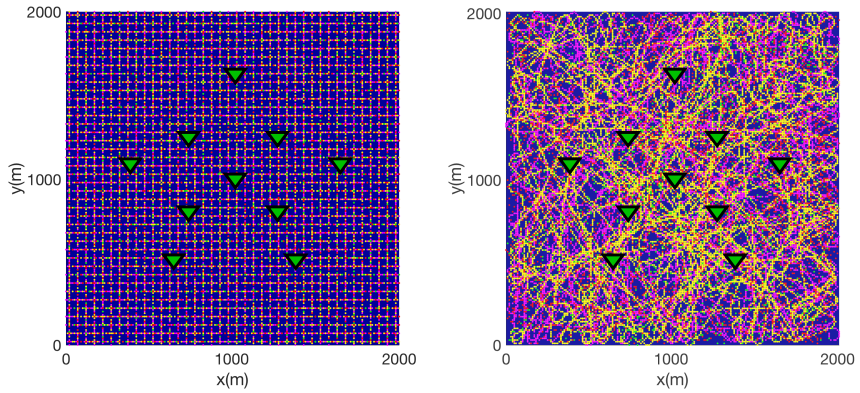

Figure 4.4: *Centralized (a) and decentralized (b) acquisition geometries. The green triangles represent the floating receiver nodes while the colored dots represent shot locations. Different colors refer to different DSA types of source.*

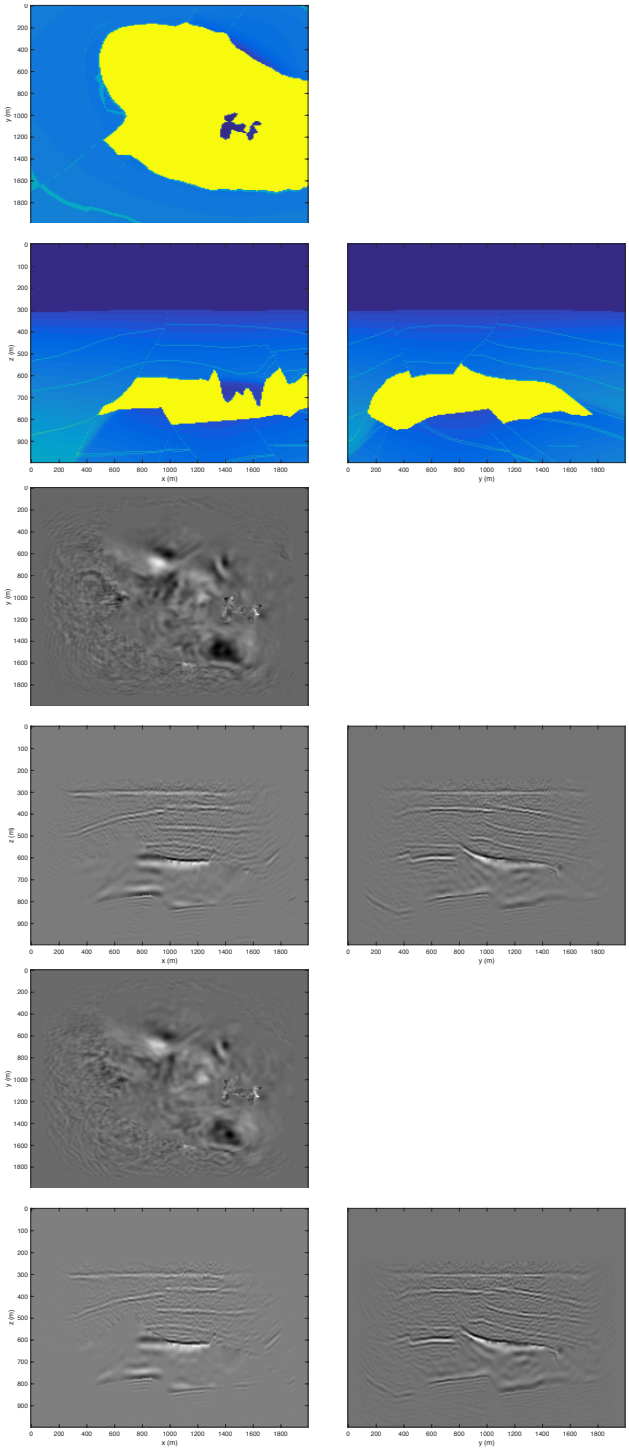

Figure 4.5: *Velocity profile used as reference for the 3D Full Wavefield Migration inversion (a) and inversion results for the centralized (b) and decentralized (c) DSA acquisition geometries.*

Four different DSA units are considered: ultralow- (2-6 Hz), low- (5-15 Hz), mid- (10-30 Hz) and high-frequency sources (20-60 Hz). For both simulations, 8 source boats per type are deployed simultaneously except for the ultralow-frequency sources, where 4 boats were deployed instead. The shot interval is irregular in order to distribute the blending noise more evenly (between 10 m and 20 m for the high-frequency units, between 20 m and 30 m for the mid-frequency units, between 30 m and 70 m for the low-frequency units and between 50 m and 100 m for the ultralow-frequency units). The same survey duration and number of shots per source type are considered for both experiments.
For the centralized case (Figure 4.4a), the source boats sail along straight lines parallel to both horizontal axis. The crossline spacing between lines is constant and equal to 100 m for the ultralow-frequency sources, 50 m for all other sources. For the decentralized case (Figure 4.4b), the sources are left free to sail within an artificial potential field generated as described in the previous section. No offline path-planning is computed beforehand and the devices are only expected to autonomously avoid each other and stay within the target area boundaries.
On the receiver side, a total of 10 floating nodes has been chosen. One is placed at the center of the area of interest while the others are evenly spaced around it along two concentric circumferences of 300 m (4 nodes) and 650 m (5 nodes) radius , respectively. Each node is positioned at a depth of 200 m below the water surface, 50 m above the ocean bottom. The receivers are recording continuously for the entire survey duration, and the result of this blended experiment is one single *supertrace* per node. For this small scale example, the length of the supertrace is approximately 30 minutes. The data inversion is performed without deblending (i.e., the inversion uses the 10 supertraces). All internal and surface multiples were utilized and not removed in the inversion process.
The FWM results are presented in Figure 4.5b-c. The same slices as for the velocity model are portrayed. With these acquisition settings, we do not expect to properly image the larger offsets, but we can see that, at the final iteration, the crosstalk and the blending noise are largely suppressed in both cases and the inversion results are comparable. This example demonstrates that it is not strictly necessary to acquire data on a regular grid in order to obtain good inversion results.

4.3.2. SIMULTANEOUS JOINT MIGRATION INVERSION OF DECENTRALIZED DISPERSED SOURCE ARRAYS DATA

In this section we demonstrate the feasibility of the decentralized DSA acquisition method with 2D numerical examples of time-lapse seismic data migration. As discussed in the previous sections, decentralized DSA surveys are non-repeatable by nature. It is thus crucial to find a robust and reliable strategy to properly handle time-lapse data. To that end, we chose to perform the inversion with the above-mentioned *Simultaneous Joint Migration Inversion* algorithm [SJMI, 12, 30].
The numerical example is based on a modified version of the well-known Marmousi model [35]. The profile under consideration is 4000 m wide along the horizontal direction and 1100 m deep. The velocity and reflectivity models used as reference are shown in Figure 4.6, together with the time-lapse differences. Concerning the time-lapse

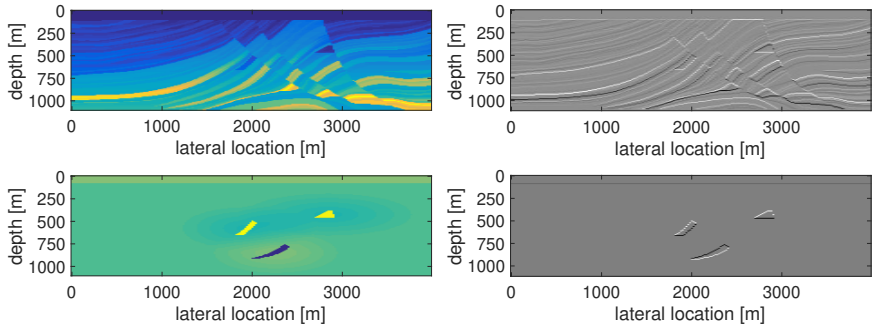

Figure 4.6: *Velocity (top left) and reflectivity (top right) models used as reference for Simultaneous Joint Migration Inversion. Time lapse perturbations are highlighted in the bottom row, both for velocity (left) and reflectivity (right).*

changes, two gas-sand traps and one oil sand trap were embedded in the model. Respectively, water-gas replacements modify the reservoir velocity causing an increase of 150 *m/s* while, for the oil sand trap, injection reduces the reservoir velocity by 200 *m/s*. Additionally, pressure perturbations and velocity variations caused by temperature fluctuations within the water column are also considered. Internal multiple and ghost signals are not removed from the data, see [36] and [3] for a more detailed discussion on how to include them in the modeling and inversion procedure.

The inversion results of three distinct time-lapse acquisition scenarios are compared hereafter. In each case, three different source types are utilized: ultralow- (2-8 *Hz*), low- (5-20 *Hz*) and mid-frequency sources (10-40 *Hz*). In the first time-lapse acquisition scenario, repeated regular baseline and monitor survey geometries were considered. The source sampling for ultralow-, low- and mid- frequency sources is regular and equal to 100 *m*, 40 *m* and 20 *m*, respectively. In the second and third acquisition scenarios, the acquisition geometries are non-repeated. In one case, a regular baseline survey is followed by a decentralized monitor survey. In the other case, both baseline and monitor survey geometries are decentralized (non-repeated). For the decentralized surveys, the same number of shots per source type as for the regular surveys is considered. In this case, the shot points are randomly distributed along the surface to simulate a fully decentralized acquisition. On the receiver side, the channel density and locations were not modified. The receiver interval is regular and equal to 20 *m*. The inverted time-lapse image and velocity for each acquisition scenario are presented in Figure 4.7 in the order they were mentioned above. It is shown that SJMI can provide most time-lapse information in each case, while no substantial degradation in the overall quality of the results is introduced by the survey geometry mismatch in the decentralized acquisition scenarios.

From a practical perspective, most seismic surveys to date have been conducted by deploying conventional sources instead of DSA devices. Realistically, legacy baseline and DSA monitor surveys would thus drastically differ not only in terms of acquisition geometry but even in what concerns the type of sources utilized and the frequency content of the data. We can show that, also in these situations, SJMI is an effective tool for time-

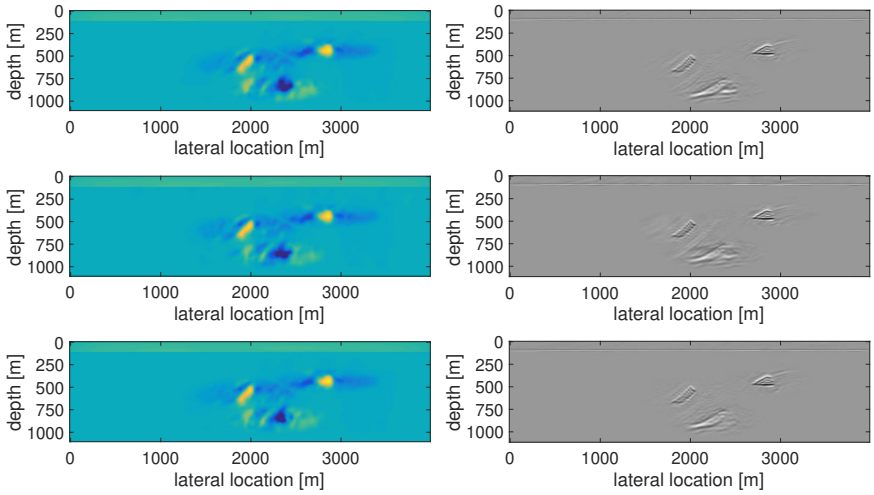

Figure 4.7: *Simultaneous Joint Migration Inversion results from three distinct DSA time-lapse acquisition scenarios. In the first (top row), repeated regular baseline and monitor survey geometries were considered. In the second and third acquisition scenarios, the acquisition geometries are non-repeated (centre: regular baseline geometry, decentralized monitor; bottom: decentralized baseline and monitor geometries).*

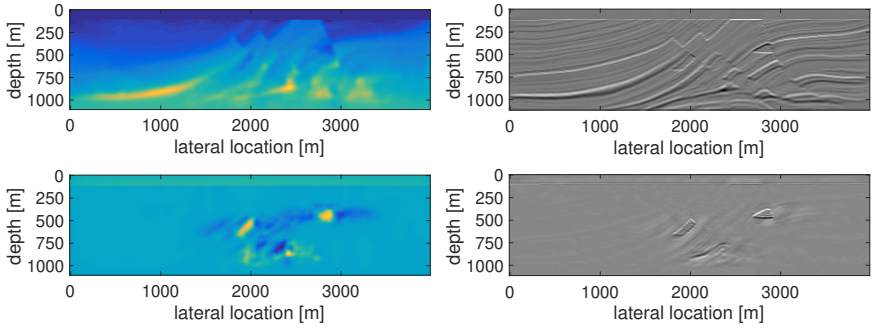

Figure 4.8: *Inverted time-lapse image and velocity models with broadband data baseline geometry and decentralized DSA monitor geometry. Velocity (left) and reflectivity (right) models are shown in the top row, time lapse perturbations are highlighted in the bottom row.*

lapse imaging and reservoir monitoring. In the following, the inversion results of an additional time-lapse acquisition scenario on the same model as the above are presented. In this case, a baseline survey conducted by deploying conventional sources on a regular grid is considered. The bandwidth of the baseline dataset is considered to span a range of frequencies between 4 Hz and 40 Hz. The source sampling is equal to 20 m. For the monitor acquisition, the survey geometry is non-repeated and, instead of conventional sources, the DSA devices introduced above are utilized in a decentralized manner. For the mid-frequency sources, the same number of shots as for the regular legacy baseline surveys is randomly distributed along the surface to simulate a fully decentralized acquisition. The number of randomly located shots is decimated by a factor 2 and 5 for

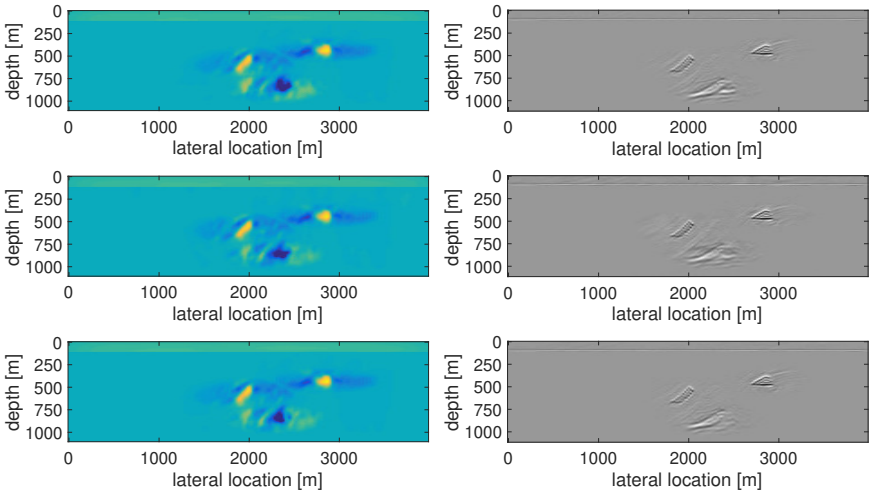

Figure 4.9: *SJMI results from the same DSA time-lapse acquisition scenarios as for Figure 4.7. Before inversion, random background noise was added to the dataset (Noise level: 40 %) In top row example, repeated regular baseline and monitor survey geometries were considered. For the second and third acquisition scenarios, the acquisition geometries are non-repeated (centre: regular baseline geometry, decentralized monitor; bottom: decentralized baseline and monitor geometries).*

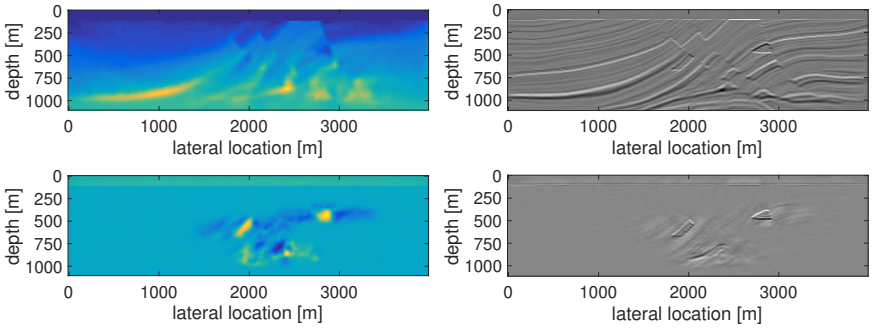

Figure 4.10: *Inverted time-lapse image and velocity models with broadband data baseline geometry and decentralized DSA monitor geometry. Velocity (left) and reflectivity (right) models are shown in the top row, time lapse perturbations are highlighted in the bottom row. Except for a noise level of 40 %, the example is identical to the one presented in Figure 4.8.*

the low- and ultralow-frequency sources, respectively. On the receiver side, the channel density and locations were not modified. The receiver interval is regular and equal to 20 *m*. The inverted time-lapse image and velocity models are presented in Figure 4.8. Once more it is shown that, by choosing the appropriate imaging tool, the overall quality of the results is comparably satisfactory, despite the substantial survey geometry mismatch, even when the type of sources utilized and their frequency bands vary significantly.
In order to test the robustness of SJMI in the presence of noise, background noise with random amplitude and phase was added to the dataset and the two examples presented

in this subsection were thus repeated. The strength of the noise was adjusted by altering the noise level, which can be defined as the energy ratio between the background random noise and the overall signal:

$$Noise\,Level = \frac{\sum_{shots}\sum_{traces} n^2}{\sum_{shots}\sum_{traces} d^2} \cdot 100\%. \tag{4.45}$$

For the examples presented in Figures 4.9 and 4.10, a noise level corresponding to 40 % has been considered. It can be seen that SJMI is very robust to random noise and that the deterioration of the quality of the inversion result is very limited. Its robustness to random noise can be attributed both to the inversion scheme of JMI and the simultaneous strategy of SJMI. A strategy to deal with coherent harmonic distortion is instead introduced in subsection 5.2.2 of this thesis.

4.4. CONCLUDING REMARKS

The so-called Dispersed Source Array (DSA) acquisition method has received growing attention in the last years and large-scale industrial applications are beginning to turn into a reality. Together with the concept of blending, it has become an increasingly relevant topic due to its critical importance for efficient and more affordable high-resolution seismic imaging.

A major practical advantage of the DSA concept is that most of its source units are expected to be smaller and less powerful than conventional sources providing the acquisition system with increased operational flexibility. To handle the larger number of sources that are simultaneously operational in the field, we propose to organize the acquisition system in an automated and decentralized manner. By applying this strategy, it is possible to produce valid inversion results even without offline path planning (acquisition geometry design). As an intermediate step, a hybrid approach, which involves real-time automated path adaptations of a simple predetermined plan with the aid of live positional data, is expected to produce satisfactory result. Finally, using the SJMI (or a similar) technology it is possible to reliably recover time-lapse information even with a significant mismatch between baseline and monitor survey geometries (e.g. decentralized DSA).

REFERENCES

[1] A. J. Berkhout, *Blended acquisition with dispersed source arrays,* Geophysics **77**, A19 (2012).

[2] C. Tsingas, Y. S. Kim, and J. Yoo, *Broadband acquisition, deblending, and imaging employing dispersed source arrays,* The Leading Edge **35**, 354 (2016).

[3] M. Caporal, G. Blacquière, and M. Davydenko, *Broadband imaging via direct inversion of blended dispersed source array data,* Geophysical Prospecting **66**, 942 (2018).

[4] F. ten Kroode, S. Bergler, C. Corsten, J. W. de Maag, F. Strijbos, and H. Tijhof, *Broadband seismic data - the importance of low frequencies,* Geophysics **78**, WA3 (2013).

[5] D. Davis and E. Patronis, *Sound system engineering* (Focal Press, 2006).

[6] R. M. Laws, E. Kragh, and G. Morgan, *Are seismic sources too loud?* EAGE (Eur. Ass. of Geosc. and Eng., Expanded abstracts, Rome, 2008).

[7] E. Kragh, R. Laws, J. F. Hopperstad, and A. Kireev, *Reducing the size of the seismic source with a 4C towed-marine streamer,* EAGE (Eur. Ass. of Geosc. and Eng., Expanded abstracts, Copenhagen, 2012).

[8] D. K. Reust, O. A. Johnston, J. A. Giles, and S. Ballinger, *Very low frequency seismic source,* SEG (Soc. Expl. Geophys., Expanded abstracts, 2015).

[9] J. Dellinger, A. Ross, D. Meaux, A. Brenders, G. Gesoff, J. T. Etgen, J. Naranjo, G. Openshaw, and M. Harper, *Wolfspar, an fwi friendly ultra-low-frequency marine seismic source,* SEG (Soc. Expl. Geophys., Expanded abstracts, 2016).

[10] O. Khatib, *Real-time obstacle avoidance for manipulators and mobile robots,* International Journal of Robotics Research **5**, 90 (1986).

[11] M. Davydenko and D. J. Verschuur, *Full-wavefield migration: using surface and internal multiples in imaging,* Geophysical Prospecting **65**, 7 (2017).

[12] S. Qu and D. J. Verschuur, *Simultaneous time-lapse imaging via joint migration and inversion,* EAGE (Eur. Ass. of Geosc. and Eng., Expanded abstracts, Vienna, 2016).

[13] A. J. Berkhout, *Seismic migration, imaging of acoustic energy by wave field extrapolation, A: theoretical aspects* (Elsevier, 1982).

[14] C. P. A. Wapenaar and A. J. Berkhout, *Elastic wave field extrapolation: redatuming of single- and multi-component seismic data* (Elsevier Science Publ. Co., Inc., 1989).

[15] D. Gisolf and D. J. Verschuur, *The Principles of Quantitative Acoustical Imaging* (EAGE Publications BV, 2010).

[16] A. J. Berkhout, *Changing the mindset in seismic acquisition,* The Leading Edge **27**, 924 (2008).

[17] A. J. Berkhout, *Review paper: An outlook on the future seismic imaging, part I: forward and reverse modelling,* Geophysical Prospecting **62**, 911 (2014).

[18] H. Bremmer, *The W.K.B approximation as the first term of a geometric-optical series,* Commun. Pure Appl. Math. **4**, 105 (1951).

[19] J. Corones, *Bremmer series that correct parabolic approximations,* Journal of Mathematical analysis and applications **50**, 361 (1975).

[20] M. V. de Hoop, *Generalization of the Bremmer coupling series,* Journal of Mathematical Physics **37**, 3246 (1996).

[21] C. P. A. Wapenaar, *One-way representations of seismic data,* Geophys. J. Int **127**, 178 (1996).

[22] A. J. Berkhout, *Review paper: An outlook on the future seismic imaging, part III: Joint Migration Inversion,* Geophysical Prospecting **62**, 950 (2014).

[23] Y. Tang and B. Biondi, *Least-squares migration/inversion of blended data,* SEG (Soc. Expl. Geophys., Expanded abstracts, Houston, 2009) pp. 2859–2863.

[24] W. Dai, X. Wang, and G. T. Schuster, *Least-squares migration of multisource data with a deblurring filter,* Geophysics **76**, R135 (2011).

[25] A. J. Berkhout, *Review paper: An outlook on the future seismic imaging, part II: Full-wavefield migration,* Geophysical Prospecting **62**, 931 (2014).

[26] D. E. Lumley, R. A. Behrens, and Z. Wang, *Assessing the technical risk of a 4-d seismic project,* The Leading Edge **16**, 1287 (1997).

[27] D. J. Verschuur, X. R. Staal, and A. J. Berkhout, *Using primaries and multiples in time-lapse imaging and velocity estimation,* SEG (Soc. Expl. Geophys., Expanded abstracts, 2014).

[28] S. Lu, D. Whitmore, A. Valenciano, and N. Chemingui, *Separated-wavefield imaging using primary and multiple energy,* The Leading Edge **34**, 770 (2015).

[29] H. Wason, F. Oghenekohwo, and F. J. Herrmann, *Randomization and repeatability in time-lapse marine acquisition,* SEG (Soc. Expl. Geophys., Expanded abstracts, 2014).

[30] S. Qu and D. J. Verschuur, *Simultaneous joint migration inversion for semicontinuous time-lapse seismic data,* SEG (Soc. Expl. Geophys., Expanded abstracts, 2017).

[31] S. Qu and D. J. Verschuur, *Time-lapse simultaneous joint-migration inversion for high-resolution imaging/inversion based on a realistic synthetic model from the grane field,* SEG (Soc. Expl. Geophys., Expanded abstracts, 2018).

[32] A. Anagaw and M. Sacchi, *Edge-preserving seismic imaging using the total variation method,* Journal of Geophysics and Engineering **9** (2012).

[33] S. Qu and D. J. Verschuur, *Full waveform inversion and joint migration inversion with an automatic directional total variation constraint,* Geophysics **82**, R175 (2019).

[34] F. Aminzadeh, J. M. Burkhard, L. Nicoletis, F. Rocca, and K. Wyatt, *Seg/eage 3-D modeling project: 2^{nd} update,* The Leading Edge **13**, 949 (1994).

[35] R. Versteeg and G. Grau, *The marmousi experience,* EAGE (Eur. Ass. of Geosc. and Eng., Expanded abstracts, 1991).

[36] M. Caporal and G. Blacquière, *Seismic acquisition with dispersed source arrays - imaging including internal multiples and source ghost reflections,* EAGE (Eur. Ass. of Geosc. and Eng., Expanded abstracts, Vienna, 2016).

5

CONCLUSIONS AND ROAD AHEAD

5.1. CONCLUSIONS

The prime focus for this thesis is on seismic acquisition and survey design. Two different methodologies to improve the efficiency of the operations and the quality of the seismic data are, at first, independently introduced and, later, jointly implemented in order to achieve the best possible outcome.
On one hand, with the concept of Dispersed Source Array, we aim at broadening the frequency spectrum of the seismic data to match the industry's ever increasing demands. It is proposed to utilize multiple types of sources during seismic surveys, each one dedicated to the transmission of a different frequency band, within the temporal bandwidth of interest. The main conclusions on this topic can be summarized as follows:

- Provided that the signal-to-noise ratio is adequate, fold and source strength can be chosen in a frequency dependent manner. Low frequency sources can be distributed more sparsely (and, if necessary, on larger offsets) than high frequency sources;

- The manufacture of each individual source becomes technically simpler and a more effective energy transmission is guaranteed. Unlike broadband sources, DSA units do not need to optimally perform at all frequencies;

- For the higher frequencies, sources become smaller and operationally more flexible, resulting in an increased survey productivity;

- In marine surveys, the destructive interference due to the source ghost notches can be mitigated by towing the devices at their specific optimum depth. This means that each source must be positioned below the water surface, at a depth z_s equal to a quarter of its central frequency wavelength λ_c, or at any half wavelength starting from that value (*i.e.*: $z_s = \frac{(2n+1)\lambda_c}{4}$, with $n \in \mathbf{Z}$);

- The enhanced flexibility and control on the seismic energy emission per frequency range introduced with the DSA concept represents a worthwhile added value. The simultaneous use of different sources with diversified spectral properties can appreciably help improving the signal-to-noise ratio. The frequency spectrum of the ambient noise is, in fact, hardly flat in the frequency domain;

- Using DSA devices, it is possible to reduce the amount of energy produced at frequency ranges that are of no benefit to seismic imaging (> 100 Hz) but may be harmful to the environment, particularly offshore. This is especially interesting considering the strict environmental regulations that are currently enforced worldwide.

On the other hand, we propose two algorithm solutions that are able to cope with adverse terrain conditions, such as obstacles in the field and inaccessible areas. The two methods are based on the reorganization of regular (centralized) and irregular (decentralized) source acquisition grids, respectively. Below, the main features of the two techniques are highlighted:

- During operations, ad hoc adjustments to the nominal survey geometry are often necessary and are conventionally performed manually. The proposed solutions can perform this task automatically;

- Geological and ecological prior information about the region of interest, as well as instructions regarding ideal illumination goals, can be easily integrated;

- In the decentralized case, the source units are not necessarily provided with a detailed acquisition preplan ahead of the survey. However, they can modify their moving speed and direction in order to adapt their path to the field conditions (e.g. obstacles, restricted areas, etc.). While doing so they are expected to deliver a well sampled dataset, in terms of offset, azimuth and fold distributions.

- The actual number of sources contemporaneously operational in the field does not sensibly affect the performance of the algorithm;

- In light of the encouraging results, it is worth considering a decentralized approach also when designing surveys for obstacle-free terrains.

Finally, we show how Disperse Source Arrays and decentralized automated path planning can be mutually beneficial. In particular:

- On one hand, by introducing the DSA concept, we expect to deal mostly with smaller and less powerful sources than in conventional surveys. This feature provides the acquisition system with increased operational flexibility;

- On the other hand, by means of an automated decentralized approach to survey design, we are able to handle the larger number of sources that are simultaneously operational in the field without a substantial additional effort;

- Despite the significant mismatch between baseline and monitor survey geometries introduced by the decentralized acquisition method, we show that it is possible to reliably recover time-lapse information. This consideration still holds even when, for the monitor survey, different types of sources than for the baseline survey are utilized (DSA versus broadband sources).

5.2. RECOMMENDATIONS FOR FURTHER RESEARCH

In this section, suggestions for future work on the topics of Dispersed Source Array acquisition and automated path planning for seismic survey design are proposed. These ideas still require more extensive research but few preliminary results and examples are presented. A special acknowledgement goes to Constantinos Tsingas and Abdulrahman AlShuhail (both from Saudi Aramco) as well as to Xander Campman (from Shell) for their encouragement in pursuing these concepts.

5.2.1. SURVEY DESIGN: GLOBAL PARAMETERS OPTIMIZATION

In large-scale 3D seismic data acquisitions, the survey design can become quite challenging. Many different survey parameters need to be appropriately tuned in order to cope with a wide variety of geophysical, operational and economical constraints. Oftentimes, some sort of compromise needs to be accepted in exchange for a reasonable balance between the numerous requirements. However, the nature and the consequences of this trade-off between costs and data quality are non trivial. Essentially, each seismic survey has very specific characteristics. Thus, it is impractical to find an analytical or numerical technique able to select the best set of parameters under any circumstance. However, it might be convenient to look at this sort of problems from a different perspective. An interesting and unconventional approach was presented by [1, 2] and [3]. The two works encourage acquisition geophysicists to look at 3D seismic survey design as a complex optimization problem. Despite their implementations and the choice of the inversion methods are marginally different, they both illustrate how mathematical programming can be a valuable tool to solve problems in survey design.
The method introduced by [1, 2] aims at selecting the appropriate survey design parameters based on the minimization of a cost function, which is a weighted sum of the square of their deviations from a user-defined list of desirable target values. The cost function is minimized first using the built-in FindMinimum function available in Mathematica (Wolfram) and an especially designed program written in C, in a second stage. The method introduced by [3] aims at minimizing the actual cost (price) of the 3D survey, while satisfying a set of geophysical and operational constraints. The cost function is minimized using the built-in Solver function available in Microsoft Excel.
From a mathematical point of view, the two methods are not substantially different. The main difference consists in how the cost function is computed, but the actual parameters and constraints are nearly the same. Even in terms of optimization method, their nature is very similar. They both rely on local (gradient-based) inversion schemes, which strongly depend on adequate initial values to generate satisfactory results. As demonstrated in the same publications, the mathematical program is non linear and tends to converge to a local optimal value in the vicinity of the initial solution. Obviously, the final solution is not necessarily the global minimum (nor an acceptable local minimum) of the highly multimodal cost function. For this reason, in order to improve the performance of the procedure and to increase the chances of convergence to an adequate solution, it is proposed to minimize the cost function using a global optimization approach, namely a Genetic Algorithm [4]. A practical example is proposed below. For a

fair comparison, the objective function and the list of the desirable target parameters are defined as in [2].

EXAMPLE

The following example is based on the one presented by [2]. It is assumed that the data will be acquired using the shot-centered, one-line roll template technique [5]. The template is described by two orthogonal coordinates (x, y) and the following six design parameters:

Notation	Description
s_x	shot interval (x direction).
s_y	shot interval (y direction).
r_x	receiver interval (x direction).
r_y	receiver interval (y direction).
n_x	number of receivers (x direction).
n_y	number of receivers (y direction).

Note that, as in [2], hereafter the use of generic x and y is preferred over the use of the terms *inline* and *crossline*. Based on the aforementioned six parameters, all key survey specifications can be uniquely defined:

Notation	Description	Definition
b_x	bin size (x direction).	$\frac{min(s_x,r_x)}{2}$
b_y	bin size (y direction).	$\frac{min(s_y,r_y)}{2}$
f_x	2D CMP fold (x direction).	$\frac{n_x r_x}{2 s_x}$
f_y	2D CMP fold (y direction).	$\frac{n_y}{2}$
f_{3D}	3D CMP fold.	$f_x f_y$
n	total live receivers.	$n_x n_y$
t_x	template dimension (x direction).	$(n_x - 1) r_x$
t_y	template dimension (y direction).	$(n_y - 1) r_y$
x_{max}	maximum offset (y direction).	$\frac{\sqrt{t_x^2 + t_y^2}}{2}$

To test this idea, the following objective function was defined:

$$f_{obj} = w_1 \left(\frac{t_x - t_y}{t_x + t_y}\right)^2 + w_2 \left(\frac{x_{max} - X_{max}}{x_{max}}\right)^2 + w_3 \left(\frac{b_x - B_x}{b_x}\right)^2 + w_4 \left(\frac{b_y - B_y}{b_y}\right)^2 + w_5 \left(\frac{f_{3D} - F_{3D}}{f_{3D}}\right)^2 + w_6 \left(\frac{n - N}{n}\right)^2, \tag{5.1}$$

where w_i are appropriately selected weighting functionals and capital letters are used to depict the user-defined target survey parameters. The purpose of the first terms is to guarantee that the template is as *square* as possible, in order to obtain a uniform azimuth distribution. The following five terms aim at obtaining a set of acquisition parameters as close as possible to the user-defined target values. Note that each term is appropriately normalized.

In [2], the final results are unsatisfactory and the authors finally opt for inverting for the

first two terms alone. Namely:

$$f_{obj} = w_1 \left(\frac{t_x - t_y}{t_x + t_y} \right)^2 + w_2 \left(\frac{x_{max} - X_{max}}{x_{max}} \right)^2. \quad (5.2)$$

Nevertheless, by choosing a global optimization method (specifically a Genetic Algorithm) and appropriate constraints for the parameters, we were actually able to obtain more reasonable values for the entire set of variables of Equation 5.1 (see below). Note that more research is necessary to further stabilize the inversion and turn the algorithm into a practical software for operations. However, we see great potential in this technique and encourage future investigations.

Input parameters	
N	500
B_x	25 m
B_y	12.5 m
F_{3D}	24
X_{max}	2000 m

Output parameters			
s_x	200 m	n	492
s_y	25 m	b_x	25 m
r_x	50 m	b_y	12.5 m
r_y	200 m	x_{max}	1485 m
t_x	2000 m	f_{3D}	31
t_y	2200 m		

5

5.2.2. SOURCE-GENERATED DISTORTIONS: SIGNAL OR NOISE?

In vibroseis operations, source-generated harmonic distortions are a frequently-observed characteristic phenomenon [6]. Poor coupling between the baseplate and the ground [7], as well as nonlinearities associated with the mechanical and hydraulic properties of the vibrator [8], are considered the major causes of these interferences. Typically, this kind of distortions are regarded as noise but, unlike other types of noise, they are not uncorrelated with the fundamental sweep. In fact, the harmonic signal closely resembles the fundamental signal in shape, but its frequency range limits are positive integer multiples of the ones associated with the fundamental signal (see Figure 5.1). As a consequence, the crosscorrelation process may produce undesired artifacts, namely an oscillatory tail on the correlogram for *downsweeps* (sweeps with frequency decreasing with time) or an oscillatory forerunner on the correlogram for *upsweeps* (sweeps with frequency increasing with time). [8] also documented the observation of *subharmonics* in uncorrelated vibroseis data. In this case, the frequency range limits of the harmonic signal are positive integer ratios of the ones associated with the fundamental signal, rather then multiples. To distinguish them from the subharmonics, other harmonics are referred to as *higher harmonics*.

Since the 1970's, a lot of research has been conducted on the attenuation and removal of the harmonic signal. To the contrary, limited attention has been paid to the development of practical techniques aimed at the separation (and eventually the utilization) of the harmonics [9–12].

Considering that, in principle, harmonic signal can be predictable, we believe that further research in the topic could provide new valuable insights, especially for near surface characterization. As a matter of fact, by making use of the harmonic signal instead of re-

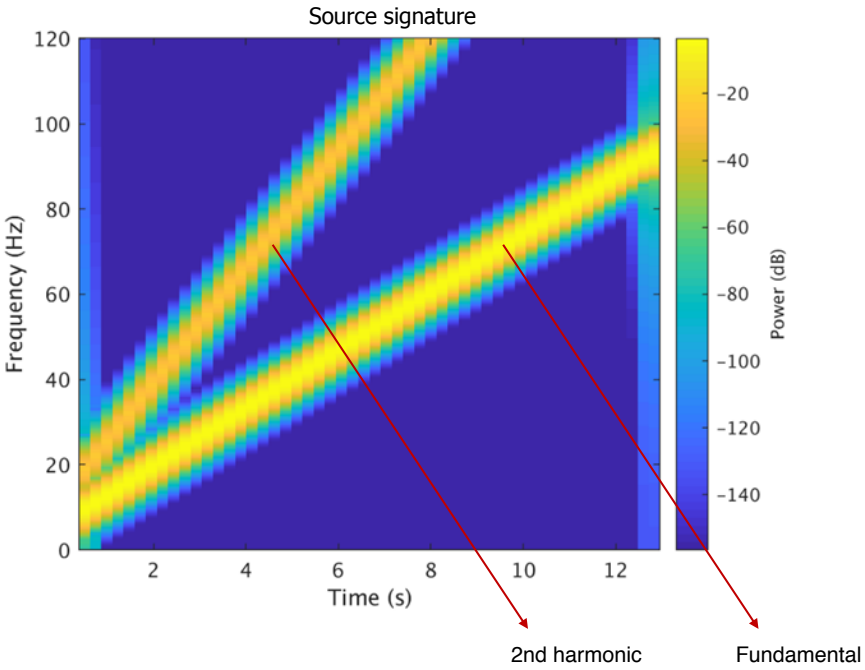

Figure 5.1: *Time-frequency map of a linear sweep fundamental and second harmonic.*

moving it, the frequency band of the data can be broadened. In practice, the harmonics act as natural DSA sources. Below, a simple demonstration of this concept is presented.

EXAMPLE

To illustrate the idea, we numerically generated a 2D shot record based on a flat layered velocity model (Figure 5.2a). The density profile was considered to be homogeneous. As seismic source, the combination of a conventional linear sweep from 6 Hz to 96 Hz and its first higher harmonic, from 12 Hz to 192 Hz, was chosen (Figure 5.2b). The correspondent modeled data is shown both in the t-x domain (Figure 5.2c) and f-t domain (Figure 5.2d). In Figure 5.3, we present the modeled data correlated with: the nominal sweep (Figure 5.3a), the harmonic signal (Figure 5.3b) and the combination of the two (Figure 5.3c). By looking at it in the f-t domain (Figure 5.4), we can see how an all new range of frequencies between 96 Hz and 192 Hz is included (in the red circles, Figure 5.4b and 5.4c), if we compare the result with the fundamental sweep signal alone (Figure 5.4a).
This is particularly interesting if we consider DSA sources. If the harmonics-to-noise ratio is acceptable, mid- and low- frequency sources can enhance the quality of the data in the higher frequencies as well. Furthermore, the same type of approach may improve the harmonic signal removal, in case it was more convenient to consider it as correlated noise. Clearly more research is required, especially to be able to recover the correct harmonics amplitude. However, we see great potential in this concept and encourage future investigations.

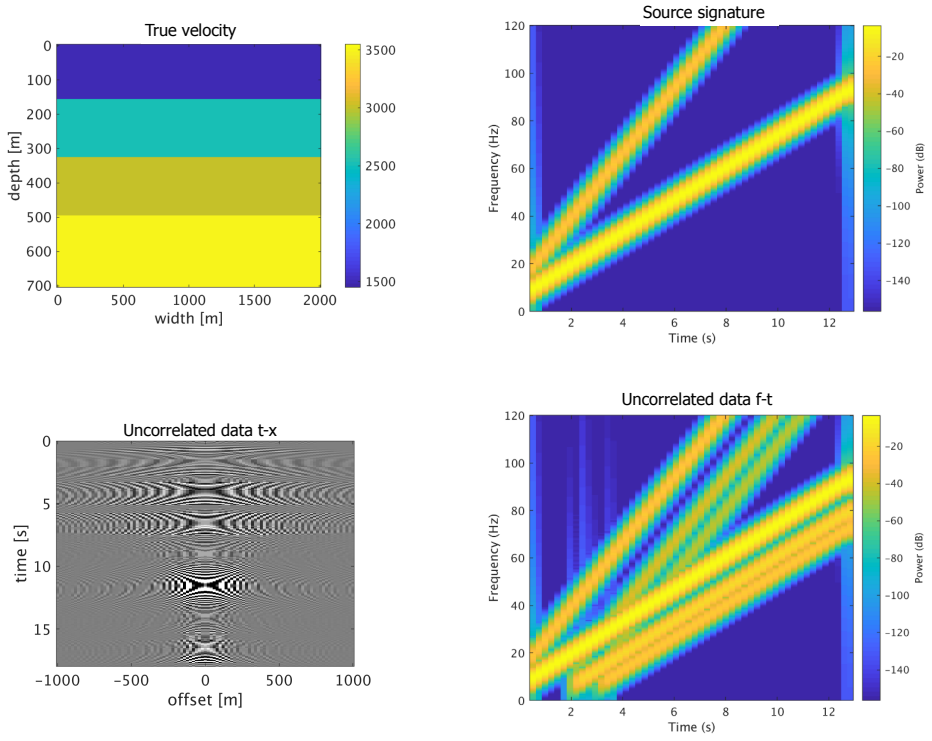

Figure 5.2: *Shot record of a linear sweep fundamental and second harmonic: velocity model (a); t-f map of the source signature (b); t-x map of the uncorrelated shot record (c); t-f map of the uncorrelated shot record (d).*

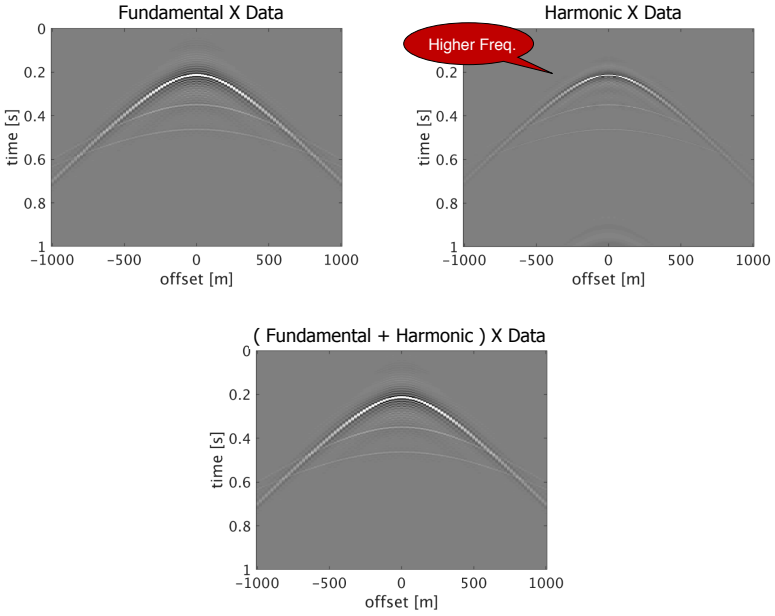

Figure 5.3: *t-x map of the shot record correlated with: the pilot sweep (a); its second harmonic (b); the sum of the pilot sweep and its second harmonic (d).*

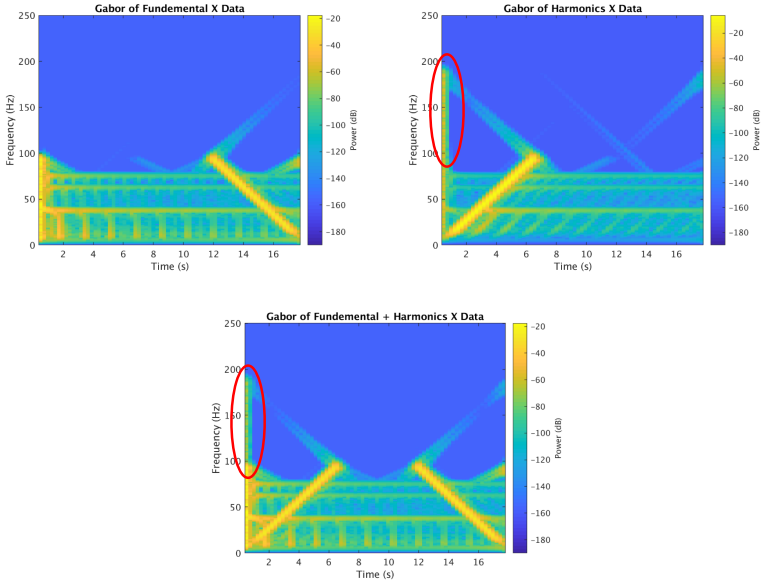

Figure 5.4: *t-f map of the shot record correlated with: the pilot sweep (a); its second harmonic (b); the sum of the pilot sweep and its second harmonic (c).*

5.2.3. AMBIENT NOISE: TOWARDS NOISE-ADAPTIVE SURVEYING

During seismic surveys, several adjustments can be implemented in order to scale down the destructive interference introduced by the seismic ambient noise and consequently improve the data quality. On the source side, for instance, more powerful, longer and/or repeated shots can drastically increase the signal-to-noise ratio of the recorded data. On the receiver side, instead, the same outcome can be achieved by selecting higher-sensitivity sensors, as well as by increasing the channel count and density. Nevertheless, both instrumental and cost-related limitations may reduce the flexibility of these survey design parameters and set hard operational constraints.

In this context, several innovative techniques and technologies were developed in order to cope with this critical issue. Although a significant number of different solutions have been proposed in the last decades, it is fair to imply that the seismic industry has seen a diffuse trend towards simultaneous shooting [i.e. *Blending* 13] and single-sensor recording [14] for high-productivity seismic surveying. On the one hand, by simultaneously recording seismic data generated by different active sources, it is possible to sensibly reduce the survey time (and, thus, the survey cost) as well as to mitigate the effects of the noise [15]. On the other hand, reducing the amount of sensors per channel can decrease the cost-per-channel both in terms of operational efforts and equipment expenditure. This becomes especially valuable today, when the demand for densely sampled, long offset and wide-azimuth data is on the rise.

Overall, a lot of attention is thus devoted to making seismic survey designs robust to all different kinds of ambient noise at once. However, due to the remarkable complexity of the problem, relatively limited quantitative research has been conducted on the specific spectral characteristics of such noise. Of course, there is general consensus within the seismic community on the lack of low frequencies signal, when compared to the high levels of ambient noise, but it could be of great value to gain more accurate and specific insights on its nature.

As pointed out by [16], in land seismic acquisition, ambient noise levels can fluctuate significantly both from one survey to another and during each single survey. Ambient noise records from several broadband point-receiver surveys around the world were analyzed. It was observed that, between the different surveys, the median RMS noise levels vary by a factor 10 over a range of frequencies spanning between 3 Hz and 100 Hz. Assuming that the noise is not source-generated, this is equivalent to a variation of a factor 100 in fold or sweep length and 10 in the number of vibrators per group. Analogously, substantial variation in the noise levels is recorded within each survey, both over time and over the frequency spectrum. An interesting case study was presented by [17]. The authors highlight the unevenness of the estimated power spectra of the noise within the frequency spectrum of seismic interest, at different depths in the image. They were able to isolate the ambient and the shot-generated noise from the signal. Surprisingly, the shot-generated noise exceeds the ambient noise by a considerable margin under most circumstances. The exception being at the lower frequencies (< 20 Hz), deep in the image in rough weather conditions. This means that airguns might be largely louder than necessary, at least above 20 Hz.

Both studies mentioned above suggest that, in most circumstances, emitting energy with a flat amplitude spectrum over the entire frequency band of interest is not necessarily

the most suitable choice. This is even more true if we consider that the response of the receivers is hardly flat in the frequency domain [18]. For these reasons, noise-adaptive acquisition design not only has the potential to increase the signal-to-noise ratio of the recorded data, but also to enhance the survey productivity by altering the requirements in terms, for instance, of fold and source strength. An example of noise-adaptive survey design was adopted by [19], who use the ambient noise spectral density for the pilot sweep design.

Some of the challenges in the study of the seismic ambient noise derive from the intrinsic nature of the noise itself. Unlike the seismic signal, the ambient noise is a power signal, not an energy signal and, therefore, requires a statistical approach and lengthier observations to quantitatively assess its spectral characteristics. In global seismology, the New Low and High Noise models (NLNM and NHNM) developed by [20] specify the range of noise levels detected on a global scale. An interesting step forward in ambient noise analysis applied to seismic surveying could be to update such models by adapting them to seismic prospecting. Considering the remarkable variability of the noise levels between different seismic surveys, it could be appropriate to develop regional/environment-specific models. For example, a set of models could be dedicated to desert environments or the Arabian peninsula, another to urban environments, and so on. Some valuable research in this direction has been presented by [21]. In the paper, the authors identify the main sources of ambient noise in an urban environment and study their individual characteristics and contributions. Based on the results of their studies, they provide qualitative practical guidelines to tailor the acquisition parameters to their specific survey scenario. This line of research is very promising and can have a considerable impact on the acquisition design.

REFERENCES

[1] C. L. Liner, R. Gobeli, and W. D. Underwood, *3-D seismic survey design as an optimization problem,* SEG (Soc. Expl. Geophys., Expanded abstracts, 1998).

[2] C. L. Liner, W. D. Underwood, and R. Gobeli, *3-D seismic survey design as an optimization problem,* The Leading Edge **18**, 1054 (1999).

[3] D. J. Morrice, A. S. Kenyon, and C. J. Beckett, *Optimizing operations in 3-D land seismic surveys,* Geophysics **66**, 1818 (2001).

[4] D. E. Goldberg, *Genetic algorithms in search, optimization and machine learning* (Addison-Wesley, 1989).

[5] G. J. O. Vermeer, *3D Seismic Survey Design* (SEG Books, 2012).

[6] A. J. Seriff and W. H. Kim, *The effect of harmonic distortion in the use of vibratory surface sources,* Geophysics **35**, 234 (1970).

[7] A. V. Lebedev and I. A. Beresnev, *Nonlinear distortion of signals radiated by vibroseis sources,* Geophysics **69**, 968 (2004).

[8] D. Walker, *Harmonic resonance structure and chaotic dynamics in the earth-vibrator system,* Geophysical Prospecting **43**, 487 (1995).

[9] D. A. Okaya, E. Karageorgi, T. V. McEvilly, and P. E. Malin, *Removing vibrator-induced correlation artifacts by filtering in frequency-uncorrelated time space,* Geophysics **57**, 916 (1992).

[10] X. P. Li, W. Söllner, and P. Hubral, *Elimination of harmonic distortion in vibroseis data,* Geophysics **60**, 503 (1995).

[11] C. B. Harrison, G. F. Margrave, M. Lamoureux, A. Siewert, A. Barrett, and H. Isaac, *From noise to signal - harnessing harmonics for imaging,* SEG (Soc. Expl. Geophys., Expanded abstracts, 2013).

[12] Y. S. Lei, J. F. Wang, M. J. Guo, X. F. Liang, and Y. L. Zhao, *Separating harmonics for vibroseis imaging,* EAGE (Eur. Ass. of Geosc. and Eng., Expanded abstracts, 2015).

[13] A. J. Berkhout, *Changing the mindset in seismic acquisition,* The Leading Edge **27**, 924 (2008).

[14] X. Campman, P. Behn, and K. Faber, *Sensor density or sensor sensitivity?* The Leading Edge **35**, 578 (2016).

[15] G. Berkhout and G. Blacquière, *Effect of noise in blending and deblending,* Geophysics **78**, A35 (2013).

[16] W. P. Kimman and P. L. Vermeer, *Use of low and high noise models for land surface-seismic data,* EAGE (Eur. Ass. of Geosc. and Eng., Expanded abstracts, 2015).

[17] R. M. Laws, E. Kragh, and G. Morgan, *Are seismic sources too loud?* EAGE (Eur. Ass. of Geosc. and Eng., Expanded abstracts, Rome, 2008).

[18] A. Stienstra, A. S. Badger, and P. W. Maxwell, *Intrinsic noise in geophones,* EAEG (Eur. Ass. of Expl. Geophys., Expanded abstracts, 1993) p. A039.

[19] J. Meunier and T. Bianchi, *How long should the sweep be?* SEG (Soc. Expl. Geophys., Expanded abstracts, 2012).

[20] J. R. Peterson, *Observations and modeling of seismic background noise* (U.S. Geological Survey - Open-File Report 93-322, 1993).

[21] T. Dean and M. Al Hasani, *The spectral characteristics of seismic noise recorded in an urban environment,* EAGE (Eur. Ass. of Geosc. and Eng., Expanded abstracts, 2018).

ACKNOWLEDGEMENTS

My PhD in Delft has definitely been a journey. Many people contributed to it directly and indirectly, and I am extremely grateful to each of them.
First, I would like to thank my supervisor Dr. Gerrit Blacquière for his continuing academic and personal support during these years. I value dearly the numerous and fruitful discussions we had during our weekly meetings. Without those I would have not achieved the same goal in my research as I did. Thank you for teaching me how important it is to deliver and communicate scientific research in an effective and professional way. Many thanks go to Dr. Eric Verschuur as well, for being a great support on a personal and scientific level despite not being my direct supervisor.
I am very glad to have been part of the Delphi Consortium and want to extend my acknowledgments to every company and institution who supported it financially and academically. During my time with Delphi, I had the pleasure to meet and receive valuable advice from Prof. Guus Berkhout, who had first proposed the very same concept of Dispersed Source Arrays my thesis is focused on. I am very grateful to Prof. Dries Gisolf and Prof. Stefan Luthi, with whom I had the first interview for my PhD position. All the best wishes also to Dr. Femke Vossepoel, a very inspiring new supervisor within the Delphi team.
In the course of my PhD, I had the opportunity to complete two different internships. I would like to thank my supervisor Dr. Xander Campnam and the geophysics acquisition team for their help and support during my internship in Shell. I learnt a lot throughout my time with them. The second internship took place in Dharhan, Saudi Arabia, where I collaborated with Aramco. My experience in the company was priceless and I am extremely grateful to the entire research and support teams in EXPEC ARC. A special acknowledgment goes to Dr. Abdulrahman AlShuhail, Dr. Constantinos Tsingas and Dr. Khalid O. Rufaii, I could not have asked for better supervisors. It was a pleasure to meet Alok (Shell) and Abdulrahman (Aramco) again in a different setting, after spending so much time together as fellow PhD candidates.
I am grateful to my committee members for reviewing my thesis. I look forward to more mutually beneficial discussions in the future. In particular, thanks to Prof. Kees Wapenaar for his support as a promotor.
My gratitude goes to Hanneke Berkhout, Gerrie van der Beek and Angela van der Sande who always made sure that the Delphi meetings would be smooth and greatly organized. A special mention to Margaret van Fessem, who ensured that my time in the Netherlands was comfortable from the very beginning. Many thanks to Edo Bergsma and Henry den Bok for their invaluable technical help.
My Delphi colleagues were always source of great motivation and support. I really hope I helped you as much as you helped me. Thank you Alok, Xander, Amarjeet, Gabriel, Apostolos, Abdulrahman, Mikhail, Siddharth, Shan, Sixue, Aparajita, Runhai, Junhai, Jan-Willem, Aayush, Tomo, Ali, Buchaib, Hussein, Nick, Siamak, Shotaro, Billy, Shogo,

Leo, Halah, Özkan and Hannes.
My time in the faculty of Geoscience and Civil Engineering was made much more enjoyable by the colleagues and friends I made along the way. Thanks to Max, Ranjani, Rémi (and of course Emilie, Croquette and Bernadette), Elisa, Pawan, Joeri, Myrna, Diego, Paloma, Boris, Karlien, Niels, Iris, Carlos, Giovanni, Alex, Asiya, Lele, Chris, Florencia, Gil, Lisanne, Helena, Nicolas, Martha, Youwei. A special mention to Dr. Guy Drijkoningen, thanks for the inspiring time during our field acquisition work in Novi Sad (Serbia) and during my teaching assistance tasks.
Thanks to Fanny, Agnese, Jón, Gabrielle, Sanjula, Bettie, Florian, Stefania, Francesca, Ad, Jennifer, Anna and Margaux for being my home and my family in the Netherlands. Thanks to Maria and Ibrahim for being there along the way and for teaching me, in very different ways, valuable lessons about life and interaction.
Last but not least, I thank my parents, my family and all the friends I had the honor to meet during my time in Aviano, Trieste, Granada, Pisa, Delft, Rotterdam, Khobar and Bogotá (including who I have already mentioned above). I take full responsibility for whatever will turn out to be wrong in this thesis. The merit for what is right is all yours.

A

APPENDIX

A

A.1. Proof of Equation 4.8

Assuming that $\vec{P}^+(z_0) = \vec{P}^-(z_N) = 0$, from Equations 4.1 and 4.6 it follows:

$$\vec{P}^+(z_n) = \mathbf{W}^+(z_n, z_{n-1})\left[\vec{S}^+(z_{n-1}) + \mathbf{T}^+(z_{n-1})\,\vec{P}^+(z_{n-1}) + \mathbf{R}^\cap(z_{n-1})\,\vec{P}^-(z_{n-1})\right]. \tag{A.1}$$

Recursively, we obtain:

$$\begin{aligned}
&\vec{P}^+(z_n) = \mathbf{W}^+(z_n, z_{n-1})\,\vec{A}^+_{n-1} + \mathbf{W}^+(z_n, z_{n-1})\,\mathbf{T}^+(z_{n-1})\,\mathbf{W}^+(z_{n-1}, z_{n-2})\,\vec{A}^+_{n-2} + \\
&+\mathbf{W}^+(z_n, z_{n-1})\,\mathbf{T}^+(z_{n-1})\,\mathbf{W}^+(z_{n-1}, z_{n-2})\,\mathbf{T}^+(z_{n-2})\,\mathbf{W}^+(z_{n-2}, z_{n-3})\,\vec{A}^+_{n-3} + \\
&+\cdots+\left[\coprod_{m=2}^{n-1}\mathbf{W}^+(z_{m+1}, z_m)\,\mathbf{T}^+(z_m)\right]\mathbf{W}^+(z_2, z_1)\,\vec{A}^+_1 + \\
&+\left[\coprod_{m=1}^{n-1}\mathbf{W}^+(z_{m+1}, z_m)\,\mathbf{T}^+(z_m)\right]\mathbf{W}^+(z_1, z_0)\,\vec{A}^+_0 = \mathbf{W}^+(z_n, z_{n-1})\,\vec{A}^+_{n-1} + \\
&+\sum_{k=0}^{n-2}\left[\coprod_{m=k+1}^{n-1}\mathbf{W}^+(z_{m+1}, z_m)\,\mathbf{T}^+(z_m)\right]\mathbf{W}^+(z_{k+1}, z_k)\,\vec{A}^+_k,
\end{aligned} \tag{A.2}$$

where:

$$\vec{A}^+_n = \vec{S}^+(z_n) + \mathbf{R}^\cap(z_n)\,\vec{P}^-(z_n). \tag{A.3}$$

Now let us define:

$$\mathbf{V}^+(z_n, z_k) = \left[\coprod_{m=k+1}^{n-1}\mathbf{W}^+(z_{m+1}, z_m)\,\mathbf{T}^+(z_m)\right]\mathbf{W}^+(z_{k+1}, z_k). \tag{A.4}$$

The symbol $\coprod$ is here defined as the reverse of the π-product:

$$\coprod_{i=0}^{M}\alpha_i = \alpha_M\cdot\alpha_{M-1}\cdot\cdots\cdot\alpha_1\cdot\alpha_0 = \prod_{i=0}^{M}\alpha_{M-i}. \tag{A.5}$$

For $k = n-1$, the π-product is an *empty product* ($\coprod_{m_1}^{m_2} = \prod_{m_1}^{m_2} = 1, \forall m_1 | m_1 > m_2$). Consequently:

$$\vec{P}^+(z_n) = \sum_{k=0}^{n-1}\mathbf{V}^+(z_n, z_k)\left[\vec{S}^+(z_k) + \mathbf{R}^\cap(z_k)\,\vec{P}^-(z_k)\right]. \quad \blacksquare \tag{A.6}$$

A.2. PROOF OF EQUATION 4.9

Assuming that $\vec{P}^+(z_0) = \vec{P}^-(z_N) = 0$, from Equations 4.2 and 4.7 it follows:

$$\vec{P}^-(z_n) = \mathbf{W}^-(z_n, z_{n+1}) \left[\vec{S}^-(z_{n+1}) + \mathbf{T}^-(z_{n+1})\vec{P}^-(z_{n+1}) + \mathbf{R}^\cup(z_{n+1})\vec{P}^+(z_{n+1})\right]. \tag{A.7}$$

Recursively, we obtain:

$$\begin{aligned}
\vec{P}^-(z_n) &= \mathbf{W}^-(z_n, z_{n+1})\vec{A}^-_{n+1} + \mathbf{W}^-(z_n, z_{n+1})\mathbf{T}^-(z_{n+1})\mathbf{W}^-(z_{n+1}, z_{n+2})\vec{A}^-_{n+2} + \\
&+ \mathbf{W}^-(z_n, z_{n+1})\mathbf{T}^-(z_{n+1})\mathbf{W}^-(z_{n+1}, z_{n+2})\mathbf{T}^-(z_{n+2})\mathbf{W}^-(z_{n+2}, z_{n+3})\vec{A}^-_{n+3} + \\
&+ \cdots + \left[\prod_{m=n+1}^{N-2} \mathbf{W}^-(z_{m-1}, z_m)\mathbf{T}^-(z_m)\right]\mathbf{W}^-(z_{N-2}, z_{N-1})\vec{A}^-_{N-1} + \\
&+ \left[\prod_{m=n+1}^{N-1} \mathbf{W}^-(z_{m-1}, z_m)\mathbf{T}^-(z_m)\right]\mathbf{W}^-(z_{N-1}, z_N)\vec{A}^-_N = \mathbf{W}^-(z_n, z_{n+1})\vec{A}^-_{n+1} + \\
&+ \sum_{k=n+2}^{N}\left[\prod_{m=n+1}^{k-1} \mathbf{W}^-(z_{m-1}, z_m)\mathbf{T}^-(z_m)\right]\mathbf{W}^-(z_{k-1}, z_k)\vec{A}^-_k,
\end{aligned} \tag{A.8}$$

where:

$$\vec{A}^-_n = \vec{S}^-(z_n) + \mathbf{R}^\cup(z_n)\vec{P}^+(z_n). \tag{A.9}$$

Now let us define:

$$\mathbf{V}^-(z_n, z_k) = \left[\prod_{m=n+1}^{k-1} \mathbf{W}^-(z_{m-1}, z_m)\mathbf{T}^-(z_m)\right]\mathbf{W}^-(z_{k-1}, z_k). \tag{A.10}$$

For $k = n+1$, the π-product is an *empty product* ($\prod_{m_1}^{m_2} = 1, \forall m_1 | m_1 > m_2$). Consequently:

$$\vec{P}^-(z_n) = \sum_{k=n+1}^{N} \mathbf{V}^-(z_n, z_k)\left[\vec{S}^-(z_k) + \mathbf{R}^\cup(z_k)\vec{P}^+(z_k)\right]. \quad \blacksquare \tag{A.11}$$

B

APPENDIX

B

In order to compute the gradients for the reflectivity and propagation operators, we will make use of the definitions and derivations presented in APPENDIX A and of following property [1]:

$$\frac{\partial ||\mathbf{A}\mathbf{X}\vec{B}+\vec{C}||_2^2}{\partial \mathbf{X}} = 2\mathbf{A}^H\left(\mathbf{A}\mathbf{X}\vec{B}+\vec{C}\right)\vec{B}^H. \tag{B.1}$$

Let us now consider the objective function:

$$J = J_\Delta + J_f, \tag{B.2}$$

where the term f is a constraining function chosen based on user-defined constraints on the reflectivity and velocity models. While:

$$J_\Delta = \frac{1}{2}\sum_{shots}\sum_{\omega}|f_\omega|^2 \|\Delta\vec{P}(z_0)\|_2^2, \tag{B.3}$$

and:

$$\Delta\vec{P}(z_0) = \vec{P}_{obs}(z_0) - \vec{P}^-_{mod}(z_0). \tag{B.4}$$

B.1. Proof of Equation 4.18

For every n between 0 and $N-1$ ($\forall n | 0 \leq n \leq N-1$), we can write:

$$\Delta\vec{P}(z_0) = -\mathbf{V}^-(z_0,z_n)\,\mathbf{R}^\cup(z_n)\,\vec{P}^+_{mod}(z_n) + \vec{D}, \tag{B.5}$$

where:

$$\begin{aligned}\vec{D} = \vec{P}_{obs}(z_0) - \sum_{k=1}^{N}\mathbf{V}^-(z_0,z_k)\,\vec{S}^-(z_k) - \sum_{k=1}^{n-1}\mathbf{V}^-(z_0,z_k)\,\mathbf{R}^\cup(z_k)\,\vec{P}^+_{mod}(z_k) + \\ + \sum_{k=n+1}^{N}\mathbf{V}^-(z_0,z_k)\,\mathbf{R}^\cup(z_k)\,\vec{P}^+_{mod}(z_k).\end{aligned} \tag{B.6}$$

We can thus relate Equations B.1 and B.3 as follows:

$$\begin{aligned}
\mathbf{A}\mathbf{X}\vec{B} + \vec{C} &= \Delta\vec{P}(z_0), \\
\mathbf{A} &= -\mathbf{V}^{-}(z_0, z_n), \\
\vec{B} &= \vec{P}^{+}_{mod}(z_n), \\
\vec{C} &= \vec{D}, \\
\mathbf{X} &= \mathbf{R}^{\cup}(z_n).
\end{aligned} \tag{B.7}$$

Thus:

$$\frac{\partial J}{\partial \mathbf{R}^{\cup}(z_n)} = -\sum_{shots}\sum_{\omega} |f_\omega|^2 [\mathbf{V}^{-}(z_0, z_n)]^H \left[\Delta\vec{P}(z_0)\right]\left[\vec{P}^{+}_{mod}(z_n)\right]^H + \frac{\partial f}{\partial \mathbf{R}^{\cup}(z_n)}. \quad \blacksquare \tag{B.8}$$

B.2. PROOF OF EQUATION 4.19

For every n between 0 and $N-1$ ($\forall n | 0 \leq n \leq N-1$), we can write:

$$\Delta\vec{P}(z_0) = -\mathbf{V}^{\cup}(z_0, z_n)\,\mathbf{R}^{\cap}(z_n)\,\vec{P}^{-}_{mod}(z_n) + \vec{D}, \tag{B.9}$$

where:

$$\begin{aligned}
\vec{D} = \vec{P}_{obs}(z_0) - \sum_{k=1}^{N} \mathbf{V}^{-}(z_0, z_k) \left[\vec{S}^{-}(z_k) + \sum_{j=0}^{k-1} \mathbf{R}^{\cup}(z_k)\,\mathbf{V}^{+}\left(z_k, z_j\right)\vec{S}^{+}\left(z_j\right)\right] + \\
- \sum_{k=1}^{n} \mathbf{V}^{-}(z_0, z_k)\,\mathbf{R}^{\cup}(z_k) \left[\sum_{j=0}^{k-1} \mathbf{V}^{+}\left(z_k, z_j\right)\mathbf{R}^{\cap}\left(z_j\right)\vec{P}^{-}_{mod}\left(z_j\right)\right] + \\
- \sum_{k=n+1}^{N} \mathbf{V}^{-}(z_0, z_k)\,\mathbf{R}^{\cup}(z_k) \left[\sum_{j=0}^{n-1} \mathbf{V}^{+}\left(z_k, z_j\right)\mathbf{R}^{\cap}\left(z_j\right)\vec{P}^{-}_{mod}\left(z_j\right) + \sum_{j=n+1}^{k-1} \mathbf{V}^{+}\left(z_k, z_j\right)\mathbf{R}^{\cap}\left(z_j\right)\vec{P}^{-}_{mod}\left(z_j\right)\right].
\end{aligned} \tag{B.10}$$

We can thus relate Equations B.1 and B.3 as follows:

B

$$\begin{aligned}
\mathbf{AX}\vec{B}+\vec{C} &= \Delta\vec{P}(z_0),\\
\mathbf{A} &= -\mathbf{V}^{\cup}(z_0,z_n),\\
\vec{B} &= \vec{P}^{-}_{mod}(z_n),\\
\vec{C} &= \vec{D},\\
\mathbf{X} &= \mathbf{R}^{\cap}(z_n).
\end{aligned} \tag{B.11}$$

Thus:

$$\frac{\partial J}{\partial \mathbf{R}^{\cap}(z_n)} = -\sum_{shots}\sum_{\omega}|f_\omega|^2\left[\mathbf{V}^{\cup}(z_0,z_n)\right]^H\left[\Delta\vec{P}(z_0)\right]\left[\vec{P}^{-}_{mod}(z_n)\right]^H + \frac{\partial f}{\partial \mathbf{R}^{\cap}(z_n)}. \quad \blacksquare \tag{B.12}$$

B.3. Proof of Equation 4.38

For every n between 0 and $N-1$ ($\forall n|0\le n\le N-1$), we can write (see Equations 4.9 and 4.11):

$$\begin{aligned}
\vec{P}^{-}_{mod}(z_0) = &\sum_{k=1}^{n}\mathbf{V}^{-}(z_0,z_k)\left[\vec{S}^{-}(z_k)+\mathbf{R}^{\cup}(z_k)\vec{P}^{+}_{mod}(z_k)\right]+\\
+&\mathbf{V}^{-}(z_0,z_n)\mathbf{T}^{-}(z_n)\mathbf{W}^{-}(z_n,z_{n+1})\left[\vec{S}^{-}(z_{n+1})+\mathbf{R}^{\cup}(z_{n+1})\vec{P}^{+}_{mod}(z_{n+1})\right]+\\
+&\sum_{k=n+2}^{N}\mathbf{V}^{-}(z_0,z_k)\left[\vec{S}^{-}(z_k)+\mathbf{R}^{\cup}(z_k)\vec{P}^{+}_{mod}(z_k)\right],
\end{aligned} \tag{B.13}$$

and:

$$\mathbf{V}^{-}(z_0,z_k) = \mathbf{V}^{-}(z_0,z_n)\mathbf{T}^{-}(z_n)\mathbf{W}^{-}(z_n,z_{n+1})\mathbf{T}^{-}(z_{n+1})\mathbf{V}^{-}(z_{n+1},z_k). \tag{B.14}$$

Thus, it follows that (see Equations 4.2 and 4.9):

$$\Delta\vec{P}(z_0) = -\mathbf{V}^{-}(z_0,z_n)\mathbf{T}^{-}(z_n)\mathbf{W}^{-}(z_n,z_{n+1})\vec{Q}^{-}_{mod}(z_{n+1})+\vec{D}, \tag{B.15}$$

where:

$$\vec{D} = \vec{P}_{obs}(z_0) - \sum_{k=1}^{n}\mathbf{V}^{-}(z_0,z_k)\left[\vec{S}^{-}(z_k)+\mathbf{R}^{\cup}(z_k)\vec{P}^{+}_{mod}(z_k)\right]. \tag{B.16}$$

We can thus relate Equations B.1 and B.3 as follows:

$$\begin{aligned}
\mathbf{A}\mathbf{X}\vec{B}+\vec{C} &= \Delta\vec{P}(z_0),\\
\mathbf{A} &= -\mathbf{V}^{-}(z_0,z_n)\,\mathbf{T}^{-}(z_n),\\
\vec{B} &= \vec{Q}^{-}_{mod}(z_{n+1}),\\
\vec{C} &= \vec{D},\\
\mathbf{X} &= \mathbf{W}^{-}(z_n,z_{n+1}).
\end{aligned} \tag{B.17}$$

Thus:

$$\frac{\partial J}{\partial \mathbf{W}^{-}(z_n,z_{n+1})} = -\sum_{shots}\sum_{\omega}|f_\omega|^2\left[\mathbf{V}^{\nabla}(z_0,z_n)\right]^H\left[\Delta\vec{P}(z_0)\right]\left[\vec{Q}^{-}_{mod}(z_{n+1})\right]^H + \frac{\partial f}{\partial \mathbf{W}^{-}(z_n,z_{n+1})}, \tag{B.18}$$

with:

$$\mathbf{V}^{\nabla}(z_0,z_n) = \mathbf{V}^{-}(z_0,z_n)\,\mathbf{T}^{-}(z_n). \quad \blacksquare \tag{B.19}$$

B.4. PROOF OF EQUATION 4.37

For every n between 0 and $N-1$ ($\forall n|0\le n\le N-1$), we can write (see Equations 4.9-4.11):

$$\begin{aligned}
\vec{P}^{-}_{mod}(z_0) &= \sum_{k=1}^{N}\mathbf{V}^{-}(z_0,z_k)\,\vec{S}^{-}(z_k) +\\
&+\sum_{k=1}^{n}\mathbf{V}^{-}(z_0,z_k)\,\mathbf{R}^{\cup}(z_k)\,\vec{P}^{+}_{mod}(z_k) + \sum_{k=n+1}^{N}\mathbf{V}^{-}(z_0,z_k)\,\mathbf{R}^{\cup}(z_k)\,\vec{P}^{+}_{mod}(z_k),
\end{aligned} \tag{B.20}$$

as well as:

$$\mathbf{V}^{+}\left(z_k,z_j\right) = \mathbf{V}^{+}(z_k,z_n)\,\mathbf{T}^{+}(z_n)\,\mathbf{V}^{+}\left(z_n,z_j\right). \tag{B.21}$$

and:

$$\begin{aligned}
\vec{P}^{+}_{mod}(z_k) &= \sum_{j=n+1}^{k-1}\mathbf{V}^{+}\left(z_k,z_j\right)\left[\vec{S}^{+}\left(z_j\right)+\mathbf{R}^{\cap}\left(z_j\right)\vec{P}^{-}_{mod}\left(z_j\right)\right] +\\
&+\mathbf{V}^{+}(z_k,z_n)\left[\vec{S}^{+}(z_n)+\mathbf{R}^{\cap}(z_n)\,\vec{P}^{-}_{mod}(z_n)\right] +\\
&+\mathbf{V}^{+}(z_k,z_n)\,\mathbf{T}^{+}(z_n)\sum_{j=0}^{n-1}\mathbf{V}^{+}\left(z_n,z_j\right)\left[\vec{S}^{+}\left(z_j\right)+\mathbf{R}^{\cap}\left(z_j\right)\vec{P}^{-}_{mod}\left(z_j\right)\right],
\end{aligned} \tag{B.22}$$

Thus, it follows that (see Equations 4.1 and 4.8):

$$\Delta\vec{P}(z_0) = -\mathbf{V}^{\triangle}(z_0, z_{n+1})\,\mathbf{W}^{+}(z_{n+1}, z_n)\,\vec{Q}^{+}_{mod}(z_n) + \vec{D}, \tag{B.23}$$

where:

$$\begin{aligned}\vec{D} = \vec{P}_{obs}(z_0) - \sum_{k=1}^{N}\mathbf{V}^{-}(z_0, z_k)\,\vec{S}^{-}(z_k) + \\ - \sum_{k=1}^{n}\mathbf{V}^{-}(z_0, z_k)\,\mathbf{R}^{\cup}(z_k)\,\vec{P}^{+}_{mod}(z_k) + \\ - \sum_{k=n+1}^{N}\mathbf{V}^{-}(z_0, z_k)\,\mathbf{R}^{\cup}(z_k)\sum_{j=n+1}^{k-1}\mathbf{V}^{+}(z_k, z_j)\left[\vec{S}^{+}(z_j) + \mathbf{R}^{\cap}(z_j)\,\vec{P}^{-}_{mod}(z_j)\right],\end{aligned} \tag{B.24}$$

and:

$$\mathbf{V}^{\triangle}(z_0, z_n) = \mathbf{V}^{-}(z_0, z_n)\,\mathbf{R}^{\cup}(z_n) + \mathbf{V}^{\cup}(z_0, z_n)\,\mathbf{T}^{+}(z_n), \tag{B.25}$$

with:

$$\mathbf{V}^{\cup}(z_0, z_n) = \sum_{k=n+1}^{N}\mathbf{V}^{-}(z_0, z_k)\,\mathbf{R}^{\cup}(z_k)\,\mathbf{V}^{+}(z_k, z_n). \tag{B.26}$$

We can thus relate Equations B.1 and B.3 as follows:

$$\begin{aligned}\mathbf{A}\mathbf{X}\vec{B} + \vec{C} &= \Delta\vec{P}(z_0), \\ \mathbf{A} &= -\mathbf{V}^{\triangle}(z_0, z_{n+1}), \\ \vec{B} &= \vec{Q}^{+}_{mod}(z_n), \\ \vec{C} &= \vec{D}, \\ \mathbf{X} &= \mathbf{W}^{+}(z_{n+1}, z_n).\end{aligned} \tag{B.27}$$

Thus:

$$\frac{\partial J}{\partial \mathbf{W}^{+}(z_{n+1}, z_n)} = -\sum_{shots}\sum_{\omega}|f_\omega|^2\left[\mathbf{V}^{\triangle}(z_0, z_{n+1})\right]^{H}\left[\Delta\vec{P}(z_0)\right]\left[\vec{Q}^{+}_{mod}(z_n)\right]^{H} + \frac{\partial f}{\partial \mathbf{W}^{+}(z_{n+1}, z_n)}. \tag{B.28}$$

■

REFERENCES

[1] M. Brookes, *The Matrix Reference Manual* (online: http://www.ee.imperial.ac.uk/hp/staff/dmb/matrix/intro.html, 2011).